“I’ve failed over and over and over again in my life and that is why I succeed.”

Michael Jordan

University of Alberta

ULTRAFAST TERAHERTZ SPECTROSCOPY OF SEMICONDUCTING MATERIALS

by

Sijia Xu

A thesis submitted to the Faculty of Graduate Studies and Research
in partial fulfillment of the requirements for the degree of

Master of Science

Department of Physics

Fall 2013
Edmonton, Alberta

Abstract

Terahertz spectroscopy is a powerful non-contact technique to study the optical and electric properties of materials at sub-picosecond time scales. In this study, ultrafast time-resolved terahertz spectroscopy was performed on both silicon-on-sapphire (SOS) and iron pyrite (FeS_2) nano-crystalline films that have potential application in photovoltaics. Transient conductivity after photoexcitation with ultrashort optical pulses was studied by extracting the complex conductivity from the terahertz spectra. The Drude model provides an excellent fit to the photoconductivity of SOS excited at moderate pump fluences. However, at higher excitation fluences, the SOS exhibits some carrier localization that is best described by a Drude-Smith model. The photoconductivity of the FeS_2 nanocrystalline film exhibits Drude-Smith behavior with very strong carrier localization, and is around 20% of the photoconductivity of SOS. The relationship between the Drude scattering time and the photocarrier density in both materials can be described by the Caughey-Thomas model.

Acknowledgements

First of all I would like to express my gratitude to my supervisor, Dr. Frank Hegmann. I feel honoured to be a member of this group under his guidance. He is very knowledgeable in the area of THz technology, and always explores new areas to extend his knowledge. His scientific rigor has set up a great example, and his sharp mind always inspires me with different ways to approach problems. During the research project, he always drops in the lab with an amiable smile, and helps me on my experiments whenever I need. He never blames his students for the faults we make, but he always explains the problems clearly for us so that we understand the mechanisms thoroughly.

I would also like to express my appreciation to Dr. Lyubov Titova, who helped me throughout the whole research project. As a highly experienced research associate in this group, her strong knowledge of both theoretical and experimental physics inspired me to a great extent. She taught me the very basic concepts of the ultrafast THz spectroscopy from the beginning, and constantly helped me to improve my skills.

I also want to thank Dr. Zhenyou Wang and Dr. Tyler Cocker for their kind assists and advices in the experiments. They both guided me conduct experiments safely. During their stay in the Ultrafast Spectroscopy Lab, they are like elder brothers of mine, and kept teaching me new things. Joshua LaForge and other co-workers from Dr. Mike Brett's group have my gratitude for their support on my project of FeS_2 nano-crystalline films. Joshua has made a huge amount of effort to prepare nice samples for my study. Special thanks are to Glenda De Los Reyes, Ayesheshim K. Ayesheshim, Vedran Jelic, James Hoffman, and Landon Haynes, who have provided me with valuable suggestions and expertises in their specialization.

I am very grateful to Don Mullin and Greg Popowich, who are the best specialist technicians I have ever met. Don has trained me on many types of equipment that are important to my research project. Greg has helped me install and fix various types of instruments in our lab. They both contributed to maintain the labs functioning with their professional knowledges and skills.

I also want to thank Dr. John Beamish and Dr. Kevin Beach for being my supervisor committee members. They provided me with profound advices with their sharp minds as my research project was ongoing. Without them, I wouldn't have been doing my research project so smoothly. I want to thank Dr. Michael Brett for being my exam committee member, too.

Finally, I would like to express my endless gratitude to my dear parents, Jianzhong Xu and Jialan Zhou. They have done everything they can to support me both in my personal life and my education. I also want to thank my dear grandparents, Ada Zhou and Mingbao Sun, who raised me up, gave me a wonderful memory in childhood, and taught me invaluable knowledge for being a good person. I genuinely want to thank my lovely fiancée, Minzhi Du, who has made our home so warm and sweet. As the most important person in me life, she motivates me to become better, and always guides me when I am lost.

Table of Contents

List of Tables

List of Figures

List of Symbols

THz	Terahertz	10^{12} [Hz]
THz-TDS	Terahertz Time Domain Spectroscopy	
TRTS	Time Resolved Terahertz Spectroscopy	
ZnTe	Zinc Telluride	
GaAs	Gallium Arsenide	
FeS_2	Iron Pyrite	
SOS	Silicon-on-Saphire	
ps	Pico-Second	10^{-12} [s]
fs	Femto-Second	10^{-15} [s]
F	Fluence	[μJ/cm^2]
eV	electronVolt	1.602×10^{-19} [J]
e	Elementary Charge	1.602×10^{-19} [C]
k_B	Boltzmann Constant	1.38×10^{-23} [J/K]
h	Planck Constant	6.626×10^{-34} [Js]
ϵ_0	Vacuum Permittivity	8.854×10^{-12} [F/m]
μ_0	Magnetic Constant	1.257×10^{-6} [N/A^2]
Z_0	Impedance of Free Space	377 [Ω]
$\hat{\sigma}$	Complex Conductivity	[S/cm]
ω	Angular Freqeuncy	[rad/s]
ν	Frequency of Photon	[Hz]
μ	Carrier Mobility	[cm^2/Vs]
η	Quantum Efficiency	
ω_p	Plasma Frequency	
ν_p	Plasma Ordinary Frequency	[THz]
c	Speed of Light	[m/s]
c_n	Carrier Localization Parameter	
N	Refractive Index	
n	Carrier Density	[cm^{-3}]
α	Absorption Coefficient	[cm^{-1}]
δ_p	Optical Penetration Depth	[nm]

Chapter 1

Introduction

The terahertz (THz—10^{12} Hz) wave region is located between the microwave and infrared regions of the electromagnetic spectrum, as shown in Fig. 1.1. Recent developments in femtosecond lasers and THz sources have greatly enhanced exploration in the THz region of the spectrum [1]. In the last several decades, many terahertz experimental systems and techniques [2] have been developed with both continuous and pulsed THz beams. It has been shown that terahertz waves can be used in imaging [3–5], security applications [6], food industry, quality control [7], pharmaceutical and medical industry [8–10], semiconductor industry [11, 12], superconductor technology [13–15], and nanotechnology [16].

As the corresponding photon energy of THz pulses is in millielectronvolt (meV) scale (1 THz = 4.1 meV), THz pulses are ideal for probing excitations that have picosecond lifetimes and energies in meV scale [2]. The non-invasiveness of THz spectroscopy also makes it preferable to traditional con-

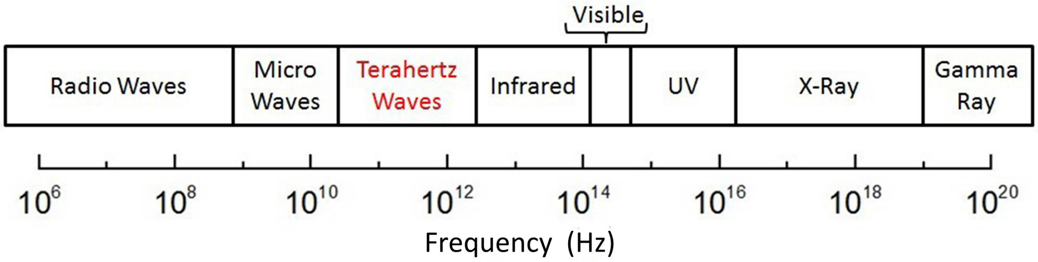

Figure 1.1: The electromagnetic spectrum ranging from radio waves to gamma rays. The terahertz range is between microwaves and infrared waves, corresponding to a frequency range around 10^{12} Hz (1 THz).

tact techniques and reduces complications associated with contacting materials. Among many techniques developed recently, terahertz time-domain spectroscopy (THz-TDS) and time-resolved terahertz spectroscopy (TRTS) are the two most widely used techniques in studying semiconductors [17]. Since the conductivity in the THz range is highly sensitive to the presence of free carriers, it is possible to observe the ultrafast photoexcited carrier dynamics in semiconductors with the use of an optical pump pulse and THz probe pulse. Also, both the intrinsic complex conductivity and photoexcited conductivity can be extracted by simply comparing the corresponding THz transmission spectra. When comparing the extracted conductivity data with theoretical conductivity models such as the Drude model and the Drude-Smith model, the intrinsic properties of different semiconductors can be analyzed [18].

Much work has already been done successfully on a wide range of semiconductors with ultrafast THz spectroscopy. Conductivity in the THz range in some bulk semiconductors, such as gallium arsenide (GaAs) [19–22] and silicon [23, 24], has been studied by many groups. Because of the strong photoresponse and well-studied conductivities of these two materials, they are widely used as reference samples in ultrafast THz spectroscopy experiments. In the last decade, there has been interest in studying organic semiconductors. Pentacene is one of the most popular organic semiconductors which has been studied by ultrafast THz spectroscopy [12, 25, 26] to understand its semiconducting properties and ultrafast carrier dynamics. Also, ultrafast THz spectroscopy has been performed on many nanostructured materials [27–29].

This thesis mainly focusses on the study of bulk silicon-on-sapphire (SOS) films and iron pyrite (FeS_2) nano-crystalline films. FeS_2 has gained a lot of attention in the area of photovoltaics because of its high absorbance and abundance. In the meantime, silicon is the most widelyused semiconductor in the world. It is reasonable to study the properties of FeS_2 nano-crystalline films with silicon as a baseline. THz-TDS was performed on the FeS_2 thin films to extract the complex conductivity of the samples. The more powerful technique TRTS was used to study the carrier dynamics, mobility, and photoconductivity of both SOS films and FeS_2 films.

Chapter 2

Time-Resolved Terahertz Spectroscopy

2.1 THz Pulses

Single-cycle THz pulses can be produced by techniques utilizing ultrafast laser pulses. A sample THz pulse waveform and its corresponding amplitude spectrum are shown in Fig. 2.1. To study the optical and electrical properties in semiconductors, pulsed THz waves are usually used instead of continuous THz waves. With an ultrafast laser source that produces ultrashort femtosecond laser pulses, it is possible to get single THz pulses containing frequency components up to several THz. The spectral width of terahertz pulses depends on

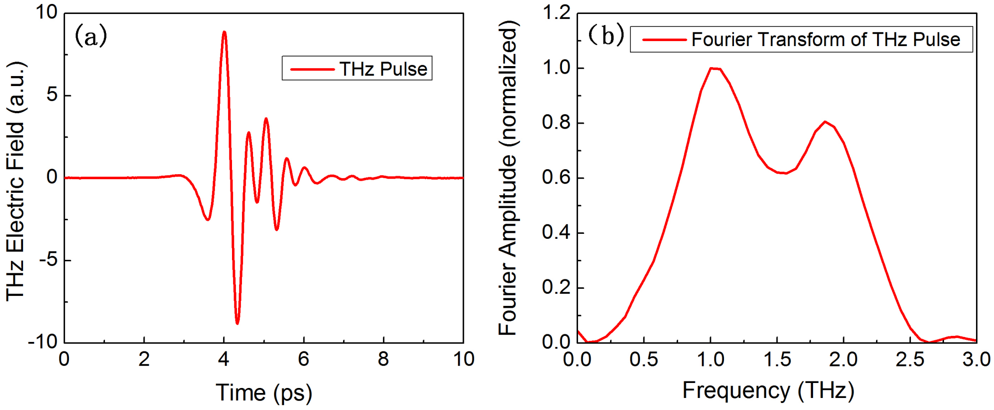

Figure 2.1: (a) A terahertz pulse waveform. The pulse duration is around 2 picoseconds (b) The corresponding amplitude spectrum of the terahertz pulse.

the generation method, the laser source condition and many other factors [1,2].

Though ultrafast THz spectroscopy is still a relatively new technique, several methods have already been developed to generate and detect THz pulses, enabling time-resolved terahertz spectroscopy. The generation and sampling of THz pulses, along with the experimental detail, will be discussed in the following sections.

2.2 Generating and Detecting THz Pulses

The mechanisms of generating and detecting a terahertz pulse determine the capability of a THz spectroscopy system. There are many different techniques to generate [30, 31] and detect [32] THz pulses. A good ultrafast THz spectroscopy system should have high signal-to-noise ratio, high time resolution and broad frequency bandwidth. All these features are related to the techniques used in generating and detecting THz pulses [33–35]. Some of the most widely used techniques will be introduced in this section.

2.2.1 Generating THz Pulses by Optical Rectification

The two most widely used methods to generate THz pulses are optical rectification and photoconductive switch. Both of them rely on the use of femtosecond laser sources. In the case of a photoconductive switch, an ultrashort laser pulse is sent to a semiconductor substrate that has a bias voltage applied at the surface. The ultrashort laser pulse excites the semiconductor into conducting state. As a result, the biased voltage drives an ultrafast current across the semiconductor surface whose duration is related to the rising time of the excitation in the semiconductor substrate [36]. The THz pulse, whose electric field is proportional to the temporal derivative of the ultrafast current density, is then emitted from the semiconductor.

Another method called optical rectification is also frequently used to generate THz pulses [31, 37]. In optical rectification, an incident laser pulse induces a transient polarization [38] in a nonlinear crystal, as illustrated in Fig. 2.2. Optical rectification utilizes a nonlinear crystal whose dielectric polarization P responds nonlinearly (containing higher order terms) [39, 40] to the electric field as

$$P(t) \propto \chi^{(1)}E(t) + \chi^{(2)}E(t)^2 + \chi^{(3)}E(t)^3 + \cdots \tag{2.1}$$

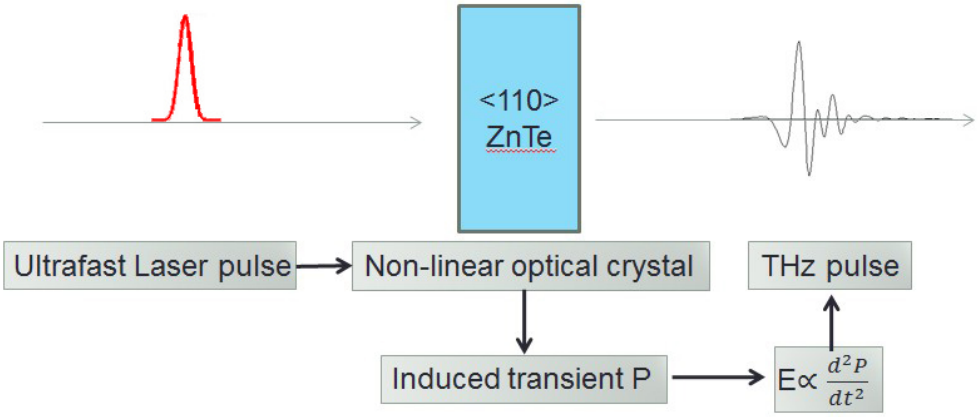

Figure 2.2: Schematic diagram of the main steps in optical rectification. An 800 nm ultrashort laser pulse is directed onto a $\langle 110 \rangle$ ZnTe crystal. The electric field of the incident laser pulse then induces a nonlinear polarization in the crystal. The transient polarization emits electromagnetic waves in the THz range.

The higher order terms are only present when the incident field is high enough. For an incoming wave that contains two frequencies, having the form $E(t) = E_a \cos(\omega_a t) + E_b \cos(\omega_b t)$, and considering terms only to second order, the polarization is given by

$$\begin{aligned} P^{(2)}(t) \propto \chi^{(1)} E(t) + \chi^{(2)} \frac{E_a^2}{2} \cos(2\omega_a t) + \chi^{(2)} \frac{E_b^2}{2} \cos(2\omega_b t) \\ + \chi^{(2)} E_a E_b \cos\big[(\omega_a + \omega_b)t\big] + \chi^{(2)} E_a E_b \cos\big[(\omega_a - \omega_b)t\big] \\ + \chi^{(2)} \frac{E_a^2 + E_b^2}{2}. \end{aligned} \tag{2.2}$$

Optical rectification refers to the constant term $\frac{1}{2}\chi^{(2)}(E_a^2 + E_b^2)$ and the low frequency difference term $\chi^{(2)} E_a E_b \cos(\omega_a - \omega_b)t$. The optical rectification term is responsible for the THz wave emission. The incident ultrashort laser pulse actually consists of a group of standing modes centered at 800 nm having frequency difference $\Delta\nu = c/2L$, where L is the distance between the mirrors in the laser cavity. So the frequency mixing in an ultrafast laser pulse always induces a frequency difference term that can generate THz radiation.

When using Maxwell's equation in media [41], the wave equation

$$\nabla^2 E = \frac{n^2}{c^2} \frac{\partial^2}{\partial t^2} E + \frac{1}{\epsilon_0 c^2} \frac{\partial^2}{\partial t^2} P \tag{2.3}$$

is an inhomogeneous differential equation. The radiation due to optical rectification is proportional to $\partial^2 P/\partial t^2$ and is only dependent on the ultrafast pulse's time profile. When the incident laser pulse was sub-picosecond duration, the emitted wave from the optical rectification term is in the THz range.

2.2.2 Detecting THz Pulses with Free-Space Electro-Optic Sampling

A pulsed probe beam split from the same laser source that generates THz pulses is used to probe the THz waveform. The two commonly used ways to detect THz pulses are photoconductive sampling and free-space electro-optic sampling [42]. Photoconductive sampling acts in the opposite way of a photoconductive switch. Two electrodes with a potential difference are deposited on a semiconductor substrate. When a probe pulse arrives at the surface between these two electrodes, it excites the semiconductor between electrodes. If a THz pulse arrives at the substrate at the same time, a transient current proportional to the strength of the THz electric field is formed. By using a semiconductor substrate that has very short recovery time, the THz electric field can be mapped out by changing the delay between the THz pulse and the probe pulse.

Electro-optic sampling utilizes the Pockels effect in a nonlinear crystal to probe THz pulses. As an example, the detection system based on a $\langle 110\rangle$ ZnTe crystal used in our setup is introduced. The setup consists of a $\langle 110\rangle$ crystal, a quater-wave plate, a Wollaston Prism, and two balanced detectors. A schematic diagram is shown in Fig. 2.3.

The setup has to be balanced without the arrival of a THz pulse. When there is no THz pulse arriving at the ZnTe crystal, the probe pulse passes through it without changing its polarization state. (The quarter-wave plate is positioned such that the probe beam is circularly polarized after passing through.) The Wollaston Prism then separates the circularly polarized beam into a horizontally-polarized beam and a vertically-polarized beam. The two beams are then detected by two photodiodes [43, 44]. Without the THz pulse, the two detectors should be perfectly balanced and display the same reading.

When the THz pulse arrives at the ZnTe crystal, the electric field of THz pulse induces a birefringence in the $\langle 110\rangle$ ZnTe crystal [45]. The extent of the birefringence is proportional to the electric field, as given by the Pockels

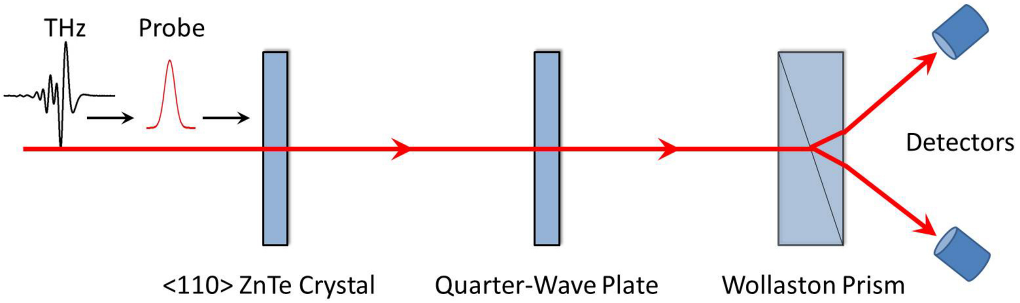

Figure 2.3: Schematic diagram of the setup for electro-optic sampling. The red solid line is the probe beam and the black waveform is the THz signal.

effect. Now the probe pulse becomes elliptically polarized after going through the quarter-wave plate. The vertical component no longer equals the horizontal component, and the difference between these two detected pulses reflects the strength of the THz pulse electric field. Theoretically, frequencies of up to 5.3 THz, limited by the phonon frequency in ZnTe crystal, should be detectable. However, the actual spectrum depends on many factors, such as laser pulse width, laser power, crystal thickness, phase matching, *etc.* Our setup in the lab is able to detect frequency up to 2.7 THz with a very high signal to noise ratio of several hundred.

2.3 Ultrafast THz Spectroscopy

THz spectroscopy has grown very fast during the last 30 years. Because of its energy scale, it is widely used in studying free carrier excitation [46], carrier properties [19, 47], intraband processes [20, 48–50], phonon modes [51], and dielectric constants [25]. The detailed setup can vary widely between groups, but the main parts are always the same, as shown in Fig. 2.4.

2.3.1 Terahertz Time-Domain Spectroscopy

THz-Time Domain Spectroscopy (THz-TDS) is a powerful method to measure intrinsic properties without any physical contact. The pulsed laser source is split into an optical pump beam, a THz generation beam, and a probe beam. In THz-TDS experiments, only the THz generation beam and probe beam are

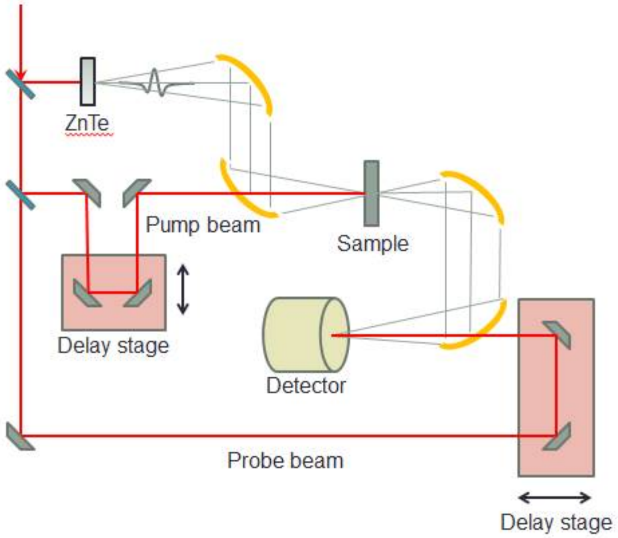

Figure 2.4: Layout of a typical ultrafast THz spectroscopy setup.

used. Delay stages are used in the experiment to produce time delays between the beams. By moving the delay stage, the relative delay between the probe pulse and the THz pulse can be controlled [37, 42]. The whole THz waveform can be mapped out by moving the delay stage, which also allows the detectors to take many averages at each point to improve the signal-to-noise ratio.

As an example, the THz-TDS data of a gallium arsenide (GaAs) wafer along with a reference THz pulse is plotted in Fig. 2.5. The THz pulse transmitted through the GaAs wafer is delayed in the time domain due to the refractive index of GaAs. The electric field is also attenuated due to reflection loss at the boundary and absorption in the sample. Using discrete Fast Fourier Transforms, the frequency-dependent amplitude and phase spectra of these two THz waveforms can be calculated and are plotted in Fig. 2.6.

A simple way to calculate a rough estimate of the refractive index is to substitute the delay time Δt between the THz pulse peaks into the following equation:

$$N = \frac{\Delta t \cdot c}{d} + 1. \tag{2.4}$$

Here, N is the refractive index of the sample, d is the thickness of the sample, and c is the speed of light. This method gives a rough value of 3.72, which is close to the value 3.6 observed before for a GaAs wafer with a thickness of 0.5 mm [52]. To extract more accurate frequency-dependent values, a THz waveform transmitted through a sample is compared to the waveform without a sample in place [53]. Taking the ratio of the frequency dependent spectra

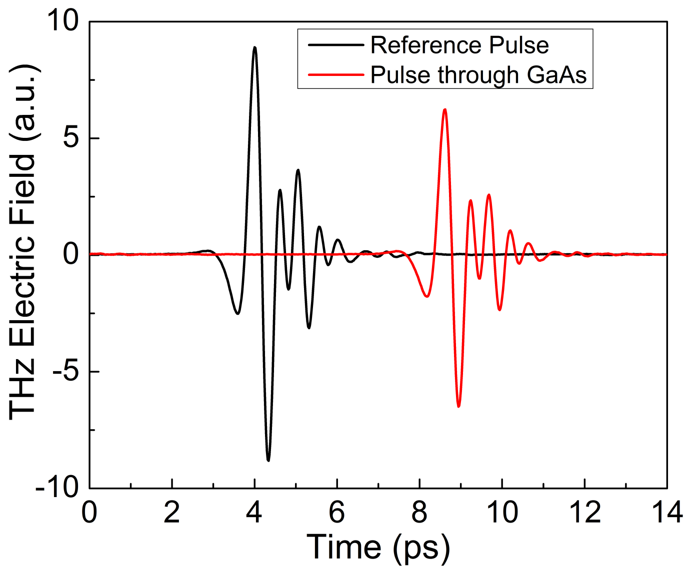

Figure 2.5: THz-TDS data of GaAs wafer plotted along with a reference THz pulse through vacuum. The two scans were acquired over the same time window.

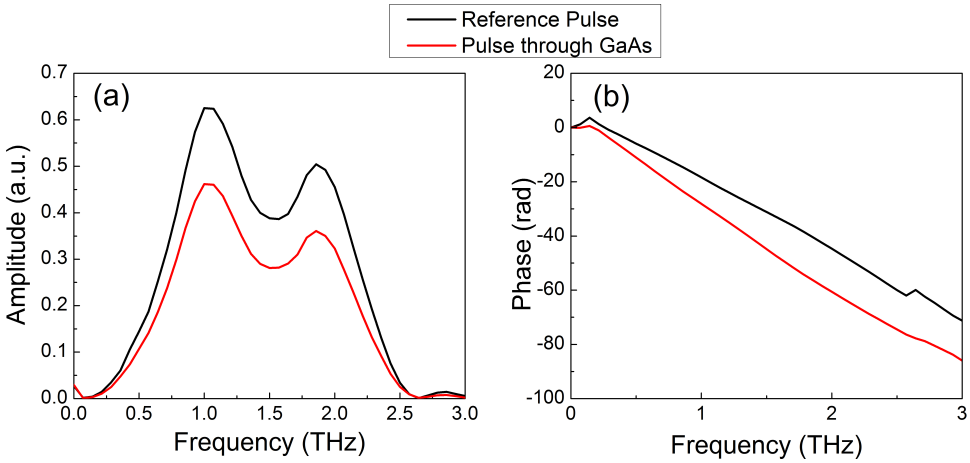

Figure 2.6: (a) Amplitude and (b) phase spectra calculated using Fast Fourier Transform of the THz-TDS data of GaAs wafer from the THz waveforms shown in Fig. 2.5.

with and without the sample, we get

$$\frac{E_s(\omega)}{E_0(\omega)} = (|t|e^{-\frac{\alpha}{2}d}) \cdot (e^{i\Phi}e^{i\frac{\omega}{c}d(N-1)}), \tag{2.5}$$

where $\Phi = \phi_s - \phi_0$ is the phase difference between the THz pulse waveform passing through the sample and that passing through free space, and ω is the angular frequency [51]. Separately comparing these two parts of the spectra, we are able to get the frequency dependent THz refractive index, N, and absorption coefficient, α.

$$N = \frac{c}{\omega d}[\phi_s(\omega) - \phi_0(\omega) - \Phi] + 1, \tag{2.6}$$

$$\alpha = -\frac{2}{d}\ln\left(\frac{|E_s(\omega)|}{|t||E_0(\omega)|}\right). \tag{2.7}$$

However, the reflection and transmission at the sample boundary can be very complicated, and we typically do not know the value of $|t|$. In order to extract the actual value, numerical methods involving many iterations have to be used along with the result from Fresnel's equation at the boundary [52].

There is an easier way that avoids numerical work. Instead of doing a numerical calculation based on a single measurement, the transmission through two samples with different film thickness can be compared to get the complex refractive index. In such a case, we do not need to know the reflection and transmission at the boundary because they cancel out for the two samples. Uncertainty from numerical calculations can also be avoided in this case. Since THz-TDS is not the main focus in this study, it will not be extensively introduced here.

Since the dielectric constant, the conductivity, and the refractive index are inter related, knowing any one of them allows us to calculate the other two easily. In our research, usually the complex conductivity is used. From the complex refractive index, we can get the complex conductivity $\hat{\sigma} = \sigma_1 + i\sigma_2$ of the sample by using the equations

$$\sigma_1 = \epsilon_2\epsilon_0\omega = 2\epsilon_0\omega n\kappa, \tag{2.8}$$

$$\sigma_2 = -(\epsilon_1 - 1)\epsilon_0\omega = -\epsilon_0\omega(n^2 - \kappa^2 - 1), \tag{2.9}$$

where κ is the imaginary part of the complex refractive index ($\hat{n} = N + i\kappa$).

This allows us to get the THz conductivity of the samples without making contact to them.

2.3.2 Time-Resolved Terahertz Spectroscopy

Time-resolved terahertz spectroscopy (TRTS) utilizes an optical pump pulse to study the photoexcited properties in a sample. This is the reason why it is also called an optical pump-THz probe experiment. In semiconductor and nanotechnology research, the photoresponse of a material and the induced conductivity are quite important for understanding material properties and for applications. With the achievable short duration of THz pulses, many fast processes such as transient conductivity and carrier dynamics can be studied with sub-picosecond resolution [37, 54]. This is the main method used in this study on semiconductor samples.

In TRTS experiments, the schematic diagram of the setup is still the same one shown in Fig. 2.4, which is very similar to the setup for THz-TDS experiments, except that the optical pump beam is now involved. The optical pump beam is also split from the same pulsed laser source. The idea of this experiment is to use the optical pump pulse to photoexcite the sample, and then use the THz pulse to investigate the photoinduced properties in the sample.

Usually in time-resolved THz spectroscopy experiments, the THz pulse is focussed tightly at the sample to let the THz pulse transmit through a uniformly excited sample. A sample holder with an aperture is usually used, and the optical beam must be wide enough to cover the aperture uniformly. Most components of a tightly focused THz pulse can pass through a 1 mm-diameter aperture. For an aperture with a diameter larger than 1 mm, there is almost no loss of THz pulse. The optical pump pulse also goes through a delay stage that can be moved relative to both the THz pulse and the probe pulse.

To study the photoexcited carrier decay dynamics, the probe pulse is fixed to detect the peak of the THz pulse. Then the pump beam is moved relative to both the THz beam and the probe beam. We define the positive time delay as when the pump pulse arrives earlier than the THz pulse and probe pulse. The optical pump pulse excites free carriers and thus induces a change in conductivity of the sample. So, at positive delay time, the transmission of the THz peak will be reduced due to this conductivity. At negative delay

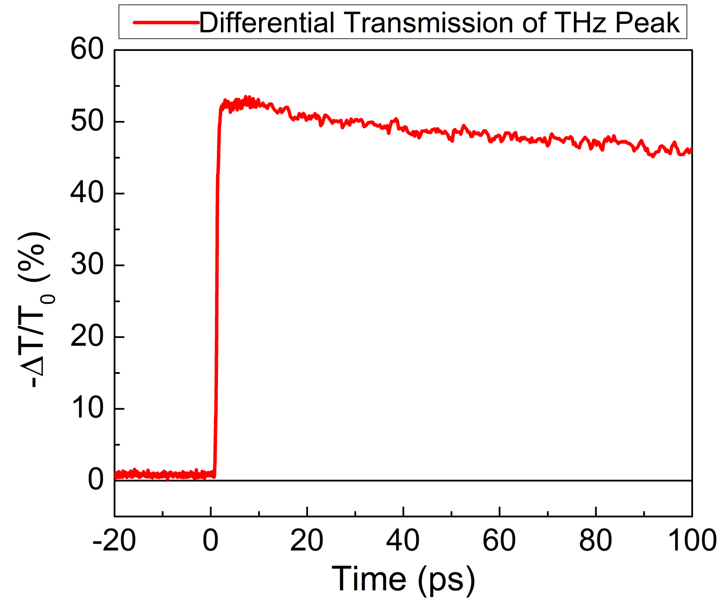

Figure 2.7: The negative differential terahertz transmission ($-\Delta T/T_0$) for a GaAs wafer with a pump fluence of 15 μJ/cm^2.

time, the THz probe pulse arrives at the sample before the optical pump pulse. The modulation in conductivity can be monitored by observing the negative differential THz transmission ($-\Delta T/T_0$) due to optical pump. A sample modulation scan performed on a GaAs wafer is shown in Fig. 2.7. The sample was excited with 800 nm pulses at a fluence of 15 μJ/cm^2. Since the GaAs wafer is a direct-gap semiconductor with band gap of 1.42 eV, interband transitions can be excited by any pulse with wavelength shorter than 870 nm. GaAs has a zincblende crystal structure (cubic structure with point group $\overline{4}3$m). It has been well studied by ultrafast THz spectroscopy and is frequently used as a reference sample in THz experiments. The modulation of GaAs at a fluence of 15 μJ/cm^2 is already very high because of the high induced conductivity in the sample. The decay time of GaAs is around a few hundred ps. We are able to observe the complete decay if the data is scanned over a longer time. One needs to be careful in using the modulation to analyse the optical and electric properties, as the intervalley scattering in GaAs influences the transmission of the terahertz pulse by a nonlinear response [20, 48, 55]. However, this doesn't influence our experiment, because $E_{\mathrm{THz}} < 1$ kV/cm is not high enough to induce a nonlinear response.

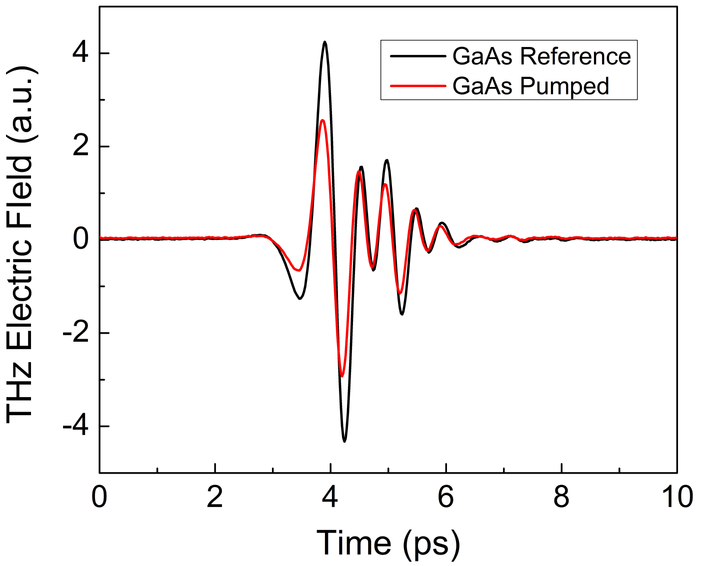

Figure 2.8: THz waveform through unexcited GaAs (black line) and GaAs (red line) at 50 ps after photoexcitation pumped by 800 nm pulse at 15 μJ/cm^2.

2.3.3 Transient Conductivity

To study the transient conductivity of the sample, the delay stage controlling the pump beam is moved to a position at positive delay time. For instance, the stage is fixed at a delay time of 50 ps, which means the pump pulse arrives 50 ps earlier than both the THz pulse and the probe pulse. If the THz pulse is scanned at this time, we will get the THz waveform through an photoexcited sample. The excited free carriers in the sample will reduce the transmission of the THz pulse. In Fig. 2.8, the THz pulses passing through unexcited and photoexcited samples are plotted. From the peak we see that the modulation in transmission is around 46%, which matches the negative differential THz transmission scan at 50 ps in Fig. 2.7. There is also a slight phase shift due to the transient conductivity in the pumped sample.

FFT is performed on the waveforms to get the frequency-dependent amplitude $E(\omega)$ and phase $\Phi(\omega)$ spectra. It is assumed that the transmission at the air-sample boundary doesn't change due to optical excitation to analyze the data, though the actual transmission might be very complicated [22]. The transient conductivity can be calculated from the modulation in transmission data. In previous studies, the transient conductivity in the GaAs wafer could

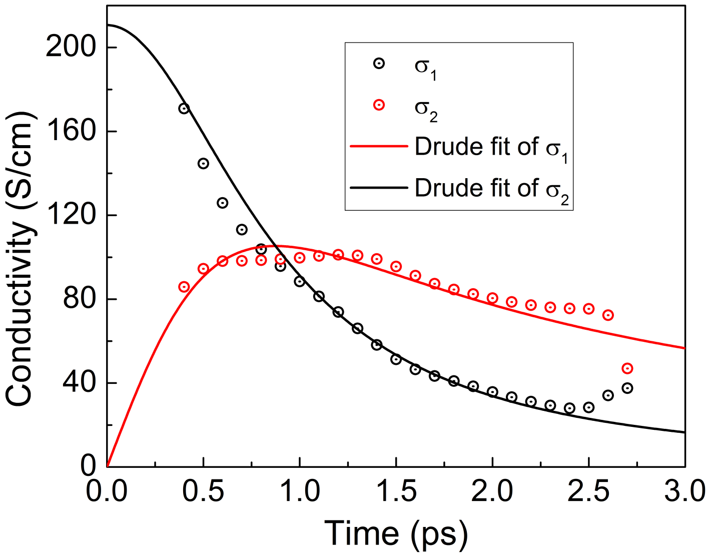

Figure 2.9: Transient conductivity data of GaAs wafer at 50 ps after photoexcited by an 800 nm pulse with a fluence of 15 μJ/cm^2. The solid lines are a theoretical fit to the Drude model.

be described well by a simple Drude model, with a long scattering time varying from 100 fs to 600 fs. The transient conductivity data extracted from the frequency-dependent FFT result is shown in Fig. 2.9.

As we can see in Fig. 2.9, the transient conductivity follows a simple Drude model (see Chapter 3) with high scattering time τ. All fits in this thesis were done using Origin. The best fit was determined by comparing the residual sum of squares. From the Drude fit, the plasma ordinary frequency $\nu_p(\omega)$ and the scattering τ have values of 18.2 ± 0.7 THz and 182 ± 3 fs. Since the optical penetration depth at 800 nm is around 820 nm, which is much longer than that at 400 nm in GaAs, the plasma frequency is lower than that pumped with 400 nm pulse at the same fluence [56]. From the Drude scattering time and the plasma frequency, the carrier mobility is calculated to be equal to 4780 ± 80 cm^2/Vs at a carrier density of $(2.7 \pm 0.1) \times 10^{17}$ cm^{-3}, which agrees with values from previous studies [19, 21, 50, 57].

Chapter 3

Data Interpretation and Conductivity Models

The Lorentz model, the Drude model, and its generalization the Drude-Smith model are introduced in this chapter. These three models will be used to interpret the data in the following chapters. Fitting parameters in these models allow us to deduce the optical and electrical properties of the samples. This chapter also introduces some commonly used ways to interpret the experimental data in thin films, especially the transient conductivity. From the waveforms and carrier decay dynamics from THz-TDS and TRTS, many properties of the samples can be extracted from these experimental data with proper methods. The validity of the approximation used to calculate the properties in thin film samples is tested with a simulation program that considers a wide range of conductivity data.

3.1 Drude Model

The Drude model was first proposed by Paul Drude, a German physicist, in 1900. Though it is a very simple model with many simplifying assumptions, it describes the carrier dynamics very well in many materials, especially metals and some doped semiconductors [58]. The key assumption made in the Drude Model is that electrons move in the material freely but can be scattered by other particles through collision at an average rate of $\frac{1}{\tau}$, where τ is the Drude relaxation time of the carriers. The details of collisions are not considered in this model. Though it describes a wide range of materials, it has to be modified to describe some specific materials [21].

With a DC or low frequency electric field E, the charge carriers drift at a velocity $v_D = \mu E$. The carrier mobility is defined as $\mu = \frac{e\tau}{m^*}$, where e is the electric charge, τ is the average time between two scattering events, and m^* is the effective mass of the carrier. The current density is

$$J_D = nev_D = \frac{ne^2\tau}{m^*}E, \tag{3.1}$$

where n is the carrier density. The corresponding DC conductivity is

$$\sigma_{DC} = \frac{J_D}{E} = \frac{ne^2\tau}{m^*} = \epsilon_0\omega_p^2\tau. \tag{3.2}$$

The carrier density n is then calculated using

$$n = \frac{\epsilon_0\omega_p^2 m^*}{e^2}, \tag{3.3}$$

where $\omega_p = \sqrt{\frac{ne^2}{\epsilon_0 m^*}}$ is the plasma frequency at that carrier density. The frequency dependent conductivity $\hat{\sigma}(\omega)$ is given by

$$\hat{\sigma} = \sigma_1 + i\sigma_2 = \frac{\sigma_{DC}}{1 - i\omega\tau}. \tag{3.4}$$

In Eq. 3.4, the imaginary term comes from the inertial response of the carriers in AC electric field. Therefore, the frequency-dependent conductivity contains a real part and an imaginary part:

$$\sigma_1 = \frac{\sigma_{DC}}{1 + (\omega\tau)^2}, \tag{3.5}$$

$$\sigma_2 = \frac{\sigma_{DC}\omega\tau}{1 + (\omega\tau)^2}. \tag{3.6}$$

At $\omega = 0$, we get $\sigma_1 = \sigma_{DC}$ and $\sigma_2 = 0$, when $\omega\tau = 1$, the real and imaginary conductivity coincide ($\sigma_1 = \sigma_2$). If the crossing point is too high as compared to the THz spectroscopy frequency range, it will make the fitting difficult because of the lack of available curvature. Fortunately, for most semiconductors and metals, the crossing point is within or near our THz spectroscopy frequency range (∼3 THz). The crossing frequency can be expressed as $f_c = 1/2\pi\tau$. For $\tau > 53$ fs, the crossing point is below 3 THz.

3.2 Lorentz Oscillator Model

The Lorentz oscillator model treats atoms as bound charges with polarizations that can interact with external electric fields. This idea was first raised by Dutch physicist Henrick Antoon Lorentz in 1878. In this model, the atomic motion is described by a classic damped harmonic oscillator in response to incident electromagnetic waves, which is

$$\mu\Big(\frac{\mathrm{d}^2x(t)}{\mathrm{d}t^2}+\gamma\frac{\mathrm{d}x(t)}{\mathrm{d}t}+\omega_0^2x\Big)=-eE(t), \tag{3.7}$$

where μ is the reduced mass and is approximately equal to the electron mass m_0, ω_0 is the natural frequency of the oscillator and γ is the damping rate ($\gamma=\frac{1}{\tau}$, where τ is the lifetime of the oscillator). A non-zero damping rate means the dipoles can energetically interact with other particles [41, 59].

If the electric field is in the form of $E(t)=E_0e^{-i\omega t}$, the displacement will also be in the similar form $x(t)=x_0e^{-i\omega t}$. Then the solution to this equation is

$$\chi_0=\frac{-eE}{m_0(\omega_0^2-\omega^2-i\gamma\omega)}. \tag{3.8}$$

From this result, we can get the polarization due to the dipole oscillation as

$$\vec{P}=-ne\chi_0=\frac{ne^2\vec{E}(\omega)}{m_0}\frac{1}{\omega_0^2-\omega^2-i\gamma\omega}, \tag{3.9}$$

where n is the number of atoms per unit volume in the material. Since we know that the electric displacement D is given by

$$\vec{D}=\epsilon_0\vec{E}+\vec{P}, \tag{3.10}$$

and for isotropic materials, the relative dielectric constant ϵ_r is defined through

$$\epsilon\epsilon_r\vec{E}=\vec{D}. \tag{3.11}$$

Solving these equations, we get

$$\hat{\epsilon}_r=\epsilon_1+i\epsilon_2=1+\frac{\omega_p^2}{(\omega_0^2-\omega^2)-i\omega/\tau} \tag{3.12}$$

where ω_p is the plasma frequency. Separating the real and imaginary parts of the relative dielectric constant, we get

$$\epsilon_1 = 1 + \frac{\omega_p^2(\omega_0^2 - \omega^2)}{(\omega_0^2 - \omega^2)^2 + (\omega/\tau)^2} \tag{3.13}$$

and

$$\epsilon_2 = \frac{\omega_p^2(\omega/\tau)}{(\omega_0^2 - \omega^2)^2 + (\omega/\tau)^2}. \tag{3.14}$$

Knowing the complex dielectric constants, we are able to get the complex conductivity [see Eq. 2.8 and Eq. 2.9] due to the dipole oscillation, which is

$$\sigma_1 = \frac{\epsilon_0\omega_p^2(\omega^2/\tau)}{(\omega_0^2 - \omega^2)^2 + (\omega/\tau)^2} \tag{3.15}$$

and

$$\sigma_2 = -\frac{\epsilon_0\omega_p^2\omega(\omega_0^2 - \omega^2)}{(\omega_0^2 - \omega^2)^2 + (\omega/\tau)^2}. \tag{3.16}$$

Notice that the Drude model conductivity is recovered when we set $\omega_0 = 0$.

3.3 Drude-Smith Model

The Drude model is very successful in describing traditional metals with only one parameter τ introduced in the model. But it fails to describe some nanostructured materials that have low DC conductivity. In order to develop a model that can cover all these behaviors, many efforts in generalizing the Drude model have been made over the past years. A very simple and powerful generalization of the Drude model is the Drude-Smith model developed by N. V. Smith [60]. In the Drude-Smith model, one more parameter, c_n, is introduced to describe the persistence of carrier velocity. Its value represents the fraction of the carriers' velocity which is retained after n collisions. Using Poisson statistics, the expression of conductivity is derived. The full form of the equation is

$$\tilde{\sigma} = \frac{\sigma_{DC}}{1 - i\omega\tau}\left[1 + \sum_n \frac{c_n}{(1 - i\omega\tau)^n}\right], \tag{3.17}$$

where σ_{DC} is the DC conductivity in the Drude model (Eq. 3.2).

In most studies to date [29, 60, 61] only the first order correction is used with $c_1 = c$, called the Drude-Smith c-parameter. The real and imaginary

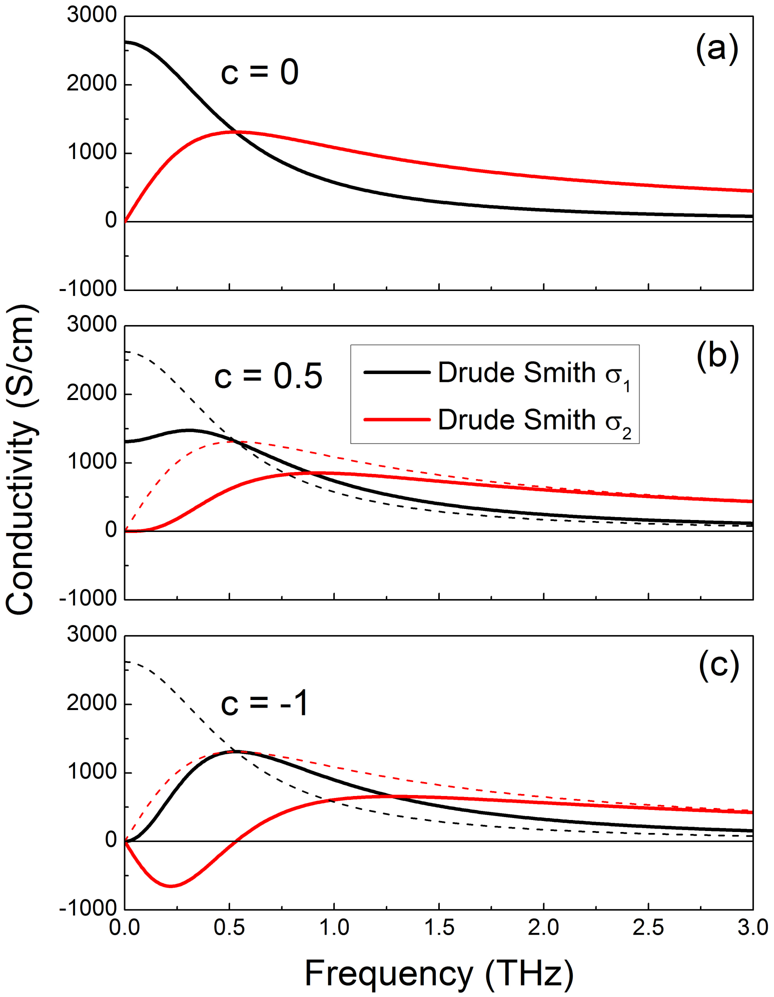

Figure 3.1: A comparison between Drude-Smith conductivities with (a) $c = 0$ (b) $c = -0.5$ (c) $c = -1$. The data is plotted with $\tau = 300$ fs and $\omega_p = 3.14 \times 10^{14}$ rad/s. The solid lines are the Drude-Smith conductivities with corresponding value of c. The dash lines in (b) and (c) are the conductivity with $c = 0$.

conductivities are given by

$$\sigma_1 = \frac{\sigma_{DC}}{\big[1+(\omega\tau)^2\big]^2}\big[1+(\omega\tau)^2 + c\big(1-(\omega\tau)^2\big)\big] \tag{3.18}$$

and

$$\sigma_2 = \frac{\sigma_{DC}\omega\tau}{\big[1+(\omega\tau)^2\big]^2}\big[1+(\omega\tau)^2 + 2c\big], \tag{3.19}$$

where c ranges from 0 to -1. At $\omega = 0$, the real conductivity is suppressed by a factor of $1+c$, which is quite common in poor metals and nano-crystalline materials. The imaginary conductivity can become negative when $c < -0.5$. A sample conductivity with three different c values is shown in Fig. 3.17.

The value $c = 0$, corresponds to the simple Drude model. We see that when $c = -1$, the low frequency real conductivity is fully suppressed, due to strong carrier localization, therefore it is not conducting when $\omega = 0$. This behavior is commonly seen in many nano-wires [28], nano-crystalline gains [27, 61, 62], nano-structured materials [29, 63, 64], and some poorly conducting alloys [65]. It is one of the most successful generalizations that can cover a wide range of materials. It's most widely used to describe the effect of localization in many materials [28, 66, 67].

3.4 Conductivity of Thin-Film Samples

Many samples are made in the form of a thin film with a surface conductivity $\hat{\sigma}_s(\omega)$ on a semi-insulating substrate. From this kind of sample, one can extract the conductivity, carrier concentration and even the mobility simply from the modulation in the transmission of the THz pulse through the thin conducting film [14]. This method will be introduced in this section.

When the film thickness is much smaller than the THz wavelength ($d \ll \lambda$) and the THz pulse is at normal incidence to the sample, Maxwell's equations become

$$\oint_P \vec{E}(\omega)\cdot \mathrm{d}\vec{l} = -\frac{\mathrm{d}}{\mathrm{d}t}\int_S \vec{B}(\omega)\cdot \mathrm{d}\vec{a} \tag{3.20}$$

and

$$\oint_P \frac{\vec{B}(\omega)}{\mu}\cdot \mathrm{d}\vec{l} = I_f + \frac{\mathrm{d}}{\mathrm{d}t}\int_S \epsilon\vec{E}(\omega)\cdot \mathrm{d}\vec{a}, \tag{3.21}$$

which gives us the boundary conditions

$$E_0(\omega) - E_r(\omega) - E_t(\omega) = 0 \tag{3.22}$$

and

$$\frac{B_0(\omega)}{\mu_0} + \frac{B_r(\omega)}{\mu_0} - \frac{B_t(\omega)}{\mu_s} = J_f(\omega), \tag{3.23}$$

where $E_0(\omega)$, $E_r(\omega)$, and $E_t(\omega)$ are the incident, reflected, and transmitted fields; $J_f(\omega)$ is the surface current density; and μ_s is the permeability of the substrate. In most substrates, the permeability is approximately equal to the permeability of free space μ_0. Substituting $J_f(\omega) = \hat{\sigma}_s(\omega)E_t(\omega) = \hat{\sigma}(\omega)dE_t(\omega)$ (where $\hat{\sigma}_s$ is the surface conductivity, $\hat{\sigma}$ is the conductivity, and d is the thickness of the film) and dividing both sides of Eq. 3.22 and Eq. 3.23 by $E_0(\omega)$ we get

$$1 - R(\omega) - T(\omega) = 0 \tag{3.24}$$

and

$$1 + R(\omega) - \sqrt{\epsilon_r} \cdot T(\omega) = \hat{\sigma} d \sqrt{\frac{\mu_0}{\epsilon_0}} \cdot T(\omega), \tag{3.25}$$

where $R(\omega)$ and $T(\omega)$ are the reflectance and transmittance. Solving these two equations for $T(\omega)$, we have

$$T(\omega) = \frac{E_t(\omega)}{E_0(\omega)} = \frac{2}{1 + N + Z_0\hat{\sigma}(\omega)d}, \tag{3.26}$$

where $Z_0 = \sqrt{\frac{\mu_0}{\epsilon_0}} = 377\ \Omega$ is the impedance of free space, and $N = \sqrt{\epsilon_r}$ is the refractive index of the substrate [13]. The ratio of transmission between excited sample and unexcited sample is

$$\frac{T_s(\omega)}{T_0(\omega)} = \frac{E_s(\omega)}{E_0(\omega)} = \frac{1 + N}{1 + N + Z_0\hat{\sigma}(\omega)d}, \tag{3.27}$$

which can be used to solve the transient conductivity and to extract experimental data [14, 63, 68].

By reversing Eq. 3.27, we are able to calculate the transmission ratio of reference pulse and pumped pulse from the frequency dependent conductivity:

$$\frac{E_0(\omega)}{E_s(\omega)} = \left[1 + \frac{Z_0\sigma_1(\omega)d}{1 + N}\right] + i\left[\frac{Z_0\sigma_2(\omega)d}{1 + N}\right] \tag{3.28}$$

Since the frequency dependent wave spectrum can be separated into the amplitude, $A(\omega)$, and the phase, $\phi(\omega)$, in the form of

$$E(\omega) = A(\omega)e^{i\phi(\omega)}. \tag{3.29}$$

Substituting this into Eq. 3.27 and separating the real and imaginary parts, we have two equations which can be used to solve the amplitude and phase of the THz pulse transmitted through thin conducting film:

$$\frac{A_0(\omega)}{A_s(\omega)}\sin[\phi_0(\omega) - \phi_s(\omega)] = \frac{Z_0\sigma_2 d}{1+N} \tag{3.30}$$

and

$$\frac{A_0(\omega)}{A_s(\omega)}\cos[\phi_0(\omega) - \phi_s(\omega)] = 1 + \frac{Z_0\sigma_1 d}{1+N}. \tag{3.31}$$

From these equations, the real and imaginary conductivities are extracted:

$$\sigma_1(\omega) = \frac{1+N}{Z_0 d}\frac{A_0(\omega)}{A_s(\omega)}\sin[\phi_0(\omega) - \phi_s(\omega)] \tag{3.32}$$

and

$$\sigma_2(\omega) = \frac{1+N}{Z_0 d}\left(\frac{A_0(\omega)}{A_s(\omega)}\cos[\phi_0(\omega) - \phi_s(\omega)] - 1\right). \tag{3.33}$$

Therefore the complex conductivity can easily be extracted from the sample and reference THz waveforms taken in TRTS experiments.

Eq. 3.32 and Eq. 3.33 are derived for thin films with no background conductivity. For some of the materials, the sample has a background conductivity even though there is no photoexcitation. The background conductivity will influence the extraction of photoexcited conductivity. For such a case, the equations need to be modified and are very complicated. The full derivation is shown in Appendix A. Fortunately, the background conductivity influences the extraction of the photoinduced conductivity only when the background conductivity is significant or there are Lorentz oscillators in the studied frequency range. The influence of background conductivity of the FeS_2 films is negligible.

When the modulation in transmission is mainly due to amplitude modulation rather than phase shift, *i.e.*, $\sigma_1 > \sigma_2$ or $\omega\tau < 1$ (as in a predominantly resistive film in the THz frequency range), Eq. 3.27 can be simplified to a frequency-independent form and related to the transmission data collected in

TRTS experiments [69]. The conductivity calculated from the transmission data could be used to estimate the real conductivity at low frequency. It is more common to write out the ratio between the negative differential transmission and the reference transmission, which from Eq. 3.27 is

$$-\frac{\Delta T}{T_0} = \frac{Z_0 \sigma d}{1+N+Z_0\sigma d} = 1 - \frac{1+N}{1+N+Z_0\sigma d}, \tag{3.34}$$

where T_0 is the transmission without optical pumping, ΔT is the differential transmission caused by optical pumping, and $\sigma_1 \gg \sigma_2$ is assumed. After rearranging, we get the conductivity of the sample as a function of negative modulation $-\Delta T/T$, which is

$$\sigma_{\Delta T} = \Big(\frac{1+N}{Z_0 d}\Big)\Big(-\frac{\Delta T}{T_0}\Big)\Big[\frac{1}{1-(-\frac{\Delta T}{T_0})}\Big]. \tag{3.35}$$

Simply from the negative modulation of the peak THz pulse transmission induced by optical pump pulse, we are able to get the transient conductivity of the sample using this equation. As in the optical pump-THz probe experiment, $-\Delta T/T_0$ is scanned over different delay times. From that, we can see how the induced conductivity decays as time elapses. When the modulation is small (usually $|\Delta T/T_0| < 20\%$), the conductivity is approximately proportional to the negative modulation of transmission

$$\sigma_{\Delta T} \cong \Big(\frac{1+N}{Z_0 d}\Big)\Big(-\frac{\Delta T}{T_0}\Big). \tag{3.36}$$

Since $\sigma_{\mathrm{DC}} = ne\mu$, where μ is the carrier mobility, the carrier density n can also be calculated directly from $-\frac{\Delta T}{T_0}$ in this approximation using

$$n = \Big(\frac{1+N}{e\mu Z_0 d}\Big)\Big(-\frac{\Delta T}{T_0}\Big)\Big[\frac{1}{1-(-\frac{\Delta T}{T_0})}\Big]. \tag{3.37}$$

The maximum modulation in optical pump-THz probe experiments is related to the maximum conductivity and therefore the maximum carrier density, too. The carrier density can be related to the optical pump fluence by including the quantum efficiency η and the maximum possible carrier density, which is

$$n = \eta n_{\max} = \eta \frac{F_{\mathrm{pump}}}{h\nu_{\mathrm{pump}} d}, \tag{3.38}$$

where F_{pump} is the optical pump fluence, h is the Planck constant, and d is the thickness of the photoexcited film. Equating Eq. 3.37 at maximum modulation $|\Delta T/T_0|_{\max}$ with Eq. 3.38, the product of carrier mobility and quantum efficiency can be expressed as a function of $|\Delta T/T_0|_{\max}$,

$$\eta \cdot \mu = \frac{(1+N)h\nu_{\text{pump}}}{Z_0 e F_{\text{pump}}}\Big(\frac{1}{1-\left|\frac{\Delta T}{T_0}\right|_{\max}} - 1\Big). \tag{3.39}$$

Letting the quantum efficiency be 1, we get a lower boundary of the carrier mobility [69]. Though it is not easy to get a value of quantum efficiency and thus an exact value of mobility, this lower boundary is still useful in comparing with the mobility extracted in other experiments.

3.5 Simulation of THz Pulse Transmission through A Conducting Thin Film

The equations for thin films introduced in the last section are very useful in analysing the data collected in time-resolved terahertz spectroscopy, considering that many semiconductor samples are now fabricated in the form of thin films coated on semi-insulating substrates. From the photoinduced modulation of the THz pulse transmission measured in a TRTS experiment, the conductivity, the carrier density and the carrier mobility can be calculated.

Though this method is quite powerful, its accuracy is limited by the resistive film approximation used in the development of the equations. The resistive film approximation assumes that $\sigma_1 \gg \sigma_2$, *i.e.*, the modulation of the transmission is mainly due to absorption rather than a phase shift of the THz pulse. To test the accuracy of the approximation equations under different conditions, a simulation program that allows us to define different conductivities of thin films is developed.

The program was written in LabVIEW to simulate a THz waveform transmitting through a conducting thin film with different conductivity models. It first reads a reference THz pulse that is transmitted through the reference substrate. The program then allows the user to change the conductivity of the thin film. By inputting the values of ω_p, τ and c, substrate refractive index N, film thickness and d, thin films with both Drude and Drude-Smith conductivities can be simulated for testing. Based on this information, the THz waveform transmitted through the conducting thin film is calculated. From these two waveforms, we can see how significant the phase shift is, and judge how close the conductivity calculated from the approximation is to the actual conductivity. The full description of the program is in Appendix B.

To test the program, we simulate a THz waveform transmitted through a conducting film with certain values of ω_p, τ, c, d, and N. We then save the simulated waveform along with the reference one and put them in the analysis program that is used to extract the complex conductivity data from TRTS experiments. The extracted complex conductivity data exactly matches the data we input in the simulation program, which means that our simulation result is reliable.

The ultimate goal of this program is to see whether the conductivity calculated using Eq. 3.35 matches the conductivity derived from the conductivity spectra at the same time delay. The conductivity calculated from the approximation in Eq. 3.35 is frequency independent while the complex conductivity of the film is actually frequency dependent. The THz transmission is measured at the peak of the THz pulse, and we see from the Fourier Transform of the THz pulse that most of the THz components are around 1 THz. So, the transmission of the THz pulse through a thin film with conductivity $\hat{\sigma}(\omega) = \sigma_1(\omega) + i\sigma_2(\omega)$ is sensitive to the complex conductivity at 1 THz. As a result, it is reasonable to compare the approximated conductivity, $\sigma_{\Delta T}$ from Eq. 3.35, to the actual conductivity, σ_a, that is extracted from the complex conductivity at 1 THz.

3.6 Validity of the Resistive Film Approximation and Simulation Results

It is necessary to know how the resistive film approximation may influence the interpretation of results. Since no one has checked this in detail in our group, the accuracy of the approximation was tested with different complex conductivities before the equations were used in the following chapters.

3.6.1 Influence of the Drude Scattering Time and Carrier Localization

Considering all the parameters, the Drude scattering time, τ, influences the resistive film approximation the most. When $f > f_c = 1/2\pi\tau$, the imagi-

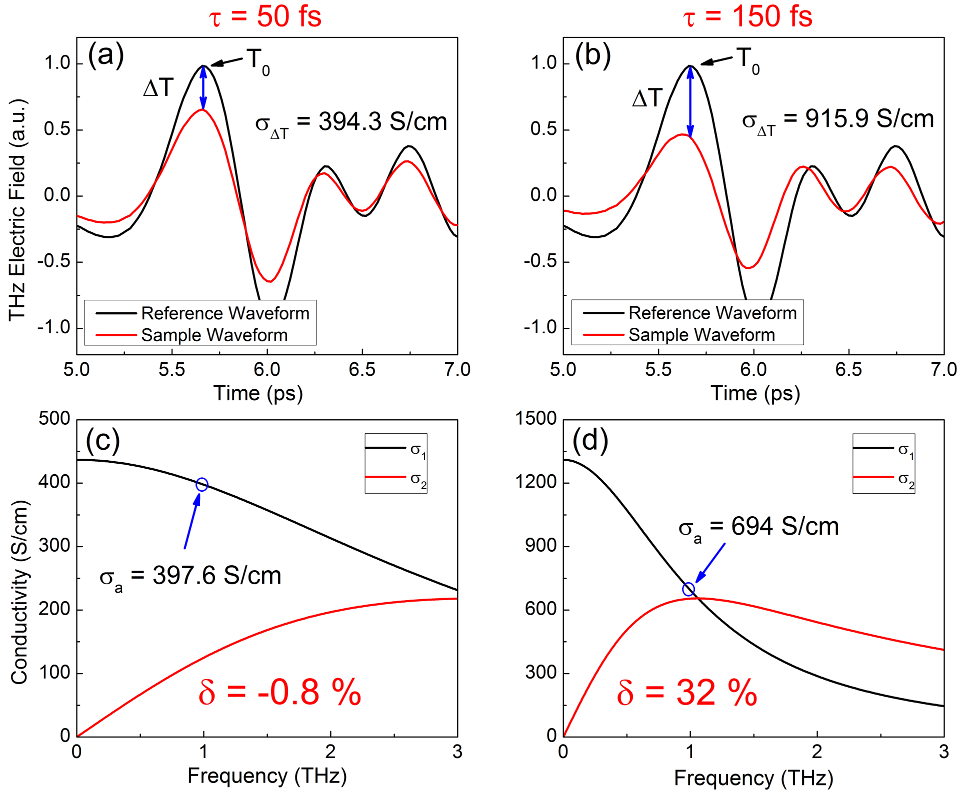

Figure 3.2: Simulated results with $\tau = 50$ fs and $\tau = 150$ fs for testing the accuracy of conductivities calculated with the resistive film approximation. The upper graphs (a), (b), show the reference THz waveform and the simulated THz waveform in each case. The lower graphs (c), (d), are the corresponding conductivity spectra. The transmitted wave is simulated with the parameters $\nu_p = 50$ THz, $c = 0$, $N = 2$ and $d = 100$ nm. The THz differential transmission ΔT is indicated by the blue double-headed arrows, from which $\sigma_{\Delta T}$ is calculated using Eq. 3.35. Single-headed blue arrows indicate the value of σ_a, which is regarded as the expected value of $\sigma_{\Delta T}$ in the approximation.

nary conductivity is higher than the real conductivity, thus the approximation breaks down. For $\tau > 159$ fs, the crossover point is below 1 THz. In such a case, the THz pulse transmitted through the conducting film will be significantly shifted in the time domain. The conductivity calculated from the negative differential transmission $\Delta T/T_0$ will contain errors caused by the phase shift. In the program, the accuracy is assessed by showing the discrepancy, $\delta = (\sigma_{\Delta T} - \sigma_a)/\sigma_a$. An example is shown in Fig. 3.2 with $\tau = 50$ fs and $\tau = 150$ fs. The conductivity spectra are produced from the values of ν_p, τ, and c input by the user. Based on the conductivity spectra, the reference THz

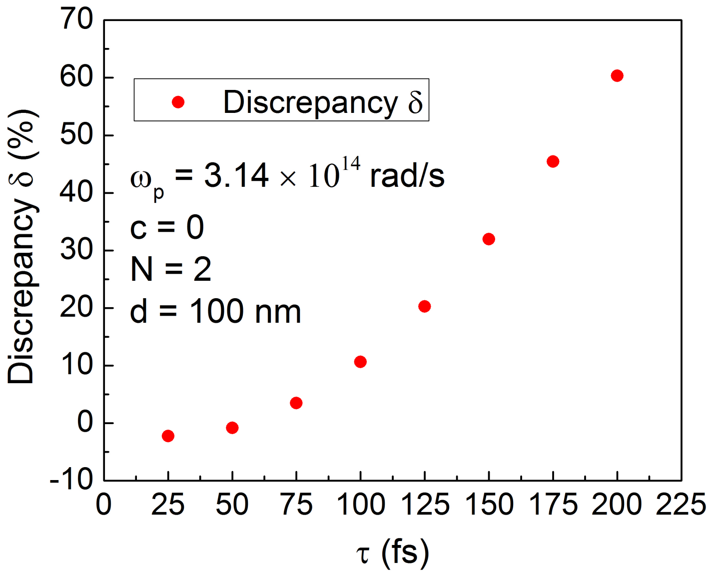

Figure 3.3: Discrepancy δ resulting from the resistive film approximation with different Drude scattering time.

waveform, and the properties of the substrate, the THz waveform transmitted through the thin conducting film is simulated.

In a real differential transmission scan (see Fig. 2.7 for example), the probe pulse is fixed at the peak of the reference THz waveform, and the differential transmission ΔT is measured for a range of delay times. Therefore, the ΔT shown in Fig. 3.2 actually corresponds to one time point in a differential transmission scan. If there is a significant phase shift, the error in measuring ΔT will lead to an inaccurate value of $\sigma_{\Delta T}$ calculated by using Eq. 3.35. From the graph, we see that the σ_1 is always higher than σ_2 in the plotted frequency range when $\tau = 50$ fs. At 1 THz, σ_1 dominates. As a result, there is barely any phase shift of the transmitted THz waveform. And the conductivity $\sigma_{\Delta T}$ calculated from the resistive film approximation is very close to the expected real conductivity σ_a at 1 THz, leading to a small discrepancy of -0.82%. When $\tau = 150$ fs, σ_2 is comparable to σ_1 around 1 THz, and the phase shift is not negligible. From Fig. 3.2 we see that the ΔT is measured from the peak of the reference THz waveform to a non-peak position of the transmitted THz waveform. Based on this ΔT, the conductivity calculated is 915.9 S/cm, which is 31.97% higher than the value obtained from the conductivity spectrum.

The discrepancies at different values of τ are shown in Fig. 3.3. We see that

N	d [nm]	ν_p [THz]	τ [fs]	c	σ_a [S/cm]	$\sigma_{\Delta T}$ [S/cm]	δ [%]
2	100	50	50	0	397.6	394.3	-0.82
2	100	50	50	-0.2	332.4	326.1	-1.89
2	100	50	50	-0.5	234.5	227.5	-2.99
2	100	50	50	-0.7	169.3	164.7	-2.68
2	100	50	50	-1	71.4	75.9	6.32
2	100	150	50	0	694	915.9	32
2	100	150	50	-0.2	685.8	806.1	17.5
2	100	150	50	-0.5	673.5	666.4	-1.1
2	100	150	50	-0.7	665.3	591.8	-11.1
2	100	150	50	-1	653	513.4	-21.4

Table 3.1: The influence of the first order Drude-Smith parameter c on resistive film approximation result.

the approximated result gets worse when the scattering time τ is above 100 fs. For $\tau < 100$ fs, the phase shift of the THz pulse can be negligible, while for $\tau > 100$ fs, the phase shift is at least tens of femtoseconds and can be as high as hundreds of femtoseconds. When the phase shift is significant, the negative differential transmission measured in TRTS experiments is not simply caused by amplitude attenuation, because now the modulation is measured from the reference THz peak to a position slightly off from the peak of the THz pulse transmitted through the conducting film. From the simulation result we see that the resistive film approximation can only be used for samples with a short Drude scattering time.

The approximation has been tested with more values of τ from 25 fs to 400 fs. For many organic or nanostructured semiconductor samples, the Drude scattering time τ is quite short due to impurities and boundaries of nanograins. Most of these samples show scattering times below 100 fs. Therefore, the resistive film approximation should work very well on these kind of samples. Many pure semiconductors or large single crystal samples have very long scattering times. For example, single crystal gallium arsenide (GaAs) has scattering times of several hundred femtoseconds even at high carrier densities. For these kinds of samples, the equations derived from the resistive film approximation should not be used to extract their optical and electrical properties.

The resistive film approximation was made in the context of the Drude model. However, in this thesis, a frequently used model is the Drude-Smith model (Section 3.3). The Drude-Smith model reduces to the Drude model when $c = 0$. Different values of c from 0 to -1 have been tested in the program

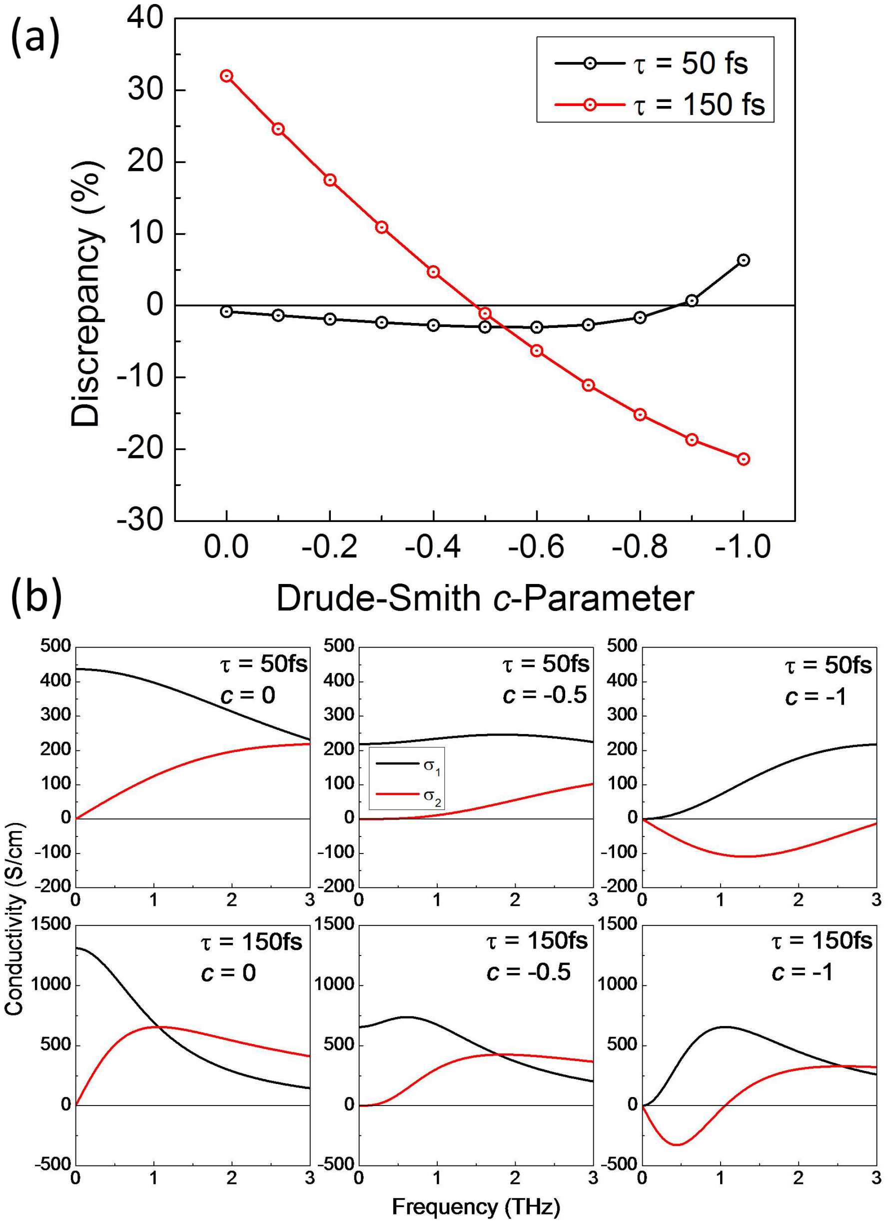

Figure 3.4: (a) Discrepancy δ resulted from the resistive film approximation with different Drude scattering time. (b) Conductivity spectra with different values of τ and c.

N	d [nm]	ν_p [THz]	τ [fs]	c	σ_p [S/cm]	$\sigma_{\Delta T}$ [S/cm]	δ [%]
3.1	14.5	53.3	72.6	0	597	572	-4.1
3.1	14.5	75.9	59.7	0	1054	1020	-3.2
3.1	14.5	98.5	48.9	0	1515	1473	-2.8
3.1	14.5	130.5	41.0	-0.1	2088	2038	-2.4
3.1	14.5	174.3	35.5	0	3590	3533	-1.6
3.1	14.5	227	31.5	-0.37	3591	3536	-1.5
3.1	14.5	301	28.1	-0.32	6034	5964	-1.2

Table 3.2: The resistive film approximation simulation results based on real experimental data measured from a silicon-on-sapphire film.

to see how the resistive film approximation works for the Drude-Smith model. In Fig. 3.4, it shows the discrepancies of the relative film approximation at different values of c with $\tau = 50$ fs and $\tau = 150$ fs. Other parameters were set constant at $\nu_p = 50$ THz, $N = 2$, and $d = 100$ nm.

The simulation results indicate that the resistive film approximation works very well for Drude-Smith conductivity at short Drude scattering time, with discrepancies below 7%. While the discrepancies can be as high as 32% with longer Drude scattering time. As a conclusion, the accuracy of the resistive film approximation is mainly influenced by the Drude scattering time. The extent of carrier localization has much smaller impact on the approximation.

3.6.2 Accuracy of the Resistive Film Approximation in Real Cases

When the GaAs wafer is pumped with an optical pulse, the surface of GaAs becomes conducting with a thickness much smaller than the THz wavelength. Therefore, we can assume that the sample is a thin conducting film on a substrate. For example, the transient conductivity of GaAs, pumped with 800 nm pulses at 15 μJ/cm^2, shows a plasma frequency $\nu_p = 18.2$ THz and Drude relaxation time $\tau = 182$ fs. Using this data and having the film thickness $d = 820$ nm, the result from the simulation shows that the peak of the reference THz waveform and the transmitted waveform are displaced by 20 fs, which makes the experimentally measured differential transmission different from the actual peak-to-peak modulation by 2.3%. But the conductivity calculated from the approximation using Eq. 3.35 is 130 S/cm, which is 42.4% higher than the expected value of 91.3 S/cm at 1 THz. This is expected as the single crystal

N	d [nm]	ν_p [THz]	τ [fs]	c	σ_p [S/cm]	$\sigma_{\Delta T}$ [S/cm]	δ [%]
2.15	44.4	26.8	53	-0.929	31	27	-13.01
2.15	44.4	36	44	-0.91	41	38	-5.76
2.15	44.4	49	39	-0.926	55	55	0.41
2.15	44.4	62	34	-0.93	66	69	4.99
2.15	44.4	73	31	-0.924	80	86	7.16
2.15	44.4	78	30.7	-0.92	92	96	7.73
2.15	44.4	87	30	-0.914	114	124	8.59
2.15	44.4	84	31.5	-0.903	123.39	132.17	7.12

Table 3.3: The resistive film approximation simulation results based on real experimental data measured from a FeS_2 nanocrystalline film.

GaAs has a very high Drude scattering time, which is the most dominating factor affecting the resistive film approximation.

The parameters measured in a TRTS experiment on a silicon-on-sapphire film are tested and shown in Table 3.2. The results in the table show that the approximation works very well for the silicon-on-sapphire in a wide range of conductivities as it has short Drude scattering time. As the Drude scattering time decreases when the carrier density increases in this sample, the approximation gives very low discrepancy at high carrier density.

Our FeS_2 films show Drude-Smith conductivity with very strong localization when excited by optical pulses. As the resistive film approximation is frequently used for this material, the data from this material is tested. The results are shown in Table 3.3. Because the FeS_2 samples have significant c values around -0.9, the real conductivity is highly suppressed in the low frequency range. As previously studied, the localization doesn't influence the accuracy of the resistive film approximation. For most of this data, the deviation is less than 10%.

Of all the three samples tested in this thesis, only the GaAs has a high Drude scattering time that limits the use of equations developed from the resistive film approximation. The short Drude scattering times of silicon-on-sapphire and FeS_2 films allow the use of the approximation with very small discrepancies. However, if extremely low excitation fluence is used in the TRTS experiment, it might generate a low carrier density with very long scattering times. It is recommended that the approximation is tested in the program before it is applied on new materials.

Chapter 4

Experimental Setup and Procedure

4.1 Ti:Sapphire Pulsed Laser Source

An ultrashort laser source is necessary in ultrafast THz spectroscopy. In this project, an amplified femtosecond Ti:sapphire laser source was used to generate THz pulses, detect THz pulses, and also optically excite the semiconductor samples being studied. This amplified femtosecond Ti:sapphire laser source contains four main parts: a Ti:sapphire seed laser (Kapteyn-Murnane Model TS Ti:sapphire laser kit) and its corresponding pump laser (Millennia Diode-pumped, cw Visible Laser), and an amplifier system (Multipass Femtosecond Ti:Sapphire Amplifier System) and its pump laser (Quantronix Odin 117).

Pumped by the Millennia continuous-wave laser at 532 nm at 3.7 W, the Ti:sapphire seed laser operates mode-locked to produce 60 fs ultrashort pulses peaked around 800 nm at a repetition rate about 80 MHz. This beam has power around 350 mW, which is too weak for direct use in ultrafast THz spectroscopy. As a result, pulses are picked out at a repetition rate of 1.04 kHz and sent through the multi-path femtosecond Ti:sapphire amplifier for energy amplification. The multipass femtosecond Ti:Sapphire amplifier also needs a pump laser to operate. Pumped by the Quantronix Model 117 laser, the multipath femtosecond Ti:sapphire amplifier amplifies the laser energy from about 4 nJ in the seed pulse to about 750 μJ in 100 fs in the amplified pulse. Though the power is amplified, the repetition rate is still 1.04 kHz. Very stable pulses are required at the output of the amplifier system, as the ultrafast THz spectroscopy requires identical THz pulses all the time. The amplified beam is split into three beams: a high power beam (80%) for optical pumping, a medium power beam (16%) for generating THz pulses and a low power beam (4%) for detecting THz pulses.

4.2 Generating and Detecting THz Pulses

Optical rectification and electro-optic sampling are used to generate and detect THz pulses in our study [40, 70]. The THz pulse is generated by optical rectification in a 0.5 mm thick ⟨110⟩ zinc telluride (ZnTe) crystal [71]. The 800 nm THz source beam is directed through a window to the ZnTe crystal to generate THz pulses. With a 100 femtosecond wide pulse incident on the 0.5 mm-thick ZnTe crystal, the sub-picodecond THz pulse has frequency components from 0.2 THz to 2.7 THz and is peaked at 1 THz [31]. The THz emission depends on both the crystal orientation and the laser pulse polarization. The azimuthal angle between the crystal axis and the polarization of the laser pulse is chosen to maximize the THz emission. After the THz pulse is generated, the pulse goes through a wire-grid polarizer to remove unwanted polarization components. The THz beam is expanded to 2" in diameter and is then focused by using off-axis parabolic mirrors to get smaller focal point on the sample. After transmitting through the sample, the THz pulse is then focused again onto another 0.5 mm ZnTe crystal for detection.

Free-space electro-optic sampling is used to detect the THz pulses. In electro-optic sampling, the THz pulse passes through the ZnTe crystal. A quarter wave plate is used to circularly polarize the probe beam. Then the circularly polarized beam goes through a Wollaston Prism and is separated into two equally powered beams of opposite polarization which are then detected by two balanced detectors. When there is a THz pulse incident on the ZnTe crystal, the birefringence induced in the ZnTe crystal changes the polarisation of the probe beam. As a result, the elliptically polarized probe beam going through the Wollaston Prism now is separated into two beams with different intensities. From this difference, we can calculate the strength of the THz electric field. All the THz source, THz detection crystal and the sample are put in a vacuum chamber as shown in Fig. 4.1.. The vacuum chamber allows the attachment of the sample to a cold finger, avoids absorption of THz by water vapour [72] and prevents sample degradation [73, 74].

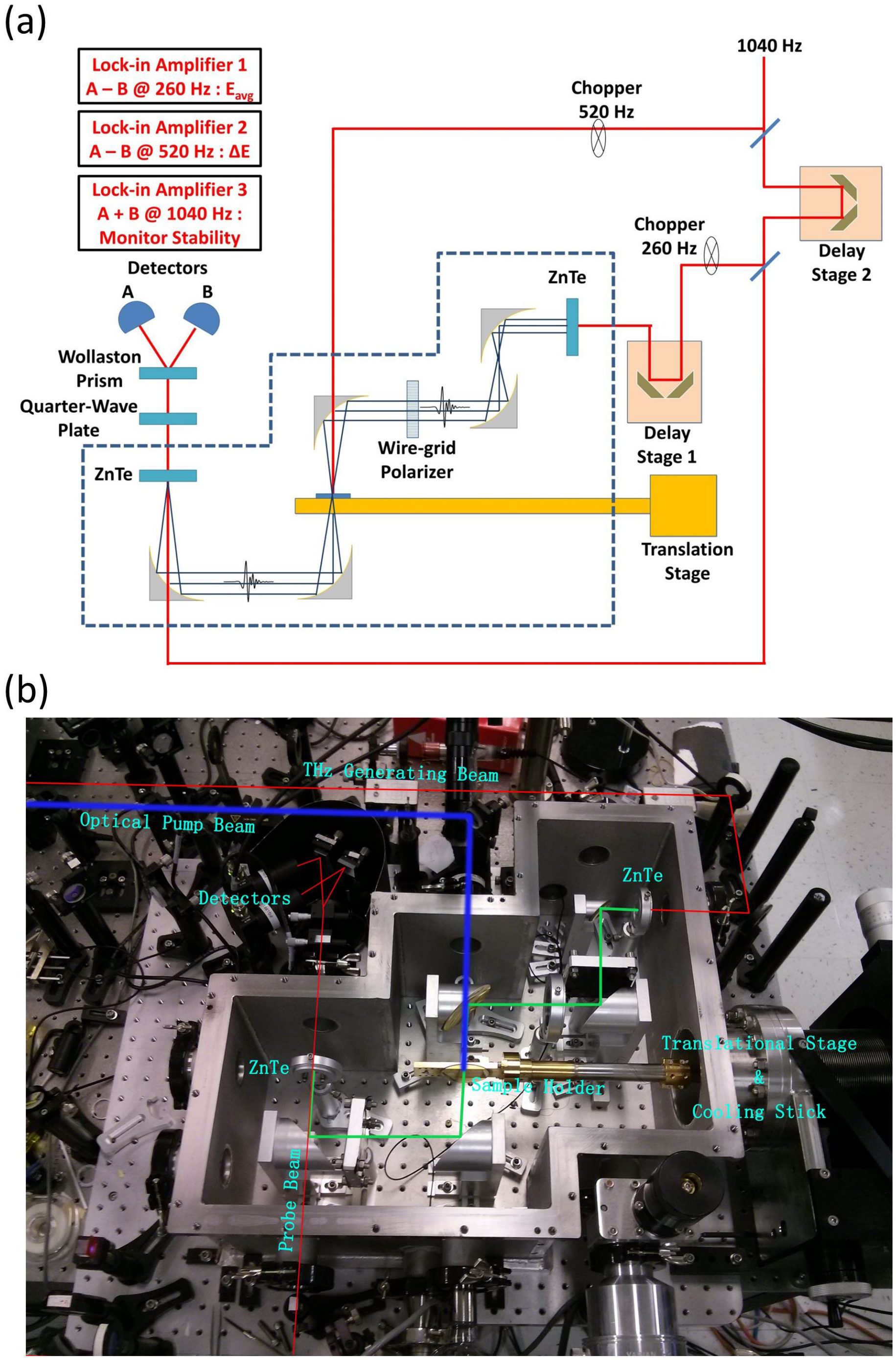

Figure 4.1: (a) Schematic diagram of the ultrafast THz spectroscopy setup. The dashed blue line indicates the area enclosed by the vacuum chamber. (b) Picture of the ultrafast THz spectroscopy setup. Solid red lines are the paths of the THz source beam and the sampling beam. The bold solid blue line is the path of the optical pump beam. The solid green line is the path of the THz beam.

4.3 Two-Channel Data Acquisition System

In our THz spectroscopy setup, two delay stages are used to control the time delay between the THz beam, the probe beam and the optical pump beam. The THz source beam goes through a ultrafine delay stage (Stage 1) which can move relative to the sampling beam and is used to scan the THz waveform. In 1 ps, light only travels 300 μm. With the delay stage, we routinely use time resolution of 20 fs using a 3 μm step size in the stage. Both the THz source beam and the sampling beam go through another delay stage (Stage 2). This stage can move relative to the optical pump beam, which controls the relative delay of the optical pump beam.

If the beam paths of these pulses are set to the correct length, the THz waveforms can be mapped out by moving the Stage 1. Then if the sampling pulse is moved to the THz pulse peak, the modulation in transmission of the THz pulse through the sample can be monitored by moving Stage 2 alone. When the pump pulse arrives at the sample later than the THz pulse, the transmission of the THz peak (T_0) is unchanged. When the pump pulse arrives earlier than the THz pulse, the transmission changes since the THz pulse now sees a photoexcited sample. Scanning through a range of delay times gives a time resolved modulation of transmission, as shown in Fig. 2.7. At negative time delay, scanning Stage 1 only gives the reference THz pulse. While if Stage 2 is at positive delay time, scanning Stage 1 gives the THz pulse transmission through the photoexcited sample and also the reference pulse.

While doing time-resolved THz spectroscopy, two waveforms are measured: one travelling through the excited sample and another to act as the reference waveform without excitation. Unfortunately, it takes a long time (about 30 minutes) to measure a complete THz waveform with low noise. If these two waveforms are measured in sequence, the measurement may not be that accurate due to fluctuations in laser power. To overcome this issue, a two-channel data acquisition system is used in our TRTS experiment, which measures the pumped THz pulse transmission and the reference THz pulse in a single scan. To achieve this, the pump pulse is chopped at half of the original repetition rate of the laser source, which is 520 Hz, while the THz pulse is chopped at a frequency of 260 Hz. Lock-in amplifiers are used to measure the pulses as shown in Fig. 4.1. Since the chopping frequency of the THz source beam (260 Hz) is half of the pump pulse (520 Hz), the lock-in amplifier set at 260 Hz sees one THz pulse through a pumped sample and one THz pulse through an unpumped sample. The value it measures is the average electric field of the pumped and reference pulses (E_{avg}). Another channel set at 520 Hz measures the differential transmission of the pumped and reference pulses (ΔE) by monitoring the change of the transmitted field at this frequency. The THz pulses through the pumped sample (E_{pump}) and unpumped sample (E_{ref}) can be reproduced using the following equations

$$E_{\text{ref}} = \frac{2E_{\text{avg}} - \Delta E}{2} \tag{4.1}$$

$$E_{\text{pump}} = \frac{2E_{\text{avg}} + \Delta E}{2} \tag{4.2}$$

After these pulses are reproduced, they can be used to extract the photo-induced conductivity for further analysis.

The waveform is usually measured over several averages to reduce systematic error. The signal to noise ratio achievable with this system can be as high as several hundred with 10 averages taken in the scan.

4.4 Experimental Procedures

To start an ultrafast THz spectroscopy experiment, the Millennia pump laser for the KM Ti:Sapphire laser kit has to be warmed up first. After turning on the Millennia pump laser, it is left for 30 minutes to let the diode currents stabilize. In the meantime, the pump laser of the multipass femtosecond Ti:sapphire amplifier can also be turned on for warm up. When the Millennia pump laser is stabilized, a small shaking of the prism is applied to the KM Ti:Sapphire laser kit to have it mode-locked. The output power is optimized by adjusting the mirrors of the laser kit, and is used as the seed laser beam in the experiment. It is then directed to the input aperture of the amplifier. When the pump laser of the amplifier is ready, the 800 nm seed beam is amplified to around 800 mW at a same repetition rate of 1.04 kHz.

The amplified source laser is directed to the experiment area for spectroscopy. The vacuum chamber where all the experiments are done is shown in Fig. 4.1(b). Samples are placed behind the apertures of the sample holder for TRTS experiments, and the sample holder is installed on a translation stage that allows control of the position of the sample in three directions. The first step of a THz spectroscopy experiment is to find the THz signal through an aperture on the sample holder. We block the THz generating beam temporarily and turn on a diode laser alignment beam that travels the same path as the THz generation beam. Since it also has the same path as the THz pulses, we can find the approximate position of the THz beam at the sample holder with the diode laser spot. By moving the translation stage, we let the diode laser beam pass through the aperture. Then the diode laser is turned off, and the THz generation beam is unblocked.

In the control program, we scan Stage 1 to search for the THz signal. At the correct delay time, we should see a THz waveform in the scan window. It should be noted that some THz components might still be cut by the sample holder aperture, as it was only roughly centered with the diode laser beam. To maximize the THz signal, Stage 1 is moved to the position of the THz peak, then the translation stage is carefully adjusted to get the maximum THz signal by watching the strength of the THz peak. When we get the maximum signal, the THz focal point should be right at the aperture position. We also need to make sure the optical pump beam coincides with the THz beam. The optical pump beam should be centered at the sample position as the THz beam, and should be large enough to cover the whole aperture uniformly. The power of the optical pump pulse should be measured outside the chamber, in front of the aperture, and after the aperture. These powers are used to calculate the fluence of the pump pulse.

After finding the THz signal, the lid of the vacuum chamber is closed and the chamber is pumped to high vacuum (10^{-5} Torr). Before the start of experiments, the detectors should be balanced with the THz beam blocked. THz time-domain spectroscopy is done by scanning Stage 1. To scan the negative differential THz transmission ($-\Delta T/T_0$), Stage 2 is scanned with Stage 1 sitting at the THz pulse peak. To measure the photoexcited waveform, Stage 1 is scanned with Stage 2 sitting at a positive delay time. The translation stage is connected to the cryostat for low temperature experiments. A LakeShore 311 Temperature Controller is used to control the temperature of the sample holder. A thermal diode is connected on the sample holder to monitor the sample temperature. The temperature controller automatically adjusts its cooling power to reach a stable temperature input by users. While in this thesis, temperature dependence study was not involved.

Chapter 5

Time-Resolved THz Spectroscopy of Silicon-on-Sapphire Films

Time-resolved terahertz spectroscopy was performed on 400 nm-thick silicon-on-sapphire thin films. Though silicon has already been widely used in many applications, it is still worth studying its property with sub-picosecond time resolution. The ultrafast THz spectroscopy results of silicon can also be used as a reference for studying other semiconductors that are not as well understood. Also, the properties studied at sub-picosecond resolution will be useful in the development of ultrafast devices based on silicon.

5.1 Introduction to Silicon-on-Sapphire Films

Silicon is one of the most abundant elements on Earth in the form of silicate compounds. High purity silicon is widely used in electronics applications. Since the last century, lots of research has been done on ultrapure silicon to study the atomic structure [75, 76], energy band structure [77, 77], carrier mobility [78,79], and photoexcitation-related events [80,81]. Single crystal silicon forms a diamond cubic structure. It is an indirect band gap semiconductor with a gap energy of 1.12 eV at room temperature. The most common applications include integrated circuits, transistors, solar cells, photodetectors, *etc.* It is commonly regarded as one of the most important elements in the development of modern human society.

The sample used in this project is a 200 nm thick epitaxial silicon thin film on a 0.5 mm thick sapphire substrate. This sample has been used as a reference sample in studying the transient terahertz conductivity of silicon nanocrystal films with ultrafast terahertz spectroscopy in our group [61]. The sapphire substrate has a refractive index of 3.1 in the THz frequency range studied here [82].

5.2 Carrier Decay Dynamics of Silicon-on-Sapphire

When semiconductors are excited by an optical pulses that has photon energy higher than the band gap, free carriers are excited in the material. Though the mechanisms are not the same, photoexcited semiconductors behave quite like doped semiconductors [83]. The photoexcited conductivity and the carrier decay dynamics are very important for developing semiconductor devices. For the epitaxial silicon thin film, the transient conductivity and decay dynamics are both studied by time-resolved THz spectroscopy. The sample was excited with a 400 nm pump pulse at several different fluences. For each fluence, the negative differential transmission, $-\Delta T/T_0$, is plotted against the delay time between the optical pump pulse and the THz pulse peak. The data was scanned over 130 ps, and is plotted in Fig. 5.1. The rise time of each scan after the arrival of optical pump pulse is less than 0.5 ps, and is limited by the experiment setup.

From these $-\Delta T/T_0$ scans, the peak modulation right after the photoexcitation can be extracted, and is related to the incident fluence by Eq. 3.39. By reversing Eq. 3.39, we are able to get the $\left|\frac{\Delta T}{T_0}\right|_{\max}$ as a function of pump fluence F_{pump}:

$$\left|\frac{\Delta T}{T_0}\right|_{\max} = \frac{1}{1 + \frac{(1+N)h\nu_{\text{pump}}}{\eta\mu Z_0 e F_{\text{pump}}}} \tag{5.1}$$

It has been shown that this equation works very well in describing the photoconductivity in TRTS experiments [24], and it also agrees with our results.

Using the relationship between the excitation fluence and the maximum carrier density in Eq. 3.38 and assuming the quantum efficiency to be 1, an estimated lower boundary of carrier mobility is calculated from each $-\Delta T/T_0$ scan. Plugging these values into Eq. 3.37, we are able to obtain the carrier

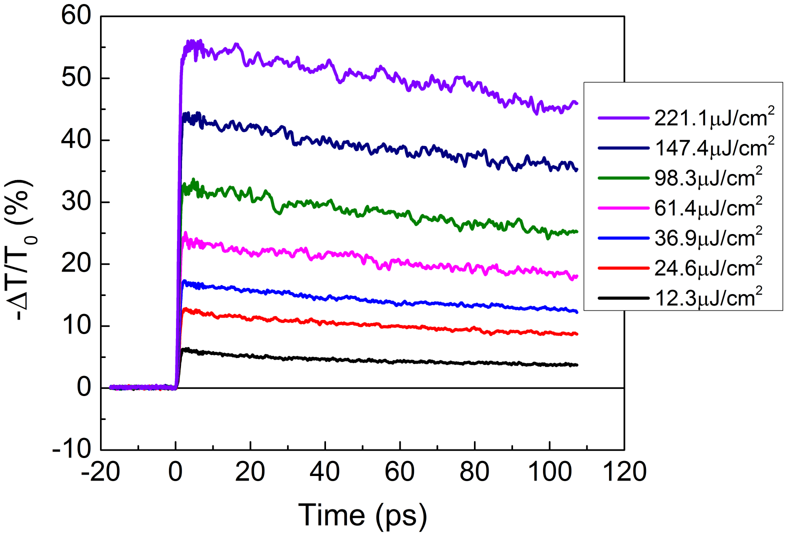

Figure 5.1: Negative differential transmission $-\frac{\Delta T}{T_0}$ as a function of pump-probe delay time of SOS excited by 400 nm pump pulses at various fluences.

density as a function of delay time for each fluence, as shown in Fig. 5.2.

From the semi-log plot in Fig. 5.2, we see that the carrier decay curves follow single exponential decays. Using a single exponential decay function to fit each decay curve, we get the carrier decay time t_1 at various fluences.

The carrier decay time t_1 changes as incident fluence is changed. Decay times at different fluence are plotted in Fig. 5.3. The decay time t_1 increases initially for $F < 120$ μJ/cm^2. The point above 120 μJ/cm^2 doesn't follow the trend. This is probably due to the carrier density being no longer proportional to the $\left|\frac{\Delta T}{T_0}\right|$ at high fluence. The result from time-resolved anti-Stokes Raman scattering done by Jeffrey J. Letcher *et al.* shows that the carrier lifetime increases as the pump fluence increase even at high excitation powers [84], and the TRTS result on radiation-damaged silicon thin films also shows an increasing trend of the carrier lifetime [24]. A more accurate way to study the carrier density is to get the carrier density n at different delay time t from the conductivity data, but it is not feasible to get the conductivity data at all delay time, as limited by the large amount of time need in such an experiment.

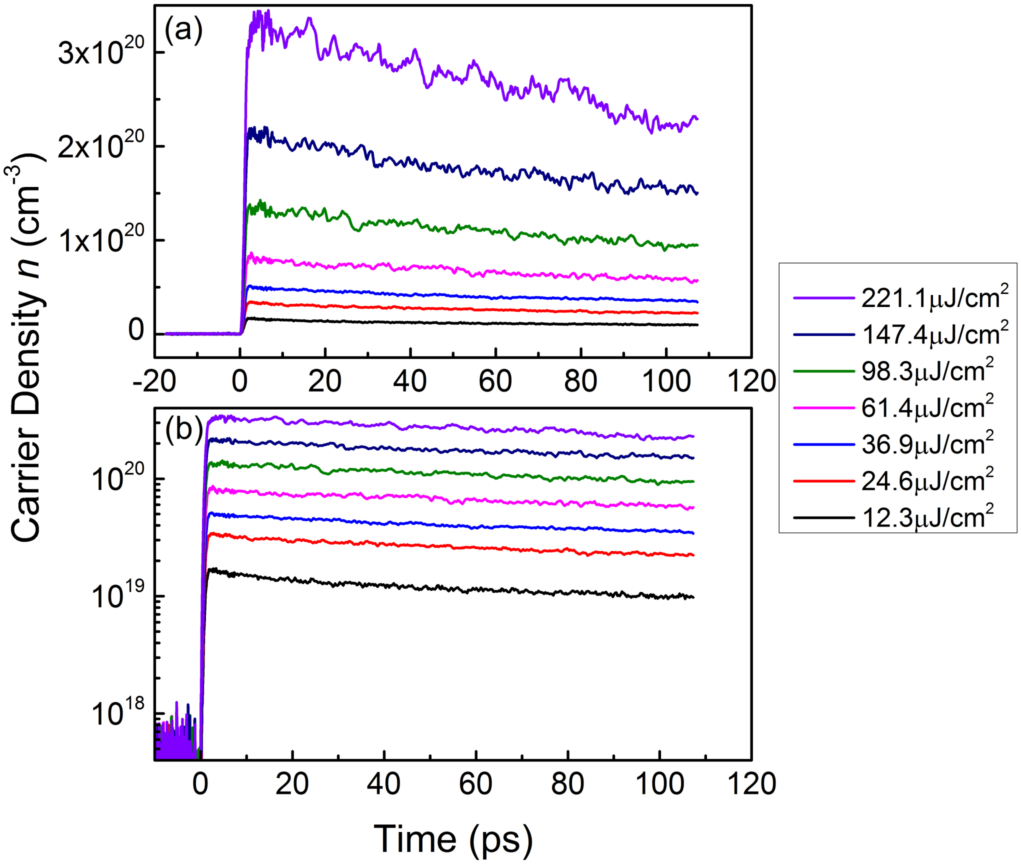

Figure 5.2: (a) Carrier density calculated using Eq. 3.37 as a function of delay time at various fluences. The same data plotted in semi-log scale is shown in (b).

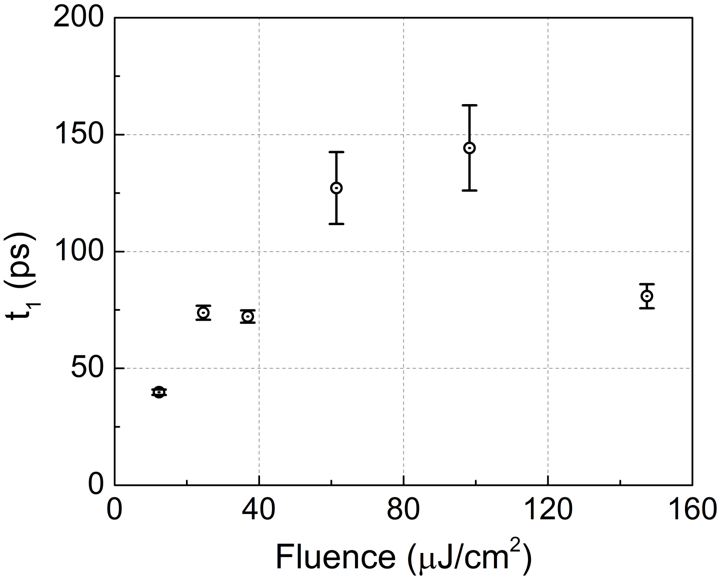

Figure 5.3: Photocarrier decay time t_1 as a function of fluence for SOS. The decay time for $F = 221.1$ μJ/cm^2 is not included. The decay time at high fluence is much longer than the time range of the experiments, which makes it difficult to extract the fitting parameters.

5.3 Transient Conductivity of Silicon-on-Sapphire

The free carriers in the sample lead to a time-dependent photoconductivity after photoexcitation. The transient conductivity data is extracted from the THz pulses transmitted through the optically-pumped sample as introduced in Chapter 3. In this experiment, the complex conductivity induced by photoexcitation was measured at 10 ps after the arrival of 400 nm pump pulses at multiple fluences. The complex conductivity data were then used to extract the optical and electrical properties of the silicon-on-sapphire. For the epitaxial silicon-on-sapphire, the photoexcited conductivity can be fit by the Drude-Smith model, as shown in Fig. 5.4. The plasma frequency ω_p, the Drude scattering time τ, and the Drude-Smith c-parameter were set as the fitting parameters. The low c values at most of the fluences recover the simple Drude model, which is widely admitted for silicon. By fitting the complex conductivity data, experimental values of ω_p, τ, and c were extracted. These parameters then are used to calculate the carrier density n and mobility μ. The fitting

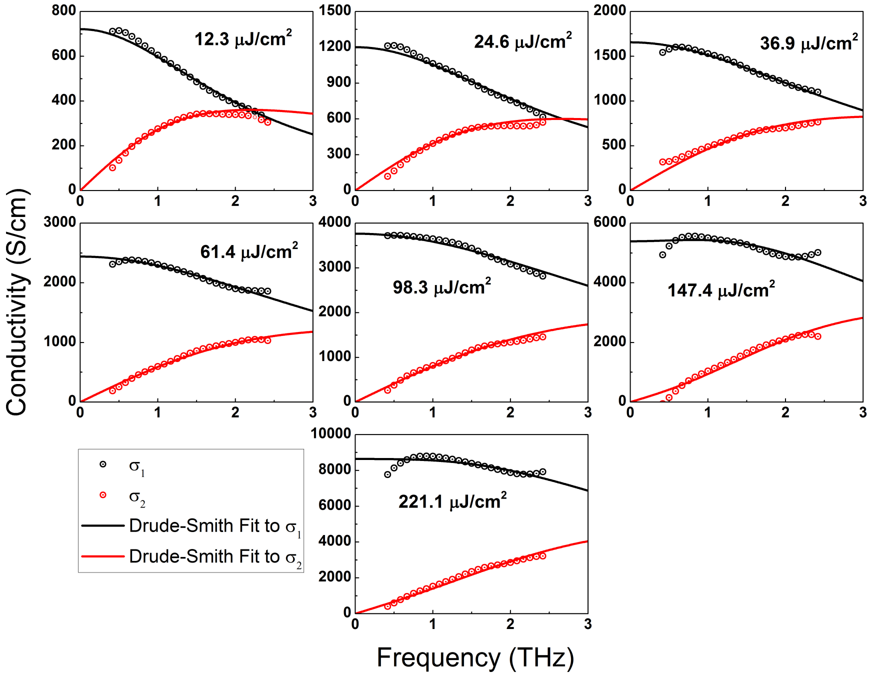

Figure 5.4: Transient conductivity spectra of silicon-on-sapphire measured at 10 ps after photoexcitation by 400 nm pulses. The Drude-Smith model (solid lines) was used to fit to the experimental data (hollow symbols).

Fluence [μJ/cm^2]	ν_p [THz]	τ [fs]	c
12.3	53.3 ± 0.3	72.6 ± 0.9	0 ± 0.009
24.6	75.9 ± 0.5	59.7 ± 0.8	0 ± 0.01
36.9	98.5 ± 0.5	48.9 ± 0.6	0 ± 0.01
61.4	130.5 ± 0.6	41.0 ± 0.4	-0.1 ± 0.1
98.3	174.3 ± 0.9	35.5 ± 0.4	0 ± 0.05
147.4	227 ± 3	31.5 ± 0.8	-0.37 ± 0.02
221.1	301 ± 3	28.1 ± 0.6	-0.32 ± 0.02

Table 5.1: Drude-Smith fitting results of the transient conductivity spectra of silicon-on-sapphire at 10 ps after photoexcitation. The experiment was done at 7 different fluences with 400 nm pump pulses.

results are shown in Table 5.1.

5.3.1 Carrier Density

The carrier density n can be calculated from the plasma frequency ω_p using the equation $n = \frac{\epsilon_0 {\omega_p}^2 m^*}{e^2}$. The carrier density n follows a power law increase as the fluence increases, which is shown in Fig. 5.5 along with the maximum carrier density calculated from the Eq. 3.38. The power of the trend of carrier density n calculated from the plasma frequency is 1.2 rather than linear with fluence. This result gives us the expression of n as a function of F_{pump}

$$n = A(F_{\text{pump}})^{1.2} \tag{5.2}$$

where A is a constant. The reason why it doesn't increase linearly with F_{pump} can be explained by the fluence-dependent exponential decay time. It should be noted that the conductivity spectra were taken at 10 ps after photoexcitation, while the maximum carrier density calculated from the fluence is the value right after the absorption optical pulse. Even at the same positive delay time, the carrier density n may be at a different portion of the original carrier density n_{max}.

Though the carrier density calculated from the plasma frequency obtained from the Drude-Smith fit is very close to the actual carrier density in the sample, we should be careful if we want to use it as a reference of the peak carrier density. For samples with long decay time such as silicon and gallium arsenide, the carrier density doesn't change much within 10 ps after photoexcitation, but

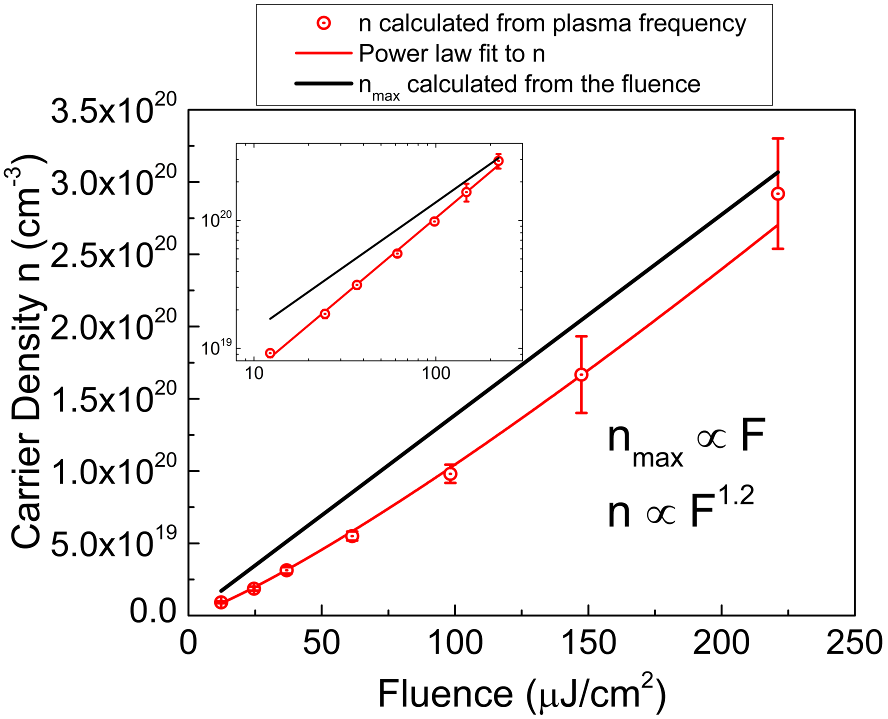

Figure 5.5: Carrier density as a function of pump fluence. The red circles are the carrier density calculated from the plasma frequency obtained from the Drude-Smith fit, which is fit by a power law function as indicated by the red solid line ($n \propto F^{1.2}$). The black triangles are the maximum carrier density calculated from the corresponding fluence using Eq. 3.38. The black solid line is a linear fit to the data.

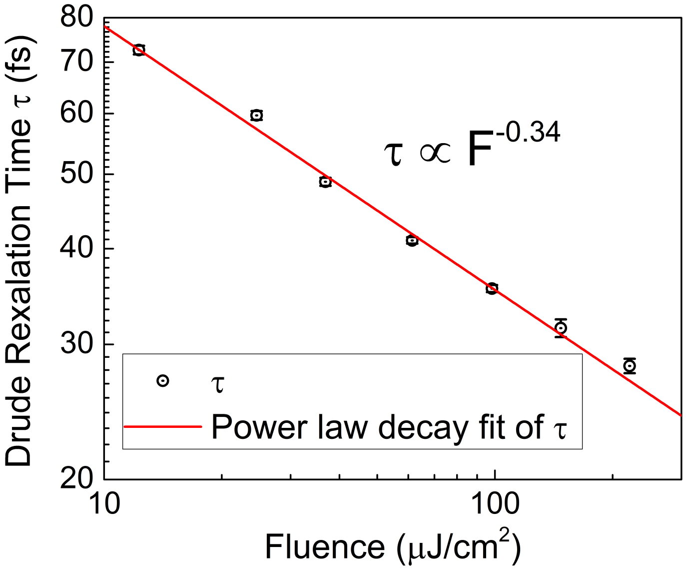

Figure 5.6: Drude scattering time τ extracted by fitting the photoconductivity spectra. The linear fit (solid red line) in log-log scale indicates that the scattering time follows a power law dependence as the fluence increases.

for some nano-crystalline samples with very short decay time, carrier density could change dramatically within several ps.

5.3.2 Drude Scattering Time and Carrier Mobility

In the Drude model, the scattering time τ is the average time that a carrier can travel without collisions. The scattering time τ extracted at different fluences is plotted in Fig. 5.6, and it clearly follows a powerlaw decay as fluence increases.

In developing the Drude model, the assumption of collision is extremely simple, and the nature of the collision process is not specified. In semiconductors, the scattering of carriers [85] is divided into three main categories: impurity (defect) scattering, carrier-phonon and carrier-carrier scattering.

If the scattering is simply caused by defects in crystal structure and surface defects, the scattering rate should not change at different fluences because the number of defect sites doesn't change in the sample. However, defects do contribute to scattering as a background even without excitation. Meanwhile, at high carrier density, the band bending and impurities near the film surface do not change the carrier diffusion. Based on this, we conclude that the change in scattering time is not related to the surface property changes of silicon film.

At room temperature, another important source of scattering is phonons. While a perfect static lattice doesn't interact with carriers, the distorted lattice could cause distortion of the energy band, and thus interfere with the movement of carriers. The distortion can lead to local fields in polar materials such as GaAs. In silicon, phonon-assisted intervalley scattering of free carriers also leads to energy change [81], but has time scales around 100 fs [86] and requires high carrier energies.

The last scattering mechanism is carrier-carrier scattering. Carriers can scatter with each other no matter what the charge is. Carriers can also scatter with plasmons and it is as important as single carrier-carrier scattering [46,87]. At high carrier density, this is the most important scattering mechanism in the sample, where the scattering rate, $\frac{1}{\tau}$, is proportional to $n|\ln(n)|$, which means $\tau \propto \frac{1}{n|\ln(n)|}$. This result doesn't agree with the result we see in the experiments. Others showed that the scattering rate is proportional to $n^{7/6}$ [88], which could cause the powerlaw decay of scattering time τ with other mechanisms.

It has been shown that the Drude scattering time τ in doped Si and GaAs can be described by the empirical Caughey-Thomas equation:

$$\tau = \frac{\tau_{\text{max}} - \tau_{\text{min}}}{1 + (n/n_0)^{\alpha}} + \tau_{\text{min}}, \tag{5.3}$$

where τ_{max}, τ_{min}, n_0 and α are the four fitting parameters in this model [89,90]. This model has limiting values of τ at both the high and low carrier density regions. τ_{max} is the carrier scattering time when the carrier density is extremely low, and τ_{min} is obtained at high carrier density when the sample approaches metallic behavior. This model is used to fit the Drude scattering time τ from the TRTS results as a function of photoexcited carrier density, as shown in Fig. 5.7. The good fit to the data in Fig. 5.7 shows that Eq. 5.3 can describe scattering rates in photoexcited samples as well. The maximum and minimum scattering time, τ_{max} and τ_{min}, in our experiment are 106 ± 16 fs and 25 ± 2 fs, respectively, while the values for doped bulk silicon are 196 fs and 10 fs [89].

Many studies on silicon have shown that the mobility would decrease as the fluence is increased [78,91], as is observed in our experiments. But in radiation-damaged silicon the mobility increases slowly as the fluence increase [24]. Since the carrier mobility is calculated by using equation $\mu = \frac{e\tau}{m^*}$, we know that it is proportional to the Drude scattering time τ. Therefore, the plot of μ against

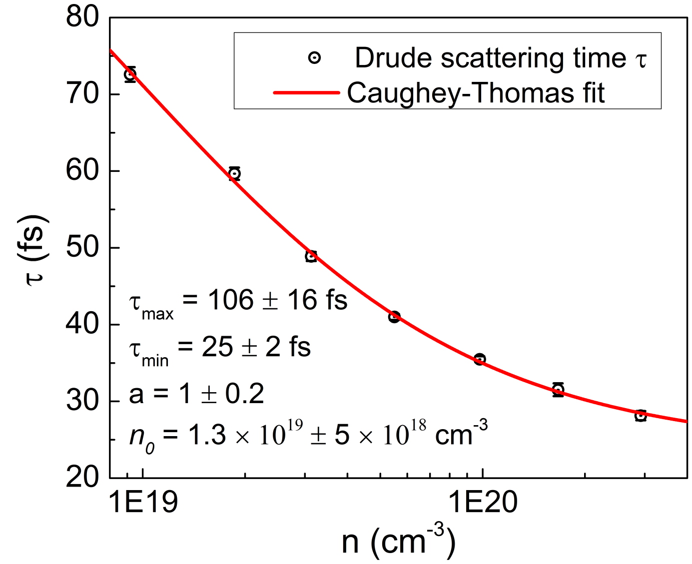

Figure 5.7: Drude scattering time τ of SOS thin film at different photocarrier density. The result is fit by the Caughey-Thomas model (Eq. 5.3).

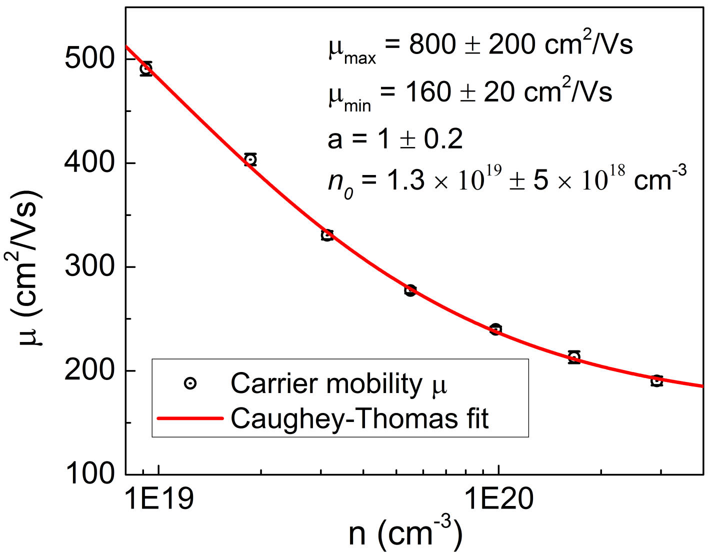

Figure 5.8: Carrier mobility calculated by $\mu = e\tau/m^*$, where the effective mass m^* =0.26 m_0 was used.

incident the carrier density shown in Fig. 5.8 has the same trend as in the plot of τ (Fig. 5.7). The carrier mobility is also fit by the Caughey-Thomas model.

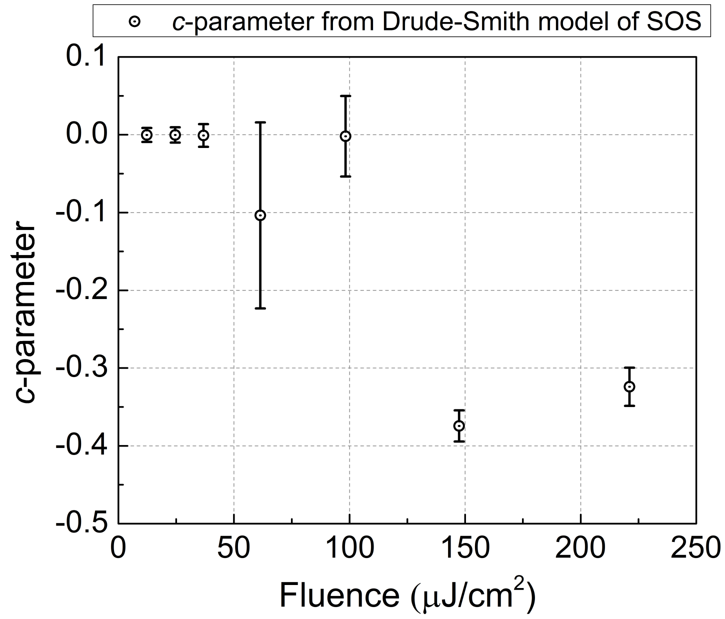

Figure 5.9: Drude-Smith c-parameter of silicon-on-sapphire sample at multiple fluences at 10 ps after photoexcitation by 400 nm pulse.

The decreasing trend in the range of 10^{18} to 10^{20} cm^{-3} has been observed in many other experiments and the mobility value roughly agrees with other studies in this carrier density range [61, 78, 91]. The decrease of mobility at high fluence can be attributed to the electron-hole scattering in silicon [92].

5.3.3 *c*-Parameter in Drude-Smith Model

As discussed in Chapter 3, the Drude-Smith model is a generalization of the Drude model. The c-parameter in the Drude-Smith model varies from 0 to -1, covering states of no carrier localization to high carrier localization. From the c-parameters extracted from the conductivity spectra in Fig. 5.4, we see that the photoconductivity remains simple Drude model at low pump fluence and becomes Drude-Smith model at higher fluence.

Similar study has been done by Cooke *et al.* on silicon-on-sapphire and some silicon nano-crystallite films [61]. The very low $|c|$ value observed on silicon-on-sapphire films at low optical pump fluence indicates there is hardly any carrier localization in the sample. At higher fluences, the real conductivity σ_1 at low frequency seems to be depressed, which is usually a signal of carrier localization in the Drude-Smith model.

It has already been observed by other groups that at very high fluence the transient conductivity of silicon and some other semiconductors follows Drude-Smith [93]. The value of $|c|$ increases as the pump fluence is increased [23]. In this experiment, we didn't observe very strong carrier localization in the studied fluence range. The level of localization should also be dependent on the sample quality. The c-parameter at different fluences is plotted in Fig. 5.9.

The c-parameter at fluences lower than 100 μJ/cm^2 is close to 0, which indicates that there is barely any carrier localization at low fluence. For fluence higher than 100 μJ/cm^2, the c-parameter becomes non-negligible. This means that at high fluence and carrier density, the carriers start to be localized. The localization we see in our experiment is not very strong, but it could be increasing as the fluence is increased more.

One possible reason for the fluence-dependent carrier localization is that the localization is caused by surface defects in the silicon-on-sapphire sample. It has been shown that carrier localization can be caused by the accumulation of carriers around defect sites [62]. High pump fluence creates a high carrier density that leads to the accumulation of photocarriers at the surface defects in the sample, which in turn causes carrier localization. Another possible explanation is that the high population of electron-hole pairs lowers the local band gap energy. Because the pump beam is not perfectly uniform, it generates higher carrier densities in some areas. The lower band gap in these areas may result in carrier localization.

Chapter 6

Time-Resolved THz Spectroscopy of Iron Pyrite Nano-crystalline Films

Iron pyrite (FeS_2), an indirect-gap semiconductor with a band gap around 0.95 eV [94], has been widely studied in the last decade for its promising future applications in optoelectronics [95, 96]. It is abundant and has an absorbance that matches the solar spectrum extremely well, making it especially suitable for photovoltaic devices. In this chapter, I discuss time-resolved THz spectroscopy (TRTS) of the nano-crystalline FeS_2 films.

6.1 Sample Preparation and Characterization

Bulk and nanostructured iron pyrite has recently been the subject of many theoretical and experimental studies [97, 98]. In particular, much work has been done over the past several decades to determine the crystal structure and band gap of this material [99]. The crystalline structure of FeS_2 has been successfully established using X-ray scattering studies [100]. The iron atoms form a face-centered cubic structure, and the sulfur atoms are embedded in this lattice at positions of $\pm(u, u, u; u + \frac{1}{2}, \frac{1}{2} - u, \overline{u}; \overline{u}, u + \frac{1}{2}, \frac{1}{2} - u; \frac{1}{2} - u, \overline{u}, u + \frac{1}{2})$, where $u = 0.386$ [101–103]. The reported values for the energy band gap range from 0.72 eV to 1.2 eV at room temperature [104], but the most widely accepted value is around 0.92–0.95 eV [105]. At low temperatures, the band gap slowly decreases [106]. While most of the studies to date were carried out on single crystal samples, understanding the properties of FeS_2 thin films becomes more urgent as new applications of thin film FeS_2 are being proposed. In particular, various techniques have been developed for fabrication of thin film and nanostructured FeS_2 for photovoltaic applications [74, 98, 107–112].

The FeS_2 nano-crystalline thin films studied in this chapter were prepared by LaForge *et al.* [112] by sulfurization of precursor Fe films deposited by glancing angle deposition (GLAD). It is known that the structure of the precursor Fe film influences the microstructure of the FeS_2 films, and it is important to understand this relationship.

The precursor Fe films having columnar structure are prepared using GLAD on quartz substrates that have a refractive index of 2.15 in the THz frequency range [82]. Changing the deposition angle α (measured from the surface normal of the sample) controls the void fraction of the Fe film, with the smaller deposition angles resulting in Fe precursor film with lower void fraction. After the precursor films are prepared, they are sulfurized with sulfur powder in a sealed environment at 450 °C. While the sulfurization process also influences the microstructure of the resulting FeS_2 film, in this project we have focused on establishing the link between the morphology of the precursor Fe film and the structure of the FeS_2 film to the resulting optoelectronic properties [110].

Only films deposited with $\alpha > 80^\circ$ show structural integrity, while those deposited at smaller angles exhibit structural failure defects such as cracking and buckling due to surface strain during sulfurization. Films prepared for this study have thickness in the range of 300 nm to 360 nm, which is sufficient to absorb all incident light energy in the visible range, as the optical penetration depth of visible light in FeS_2 is tens of nanometers [105].

Steady-state, room temperature resistivity of FeS_2 films varies from 0.1 to 10 $\Omega\cdot$cm [106, 107], and the resistivity of nano-crystalline films has also been found to be dependent on the film thickness [113]. The resistivity of single crystal samples is generally lower [114], and also depends on the sample quality. While the nature of the majority carriers in undoped FeS_2 is yet to be conclusively established, some reports indicate that the electrons dominate in FeS_2 at room temperature [106]. For single crystals, the mobility is around 30–100 cm^2/Vs at room temperature, while the mobility of thin films is usually in the 0.1–1 cm^2/Vs range.

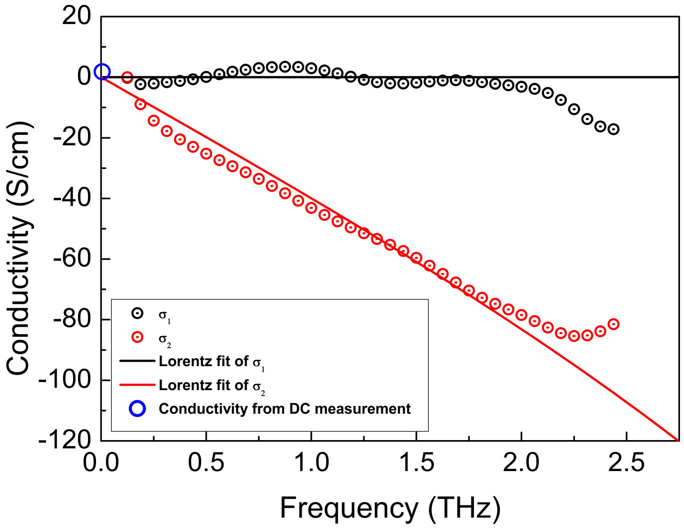

Figure 6.1: Frequency-dependent complex conductivity of the FeS_2 sample grown at $\alpha = 82°$. The black and red solid lines are the results of the simultaneous fits of the real and imaginary conductivity to a Lorentz oscillator model with central frequency of 8.79 THz, lifetime of 2.7 ps and plasma frequency of 74 THz. The blue circle shows the DC conductivity [112].

6.2 THz Time-Domain Spectroscopy of FeS_2

Before exploring the nature of photoinduced conductivity of FeS_2 nano-crystalline films, it is important to understand their dark conductivity (conductivity without photoexcitation).

We used THz time-domain spectroscopy (THz-TDS) to study frequency-resolved dark conductivity of FeS_2 film grown at $\alpha = 82°$. In the literature, reported values of the DC conductivity of FeS_2 thin films are quite low at around 0.1 to 10 S/cm [110, 113], and the conductivity of single crystal samples is around 20 to 100 S/cm [94, 104, 104]. Also, far infrared spectroscopy experiments have shown that the AC conductivity of FeS_2 films follows a multi-Lorentz oscillator response [115, 116]. In the THz-TDS experiment, the phase and the amplitude of the terahertz pulse transmitted through the FeS_2 thin film on the quartz substrate is compared to those of the THz pulse transmitted through the substrate only. Since the thickness of the FeS_2 nano-crystalline film is much smaller compared to the THz wavelength, we use Eq. 3.32 and Eq. 3.33 to extract the real and imaginary conductivity in the THz range.

The conductivity data in the THz range can be successfully fitted to a

Lorentz oscillator [Eq. 3.15 and Eq. 3.16]. However, since the observed σ_1 is nearly flat and σ_2 linearly decreases in the studied frequency range (<3 THz), determining the central frequency of the oscillator is difficult as it falls outside the experimental range. To obtain the fits shown in Fig. 6.1, we used the literature value of 8.79 THz for the lower energy oscillator frequency and $\tau = 2.7$ ps for oscillator lifetime [115–117], which is related to the stretching vibrations of the bonds between S atoms [118,119]. This allowed us to extract the value of plasma frequency $\nu_p = 74$ THz.

In the Lorentz model, the DC conductivity is 0, and the material is insulating at zero frequency. Since the measured DC conductivity using four-point probe of this FeS_2 film is close to 0.2 S/cm, this might suggests the existence of a small but non-zero Drude contribution to conductivity in addition to the dominant contribution from a Lorentz oscillator. As can be seen from the graph, the four-point probe DC conductivity is practically indistinguishable from the value we obtain by extrapolating the fit to the real conductivity to $f = 0$ THz. When taking the experimental errors into account, the Lorentz oscillator model agrees with the experimental values nicely.

6.3 Surface Morphology of Nanocrystalline FeS_2 Films

The microstructure of FeS_2 films prepared from Fe precursor films is known to dependent on deposition angle α. In turn, the film morphology determines its electrical and optical properties, and thus determines its suitability for applications in semiconductor electronics. In our experiment, films deposited at 80°, 82°, 84° and 88° were studied (for brevity, $\alpha80$ stands for the sample deposited at 80°, and so on). The morphology of these films can be seen in the scanning electron microscopy (SEM) images (Fig. 6.2). For the $\alpha80$, $\alpha82$ and $\alpha84$ samples, the films contain nano-crystals with sizes ranging from tens to hundreads of nanometers. From the edge-view micrographs, we can see that these films are quite uniform, with low void fraction as the space between the large grains is filled by the small ones. Compared to these films, the $\alpha88$ one is quite different. It contains no nano-grains larger than 100 nm, and the small nano-grains form 200 nm–300 nm clusters. Both plan-view and edge-view micrographs show the presence of voids between the nano-clusters. It is

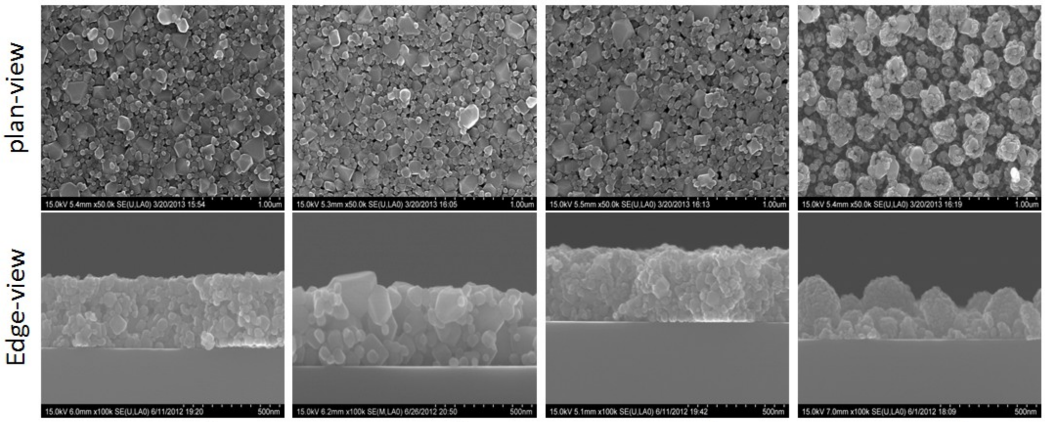

(a) α=80° (b) α=82° (c) α=84° (d) α=88°

Figure 6.2: SEM results of FeS_2 nano-crystalline films deposited at (a) 80° (b) 82° (c) 84° (d) 88°. The upper picture shows the plan-view of each film while the lower picture shows the edge-view. Images were taken by Joshua LaForge.

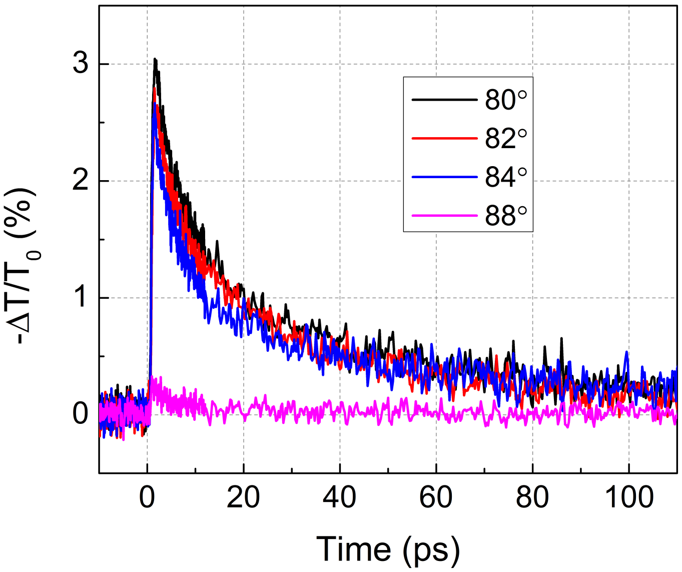

Figure 6.3: $-\frac{\Delta T}{T_0}$ of FeS_2 nano-crystalline films pumped with 400 nm pulses. Fluence was kept at $F_{pump} = 288\ \mu J/cm^2$ for all four samples.

also evident from the edge-view that the surface of the $\alpha 88$ film is not smooth. Overall, the grain size is much smaller in GLAD-grown films than samples prepared by other methods [108].

6.3.1 Optical Pump-THz Probe of FeS_2 Films with Different Surface Morphology

The frequency-resolved photoconductivity of these four samples was studied using optical pump-THz probe spectroscopy. Fig. 6.3 shows comparison of the photoconductivity dynamics of the four films measured using the same excitation fluence $F_{pump} = 288\ \mu\text{J/cm}^2$.

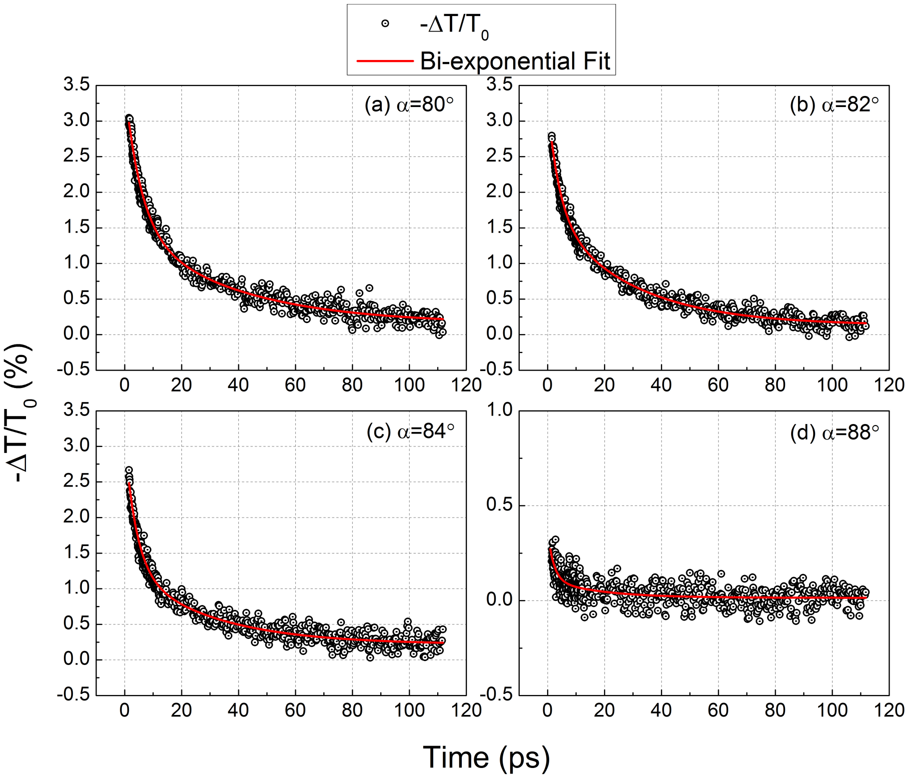

Figure 6.4: Photoconductivity decay of FeS_2 nano-crystalline films grown at deposition angles of (a) 80° (b) 82° (c) 84° (d) 88°. Red solid lines are fits of data to biexponential decay functions. (Decay times of fits shown in Fig. 6.5)

The magnitude of the photoinduced conductivity is highest in the $\alpha 80$ sample, while $\alpha 82$ and $\alpha 84$ exhibit slightly lower signal. Different from these three samples, the $\alpha 88$ film has very weak photoresponse at this fluence. In all four films, the photoconductivity dynamics fit well to a biexponential decay (Fig. 6.4). Since for $|\Delta T/T_0| < 20\%$, $|\Delta T/T_0|$ is roughly proportional to the photoinduced carrier density, the observed biexponential decay suggests the presence of two mechanisms for trapping of the photoexcited carriers in these nano-crystalline films. The fast decay component has decay time $t_1 < 10$ ps,

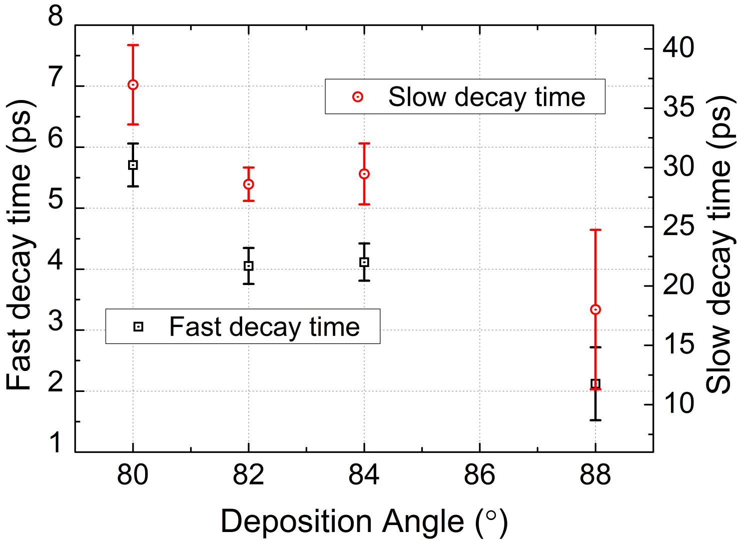

Figure 6.5: Fast and slow decay time constants of FeS_2 nanocrystalline films.

and the longer component t_2 is in the tens of picoseconds range for all films (Fig. 6.5). Both decay constants have the highest values in the $\alpha 80$ sample and the lowest values in the $\alpha 88$ sample, with the decay times for $\alpha 82$ and $\alpha 84$ samples falling between the $\alpha 80$ and $\alpha 88$ values.

6.3.2 Transient Conductivity of FeS_2 Films with Different Morphology

For the $\alpha 80$, $\alpha 82$ and $\alpha 84$ samples, the frequency-resolved photoinduced conductivity spectra were measured at 5 ps and 10 ps after photoexcitation, and fitted by a Drude-Smith conductivity model [Eq. 3.18 and Eq. 3.19], which takes carrier localization effects into account. All the spectra and the corresponding fits are plotted in Fig. 6.6.

For all the samples, the conductivity data shows evidence for strong localization of photoinduced carriers. The real component of the conductivity is strongly suppressed at low frequencies, and the imaginary component of the conductivity is negative over the entire studies frequency range. The Drude-Smith fitting parameters are shown in Table 6.1.

Of all the films, $\alpha 80$ has the highest plasma frequency, indicating that the photoexcited carrier density is highest in this sample. While values of the Drude relaxation time τ are close for these samples, τ at 10 ps after pho-

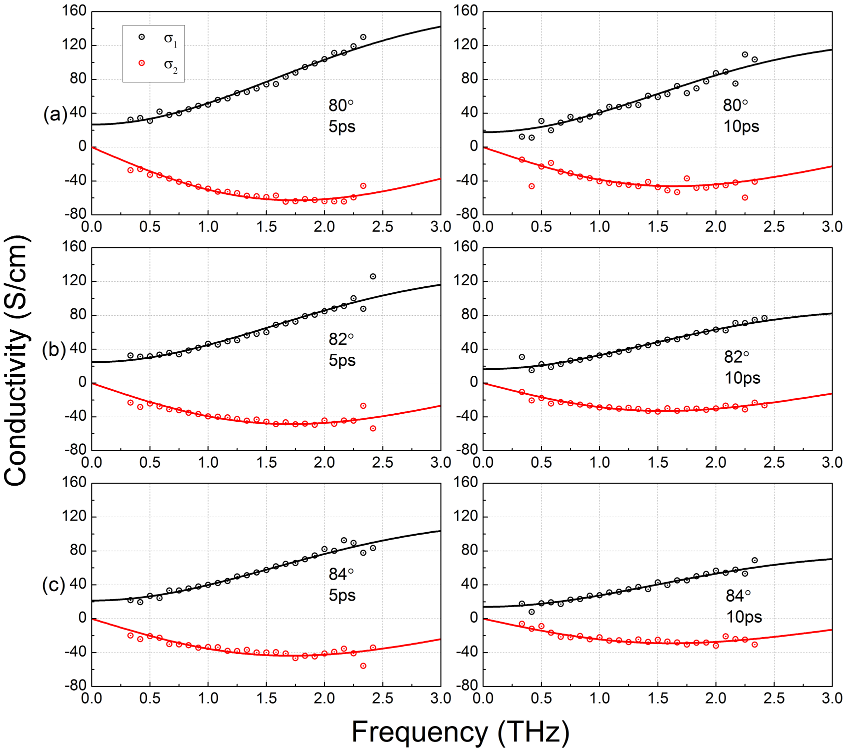

Figure 6.6: Photoinduced conductivity of the (a) α80 (b) α82 (c) α84 samples at 5 ps and 10 ps after photoexcitation. The black and red solid lines are the simultaneous fits of real and imaginary conductivity components to the Drude-Smith model (Eq. 3.18 and Eq. 3.19).

$\alpha[°]$	Delay Time [ps]	ν_p [THz]	τ [fs]	c
80	5	50.0 ± 0.8	36.0 ± 0.7	-0.915 ± 0.003
80	10	42 ± 2	39 ± 2	-0.928 ± 0.009
82	5	45 ± 1	36 ± 1	-0.902 ± 0.006
82	10	35.0 ± 0.7	40 ± 1	-0.903 ± 0.005
84	5	42 ± 1	36 ± 1	-0.904 ± 0.006
84	10	33.2 ± 0.9	39 ± 1	-0.905 ± 0.006

Table 6.1: Drude-Smith fit parameters for FeS_2 nano-crystalline films at 5 ps and 10 ps after excitation.

toexcitation is slightly higher than the value at 5 ps, suggesting a relationship between the scattering rate and the carrier density. All three films have $|c|$ values that are higher than 0.9, indicating very strong carrier localization. The degree of carrier localization, and consequently the c-parameter, is determined by the size of nano-grains, carrier mean free path, and the height of the potential barrier at the nanograin boundary [61–64, 66, 67]. As the c-parameter is nearly the same in all three films, the photoexcited carriers are mostly localized inside the nanograins, and the film macroscopic morphology beyond the individual nanograins doesn't have a significant impact on carrier dynamics.

6.4 Pump Fluence Dependence of Photoinduced Conductivity

For successful application of the nano-crystalline FeS_2 films in photovoltaic and other optoelectronic devices, it is crucial to understand how changes in the excitation fluence affect their photoconductive properties. As the α80 sample exhibits the strongest photoconductive response of all the films studied, we chose it to study the influence of excitation fluence on photoconductive dynamics and spectra. For these measurements, we have used 800 nm laser pulses for excitation, since the 800 nm beam has more power and allows for the largest variations in incident fluence.

6.4.1 Fluence-Dependent Optical Pump-THz Probe of FeS_2

For the measurements discussed here, 800 nm pump fluence was varied from 73.6 μJ/cm^2 to 2758.4 μJ/cm^2. All measurements were performed at room

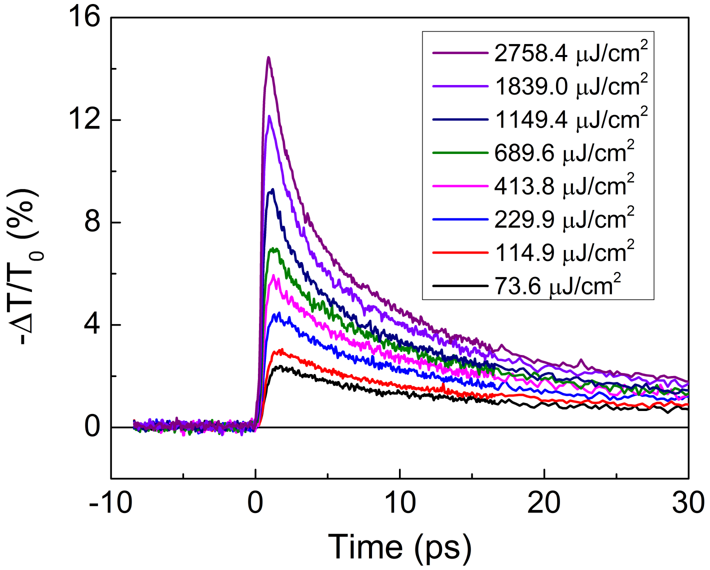

Figure 6.7: Photoinduced conductivity decays of the $\alpha 80$ sample excited with various fluences of 800 nm pump pulses. While the decays were acquired up to 120 ps pump-probe decay time, the plot only shows the data up to 30 ps for clarity.

temperature in the TRTS vacuum chamber pumped to 10^{-5} Torr. The resulting photoconductivity decays are shown in Fig. 6.7. Even at the highest pump fluence, the modulation in the THz transmission is below 20%, allowing us to use the small modulation approximation given by Eq. 3.36. In this approximation, the photoexcited carrier density is proportional to the peak modulation. The peak $-\Delta T/T_0$ as a function of excitation fluence is plotted in Fig. 6.8. As we can see from Fig. 6.8, $|\Delta T/T_0|$ is proportional to the square root of the pump fluence, as opposed to the linear dependence on fluence predicted by Eq. 3.38.

The origin of the square root dependence of the peak photoconductivity on the excitation fluence is not clear at the moment and needs to be further investigated. As the photoconductivity depends on both the scattering rate and the carrier density in the sample, the influence of the pump fluence of both of these parameters needs to be considered. As we have observed in both the silicon and the FeS_2 samples (shown later), while the scattering time and carrier mobility decrease at higher excitation fluences, the carrier density increases leading to overall conductivity increase. The observed square-root fluence dependence of the peak photoconductivity might also be related to

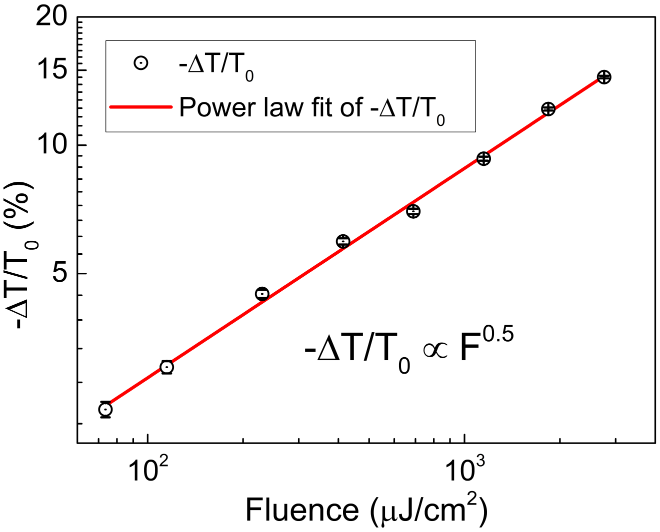

Figure 6.8: The peak modulation of THz transmission of the α 80 film as a function of the pump fluence on a log-log scale. Fitting parameters are indicated in the inset.

a fluence-dependent quantum efficiency, which would lead to the product $\eta\mu$ being fluence-dependent, and causing deviations from a linear dependence of $-\Delta T/T_0$ on fluence. Another possible explanation is that the photocarrier decreases dramatically within one picosecond by bimolecular recombination [120]. As limited by the resolution of our setup, we are not able to observe carrier dynamics within such a short time.

All the decay curves were fit to a biexponential function. The pump fluence dependence of the fast and slow decay time constants is plotted in Fig. 6.9. Both decay times initially increase with the increasing fluence, followed by a decrease at fluences above 250 μJ/cm^2, and eventually saturate at fluences higher than 2 mJ/cm^2.

6.4.2 Fluence-Dependent Transient Conductivity

The complex frequency-dependent conductivity induced by 800 nm pump pulses in the FeS$_2$ α80 film was extracted at multiple fluences at 5 ps and 10 ps after photoexcitation and fit to the Drude-Smith model [Eq. 3.18 and Eq. 3.19]. The fitting parameters are listed in Table 6.2.

From the plasma frequency $\omega_p = 2\pi\nu_p$, we are able to calculate the carrier density in the sample at both 5 ps and 10 ps at different fluences. The resulting

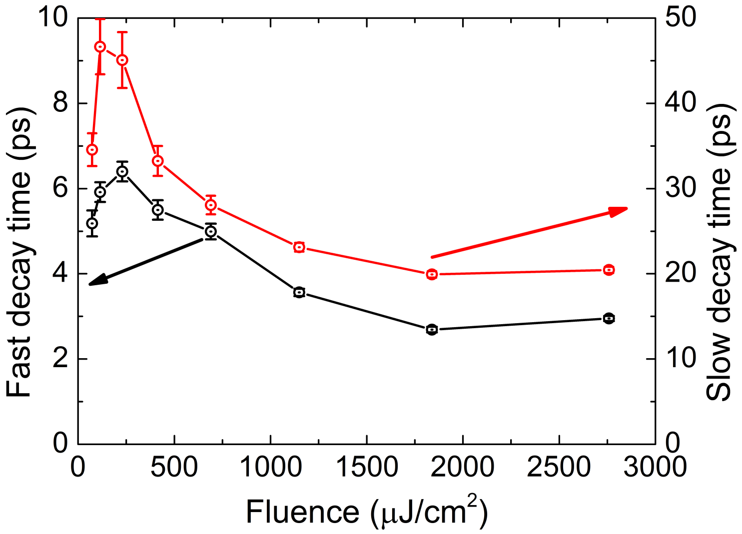

Figure 6.9: The fluence-dependence of the fast and slow decay components of the $\alpha 80$ sample.

Time [ps]	Fluence [μJ/cm^2]	ν_p [THz]	τ [fs]	c
5	73.6	26.8 ± 0.5	53 ± 1	-0.929 ± 0.009
5	114.9	36 ± 1	44 ± 2	-0.91 ± 0.01
5	229.9	49 ± 1	39 ± 1	-0.926 ± 0.007
5	413.8	62 ± 2	34 ± 1	-0.930 ± 0.006
5	689.6	73 ± 2	31 ± 1	-0.924 ± 0.004
5	1149.4	78 ± 2	30.7 ± 0.9	-0.920 ± 0.004
5	1839	87 ± 2	30 ± 1	-0.914 ± 0.004
5	2758.4	84 ± 2	31.5 ± 0.9	-0.903 ± 0.003
10	73.6	24.0 ± 0.8	51 ± 2	-0.91 ± 0.01
10	114.9	28 ± 1	49 ± 2	-0.93 ± 0.01
10	229.9	44 ± 2	36 ± 2	-0.936 ± 0.007
10	413.8	47 ± 2	38 ± 2	-0.946 ± 0.009
10	689.6	61 ± 2	31 ± 1	-0.932 ± 0.006
10	1149.4	65 ± 2	31 ± 1	-0.933 ± 0.006
10	1839	64 ± 2	34 ± 1	-0.937 ± 0.006
10	2758.4	73 ± 3	30 ± 1	-0.917 ± 0.005

Table 6.2: Drude-Smith fitting parameters of the conductivity data of the FeS$_2$ $\alpha 80$ nano-crystalline film at 5 ps and 10 ps after excitation. The experiment was done at 8 different fluences with 800 nm pump pulses.

values are plotted in Fig. 6.10.

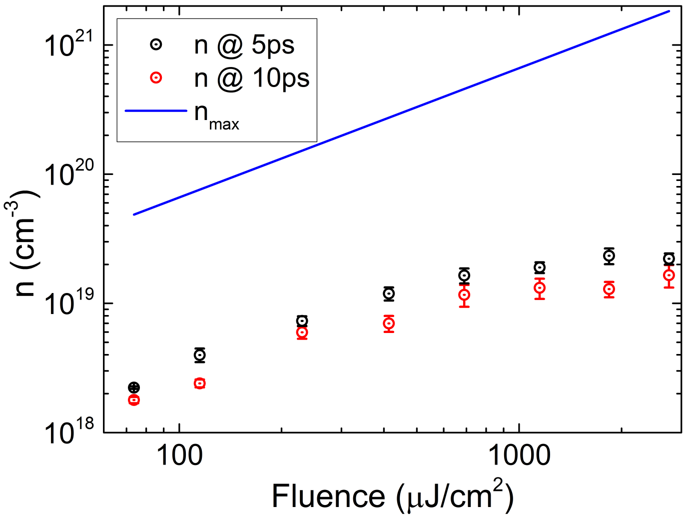

Figure 6.10: The carrier density n of the FeS $_2$ α80 sample at 5 ps and 10 ps after photoexcitation at multiple fluences. The blue solid line shows the square root dependence of pump fluence as observed from the peak modulation.

Fig. 6.10 shows that as time after the excitation increases, the extracted instantaneous carrier density deviates more from the square root fluence dependence that was observed for the peak photoconductivity. This is again due to the different carrier lifetime at different fluences. This also suggests that photoexcited carrier lifetimes are fluence-dependent, and therefore depend on the initial photoexcited carrier density. At high initial carrier densities, carrier lifetimes tend to be shorter, thus suggesting that carrier-carrier scattering plays an important role in carrier recombination and trapping.

We have also studied how the excitation fluence affects the Drude scattering time. As we observed in silicon-on-sapphire, the scattering time can be fit by the Caughey-Thomas model. The FeS_2 α80 sample exhibits similar behavior, with the relaxation time dropping from more than 50 fs at low excitation fluence to around 30 fs at higher fluence, and finally saturating as fluences higher than 500 μJ/cm^2. The relaxation times at 5 ps and 10 ps are plotted in the same graph as a function of fluence, and are fit by the Caughey-Thomas equation (Eq. 5.3) in Fig. 6.11.

Though the scattering time in both the SOS and the FeS_2 are well described by the Caughey-Thomas equation, we have not yet established the exact nature

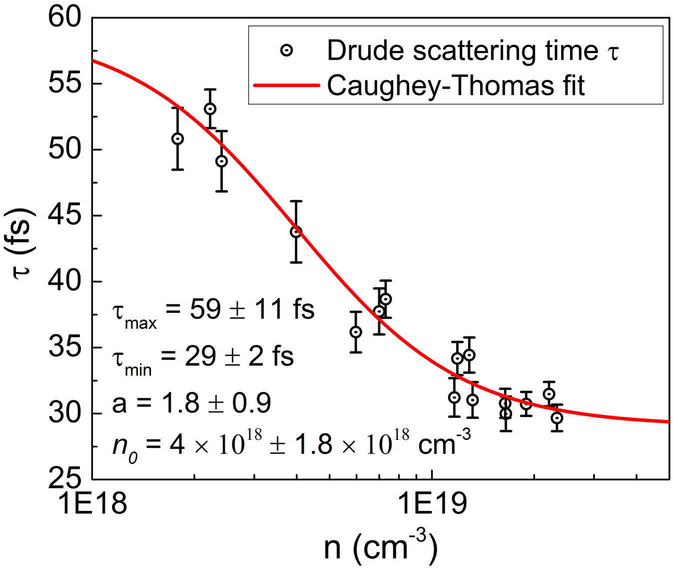

Figure 6.11: The Drude-Smith relaxation time τ of the FeS_2 $\alpha 80$ sample at 5 ps and 10 ps after photoexcitation extracted from the Drude-Smith fit of the conductivity data. The red solid line is a Caughey-Thomas fit of the data.

for the sublinear dependence of carrier density on excitation fluence.

We have also explored how the degree of carrier localization in the film is influenced by excitation fluence. As discussed earlier, the magnitude of the Drude-Smith c-parameter in all the FeS_2 nano-crystalline films is larger than 0.9, indicating significant carrier localization and suppressed long-range conductivity.

To study the origin of the strong localization, the carrier mean free path in the sample was calculated and compared to the grain size. The thermal velocity of electrons in the film is given by

$$v_{\mathrm{th}} = \sqrt{\frac{3k_BT}{m^*}} \tag{6.1}$$

where k_B is the Boltzmann constant, T is the temperature, and m^* is the effective mass. Here, $m^* = 0.25m_0$ and the thermal velocity is $v_{\mathrm{th}} = 2.31 \times 10^5$m/s at room temperature ($T = 295$ K). With an average scattering time of 40 fs, the mean free path is calculated to be 9.2 nm. This distance is shorter than the diameter of the small nanograins in the sample. Strong localization only occurs when the mean free path is comparable to the grain size [62, 67].

Therefore, it indicates that there may be finer structure within the nanograins that may be causing localization over length scales comparable to the carrier mean free path.

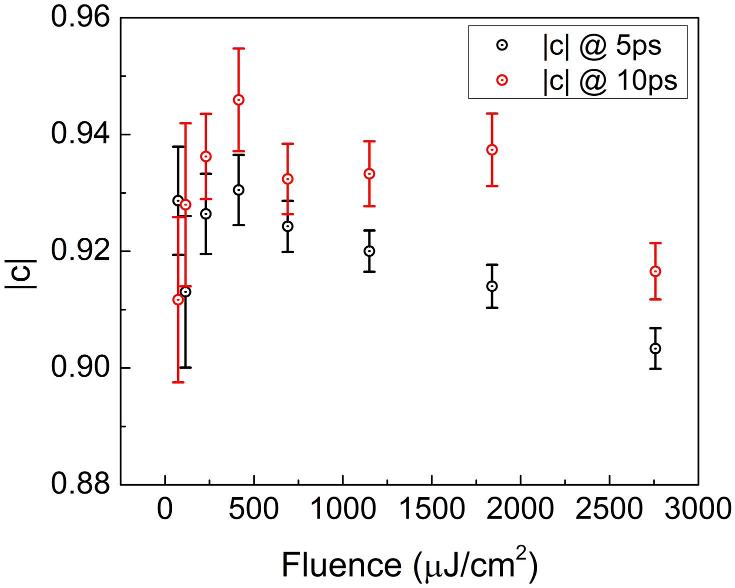

Figure 6.12: The absolute value of the c-parameter of the FeS_2 α80 sample at multiple fluences at both 5 ps and 10 ps after photoexcitation.

The absolute value of the c-parameter in the FeS_2 α80 film at 5 ps and 10 ps after photoexcitation is plotted in Fig. 6.12. As can be seen from the graph, $|c|$ is decreasing slightly as the fluence increases, suggesting that longer range carrier transport is easier when the initial carrier density is higher [62]. The exact reason for this is not yet known but such dependence of carrier localization on initial carrier density might suggest that filling of the interface trap states [62], which occurs faster under higher excitation conditions, lowers the interface barrier height.

In the Drude-Smith model, the carrier mobility is given by $\mu = (1 + c)\frac{e\tau}{m^*}$, and depends on both the carrier localization and scattering time. The carrier mobility calculated using this equation and Drude-Smith fitting parameters at 5 ps and 10 ps is shown in Fig. 6.13. The mobility initially decreases rapidly in the low fluence region. However, at higher fluences the mobility increases slowly in the range from 500 μJ/cm^2 to 3000 μJ/cm^2. The slow increase in mobility is likely due to the slight decrease in the degree of the

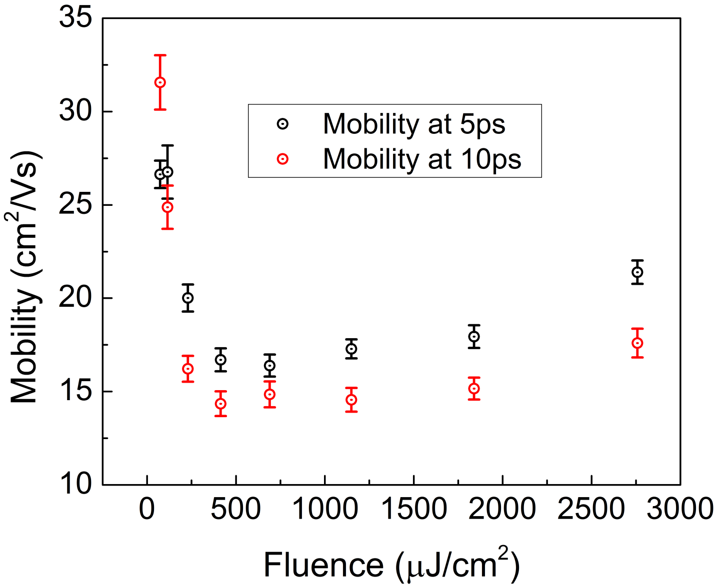

Figure 6.13: The mobility of the FeS_2 α80 film at 5 ps and 10 ps after photoexcitation as a function of the excitation fluence.

carrier localization as shown in Fig. 6.12. The magnitude of the mobility is around 20 cm^2/Vs, close to the mobility in FeS_2 single crystals that range from 30 to 100 cm^2/Vs [94]. It is also 20 times less than that in silicon-on-sapphire, but significantly higher compared to the mobilities reported in organic semiconductors that are usually below 1 cm^2/Vs [12, 25], suggesting that FeS_2 is indeed a candidate material for applications in photovoltaics.

6.5 Frequency-resolved THz Spectroscopy of Nano-crystalline FeS_2 Films as Function of Time after Photoexcitation

Understanding how the photoconductivity changes as a function of time after the optical injection of carriers is important for developing applications that are based on nanocrystalline FeS2 films. For this purpose, we have measured the frequency-resolved photoinduced conductivity spectra of FeS_2 α80 sample at several different times after photoexcitation, as indicated by the arrows in Fig. 6.14.

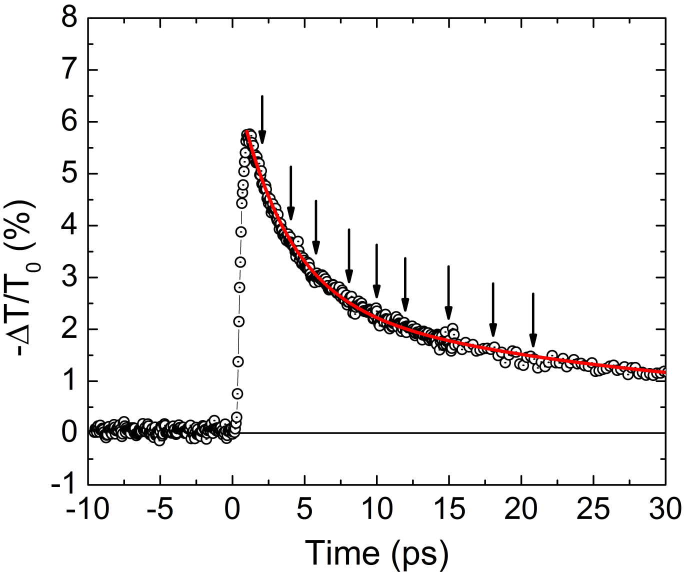

Figure 6.14: Photoconductive decay of the FeS_2 α80 sample excited with 800 nm pulses at 288.3 μJ/cm^2. The arrows indicate time points at which conductivity spectra were acquired.

Delay Time [ps]	ν_p [THz]	τ [fs]	c
2	66 ± 1	35.8 ± 0.8	-0.906 ± 0.004
4	64 ± 1	34.1 ± 0.7	-0.926 ± 0.003
6	57.8 ± 0.8	35.1 ± 0.6	-0.933 ± 0.003
8	52 ± 1	37 ± 1	-0.938 ± 0.005
10	51 ± 1	35 ± 1	-0.934 ± 0.005
12	46 ± 1	38 ± 1	-0.941 ± 0.008
15	46 ± 1	34 ± 1	-0.934 ± 0.005
18	41 ± 1	37 ± 1	-0.931 ± 0.007
21	37.8 ± 0.7	37.0 ± 0.8	-0.926 ± 0.004

Table 6.3: Drude-Smith fitting parameters of the conductivity data of the FeS_2 α80 nano-crystalline film at multiple delay times after photoexcitation.

6.5.1 Time-Dependent Transient Conductivity and Carrier Density

The conductivity spectra taken at different times after photoexcitation with $F_{\mathrm{pump}} = 288.3$ μJ/cm^2 are shown in shown in Fig. 6.15. From the Drude-Smith fitting parameters the time dependent scattering time, Drude-Smith c-parameter, carrier density, and mobility can be extracted.

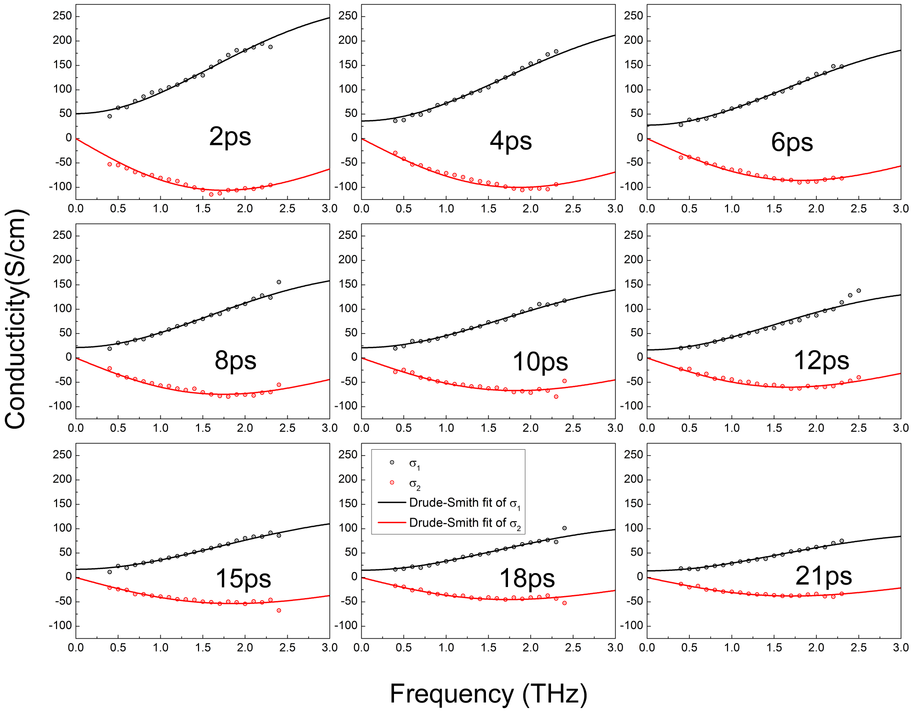

Figure 6.15: The photoinduced complex conductivity spectra of FeS_2 ($\alpha80$) taken at different times after excitation with 800 nm pulses with $F_{\text{pump}} = 288.3\ \mu\text{J/cm}^2$.

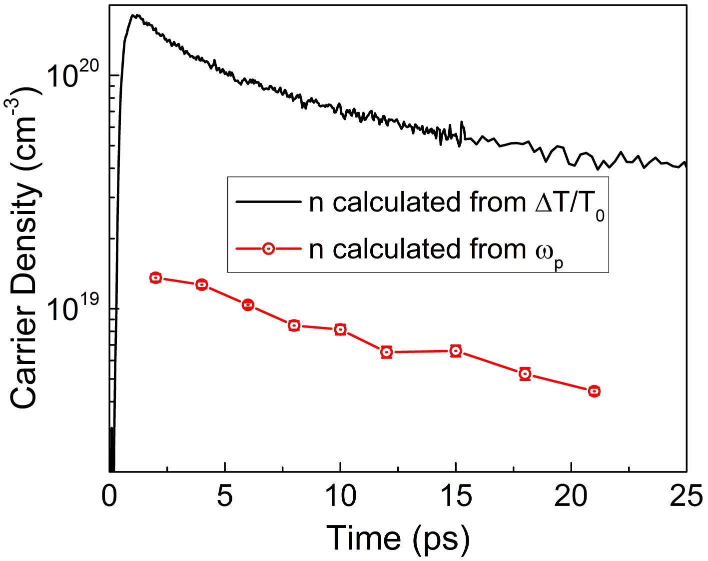

Figure 6.16: Carrier density calculated from $-\Delta T/T_0$ using Eq. 3.37 (solid black curve) and from the plasma frequency as determined by the fit of conductivity spectra to the Drude-Smith model (hollow red circles). With a 800 nm pump at a fluence of $288.3\mu\mathrm{J/cm}^2$, the peak carrier density is 1.93×10^{19} cm^{-3}

As discussed earlier, the carrier density calculation using the photoconductive decay is only applicable in predominating resistive samples and can provide incorrect results in films with an appreciable imaginary conductivity component. In this section, we compare the carrier density calculated using equation Eq. 3.37 to the value obtained from the plasma frequency. When calculating carrier density changes as a function of time after excitation using Eq. 3.37, we have to assume that the mobility is time-independent. The calculated carrier density is compared to the carrier density that is calculated from the plasma frequency of the Drude-Smith fit, as shown in Fig. 6.16. Comparing these two carrier density values, we get a quantum efficiency for the FeS_2 nano-crystalline film at a fluence of 288.3 μJ/cm^2 of around 10%.

6.5.2 Dependence of Drude Relaxation Time and Mobility on Pump-Probe Delay

The relaxation time τ was extracted from the Drude-Smith fits to the frequency-dependent conductivity spectra at different delay times after the

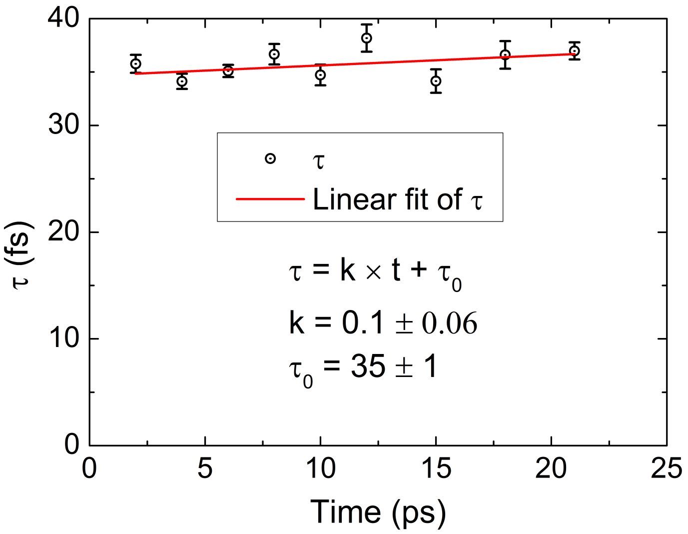

Figure 6.17: The Drude relaxation time τ extracted from the Drude-Smith fits to the conductivity spectra at different delay times after photoexcitation.

photoexcitation (Fig. 6.17). As it can be seen from Fig. 6.17, τ increases very slowly with time after photoexcitation. This behavior is consistent with the preciously observed carrier density-dependence of τ: the relaxation time becomes longer at lower carrier density, as shown in Fig. 6.11. It is not fit by the Caughey-Thomas equation since the change is too small in the studied time range to get accurate fitting parameters.

The c-parameter obtained from the fits of the conductivity spectra at different pump-probe delay times to the Drude-Smith model is plotted in Fig. 6.18. The degree of carrier localization is the lowest at early times after excitation, and at later times the absolute value of the c-parameter slowly increases, indicating suppression of inter-grain carrier transport and increasing localization of photoexcited carriers in the nano-crystalline grains. At the probe delay longer than 10 ps, the degree of carrier localization remains nearly constant. Similar behavior was observed earlier in silicon nano-crystal films by Cooke *et al* [27] and Titova *et al* [62]. In the case of silicon nano-crystals, it was explained by either the increase in nano-crystal boundary barrier heights, or by the preferential trapping of carriers travelling in the connected nano-crystal pathways. Similar mechanisms might be at play in the nano-crystalline FeS_2 films, however, there are important differences in the carrier localization mechanisms and dynamics in these two systems. The c-parameter was found to be

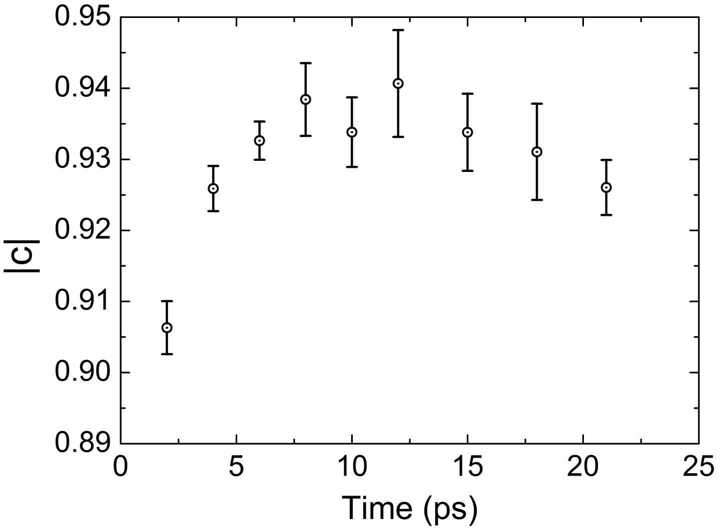

Figure 6.18: The c-parameter at different delay times after optical excitation.

fluence-independent in the case of Si nano-crystals embedded in SiO_2 [62], whereas the c-parameter in the nano-crystalline FeS_2 film exhibits a clear fluence dependence (Fig. 6.12).

We have also examined the time dependence of the carrier mobility, which was calculated from the Drude-Smith fit parameters as $\mu = (1 + c)e\tau/m^*$. The resulting values are plotted in Fig. 6.19, and vary from 16 cm^2/Vs to 24 cm^2/Vs. Mobility is highest immediately after photoexcitation, when the degree of carrier localization is the lowest, and it quickly falls to 16 cm^2/Vs within the first twelve picoseconds after the arrival of the optical pulse. At times longer than 15 ps, we observe a slight upturn in carrier mobility. Its origin needs to be further investigated but is likely related to a slight decrease in the carrier-carrier scattering rate as evidenced by the increase in relaxation time τ in Fig. 6.17.

6.6 Comparison Between Silicon on Sapphire and FeS_2 Films

As silicon is the most widely-used semiconductor in photovoltaics and other opto-electronic devices, comparison of the properties of silicon and FeS_2 thin films is useful for assessment of the suitability of nano-crystalline FeS_2 films

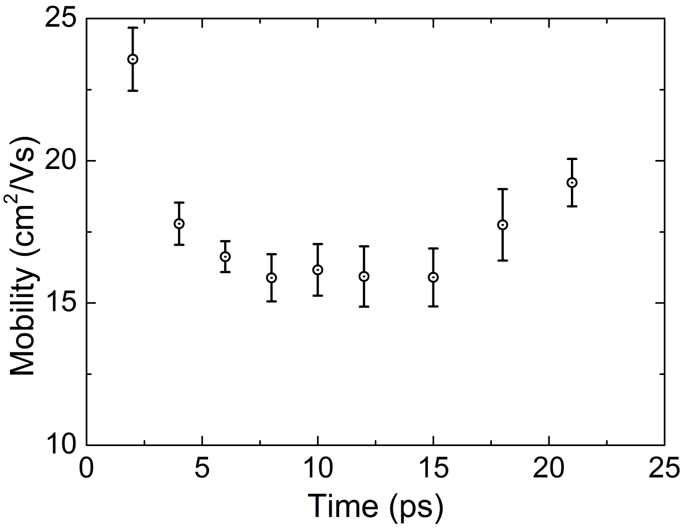

Figure 6.19: The carrier mobility as a function of time after the photoexcitation calculated from the Drude-Smith fit parameters as $\mu = (1 + c)e\tau/m^*$.

for photovoltaics. Here we compare the ultrafast photoconductivity dynamics in the silicon-on-sapphire thin film sample and the FeS_2 $\alpha80$ nano-crystalline film. The photoconductive properties of both films were measured with TRTS, using 400 nm pump pulses at a fluence of 50 μJ/cm^2.

As shown in Fig. 6.20, the peak magnitude of the photoconductive response of the nanogranular FeS_2 ($\alpha80$) sample is nearly 20% of the signal measured in epitaxial single crystalline silicon. Because the resistive film approximation works well in estimating the photoconductivity of both silicon-on-sapphire and iron pyrite nano-crystalline films, we roughly know the ratio of the photoconductivity from this comparison. Based on the conductivity comparison, the nano-crystalline FeS_2 films grown by GLAD techniques at angle $\sim 80^\circ$ indeed show promise for future applications in photovoltaic devices. However, before applications of iron pyrite nano-crystalline films can be realized, many outstanding issues, such as low quantum efficiency and strongly suppressed long-range conductivity, need to be addressed, and the mechanisms of photoconductivity in nano-granular FeS_2 films need to be elucidated.

According to the resistive film approximation equation [Eq. 3.39], the negative differential transmission is proportional to the product of quantum efficiency and the carrier mobility for small modulation. Based on the mobility and quantum efficiency extracted from the previous experiment,

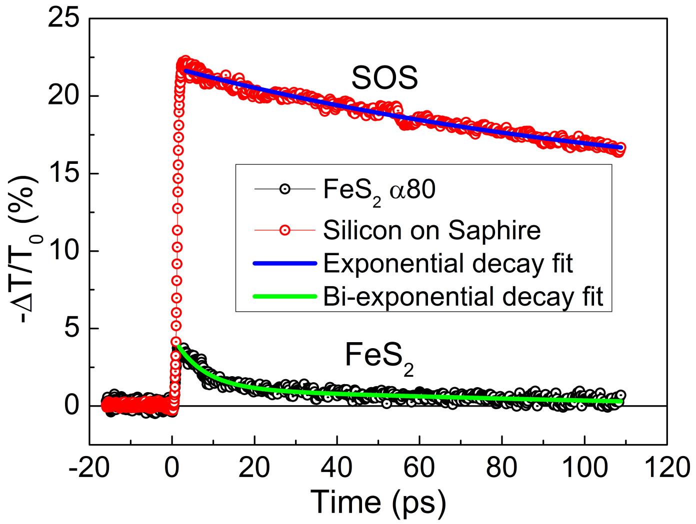

Figure 6.20: Optical pump-THz probe measurement on silicon-on-sapphire and FeS_2 nano-crystalline film. 400 nm pulses at 50 $\mu J/cm^2$ were used for excitation of both samples. The two solid lines are an exponential decay fit for silicon-on-sapphire and biexponential decay fit for FeS_2.

the ratio of the negative differential transmission of the silicon-on-sapphire and the iron pyrite nano-crystalline film should be much lower than 20% $((\eta\mu)_{\mathrm{FeS_2}}/((\eta\mu)_{\mathrm{SOS}} \cong 1\%)$. It is noted that we have used $\sigma_{\mathrm{DC}} = ne\mu$ in the resistive film approximation to develop Eq. 3.39. Though we have showed that the approximate value of conductivity is very close to the real conductivity at 1 THz for short scattering time, we have not tested whether using $\sigma_{\mathrm{DC}} = ne\mu$ in the resistive film approximation is a valid approach. For the simple Drude model with a short scattering time, σ_{DC} is roughly equal to the conductivity at 1 THz. But for Drude-Smith model, the conductivity at $\omega = 0$ THz is actually given by $\sigma(0) = (1 + c)ne\mu$. We have not tested yet which expression should be used to develop a more accurate equation for conductivity with high magnitude of c. As a result, we should use Eq. 3.35 instead of Eq. 3.39 for samples with Drude-Smith conductivity. For more accurate comparison, the data extracted from photoconductivity spectra should be used for both samples.

The peak carrier density n_{peak} measured from the carrier density decay curves of silicon-on-sapphire and FeS_2 $\alpha 80$ sample as a function of fluence are compared in Fig. 6.21. From the graph, we see that the peak carrier

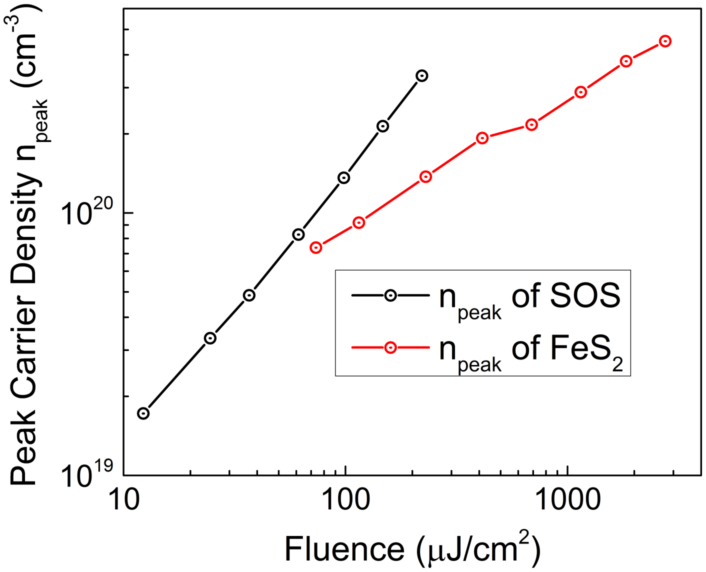

Figure 6.21: The peak carrier density n_{peak} of silicon-on-sapphire and FeS_2 α sample as a function of fluence.

density after photoexcitation of silicon-on-sapphire is linear with pump fluence, while the FeS_2 $\alpha80$ sample has a square root-dependence with pump fluence. As a result, the FeS_2 sample has a photoconductive response that is closer to that of silicon-on-sapphire at low pump fluence. At higher fluence, the photoconductive response of FeS_2 will be much lower compared to that of silicon-on-sapphire.

6.7 Exploring the Possibility of Multi-Exciton Generation in Nano-crystalline FeS_2 Film

As the most promising envisioned future application of thin FeS_2 films is in photovoltaics, it is important to investigate the possibility of multi-exciton generation in this material, as multi-exciton generation is one of the primary proposed mechanisms for exceeding the Shockley-Queisser power conversion efficiency limit [121–123]. Multi-exciton generation maximizes the power conversion efficiency by converting a high-energy photon into multiple electron-hole pairs.

Since the band gap of FeS_2 is 0.95 eV, incident light with wavelength shorter than 1305 nm can create excitons in the material. As the excitons are unsta-

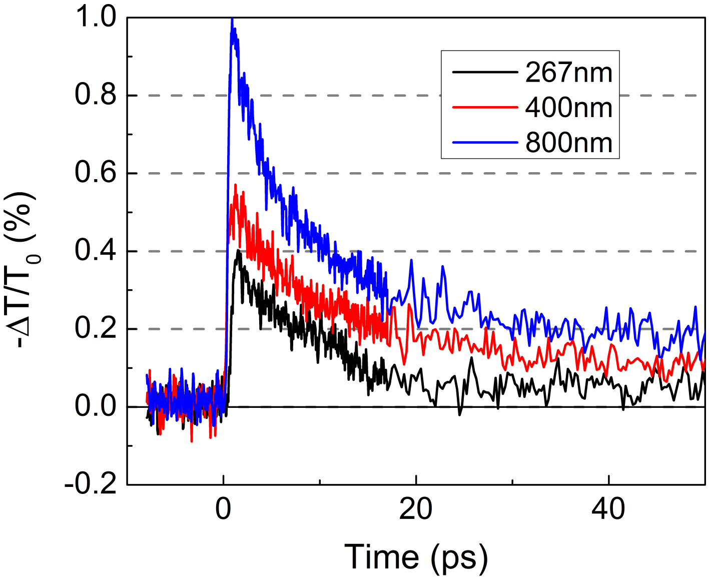

Figure 6.22: The normalized negative differential transmission of the THz pulse peak of the FeS_2 $\alpha 80$ film taken with 267 nm, 400 nm and 800 nm pump pulses at the same fluence ($F = 370$ μJ/cm^2).

ble at room temperature, they quickly become free-electron-hole pairs, which create photocurrent. When the energy of incident light is more than twice the band gap, one photon can generate more than one exciton. For FeS_2, this threshold energy is 1.9 eV, corresponding to 653 nm light.

In order to investigate whether multi-exciton generation occurs in the FeS_2 nano-crystalline films, we had carried out TRTS measurements using 800 nm, 400 nm and 267 nm pulses at the same fluence ($F = 370$ μJ/cm^2) for excitation. At equal fluence, the ratio of the number of photons in 800 nm, 400 nm, and 267 nm pump pulses is

$$P_{800} : P_{400} : P_{267} = 6 : 3 : 2 \tag{6.2}$$

In the event that no multiple exciton generation occurs in FeS_2, the ratio of the photoinduced carrier densities excited at the same fluence at 800 nm, 400 nm, and 267 nm should be the same as in Eq. 6.2. At the chosen pump fluence, the peak modulation of the THz pulse transmission at all three wavelengths is less than 20%, thus allowing us to use the ratio of the differential transmission magnitudes as a measure of photoexcited carrier density ratio.

The measured ratio of the peak differential transmission is 6 :3.3:2.3, which is very close to the ratio in Eq. 6.2. The small deviation from the ratio given in Eq. 6.2 is likely caused by the noise inherent in the experimental data or by a difference in the optical penetration depth, which may affect initial carrier recombination dynamics. It could also be caused by errors in measuring the reflectance of the optical pump beam at each wavelength. However, while the optical penetration depth of the sample is not known at 267 nm, it doesn't change much between 400 nm and 800 nm, and is not expected to be a major factor for comparing the photoexcited carrier densities at these wavelengths [105, 112]. With these uncertainties, it is hard to tell whether there is multi-exciton generation in the sample. As the ratio is actually slightly higher than expected, it may indicate that there is a small portion of photons that generate multiple excitons in the film.

Chapter 7

Conclusion

In conclusion, we have studied ultrafast carrier dynamics and conductivity in single crystalline GaAs, thin epitaxial silicon-on-sapphire, and nano-crystalline FeS_2 films using time-resolved terahertz spectroscopy. From the TRTS data, we have extracted the dark conductivity and the photoinduced complex conductivity spectra of the investigated samples in the 0.2 THz to 2.7 THz range. We have applied the Drude, Drude-Smith, and Lorentz conductivity models in order to analyse the frequency-dependent conductivity in the samples and extract important parameters, such as the degree of carrier localization, carrier relaxation and trapping times, as well as carrier mobility, that govern the ultrafast carrier dynamics in these materials.

In the case of silicon-on-sapphire, we found that the photoinduced conductivity decays following a single-exponential function, indicative of a single dominant charge trapping mechanism. We also found that the conductivity at low excitation fluences is well described by the Drude model, as expected for a single crystal semiconductors. At excitation fluences above 100 $\mu J/cm^2$, the carrier relaxation times and the carrier mobility decreased from 500 cm^2/Vs to 200 cm^2/Vs, and a non-Drude component of the conductivity was observed that could be fit with the Drude-Smith model, indicative of the carrier-carrier scattering becoming more important.

We have also assessed the validity of the resistive film approximation for determining photoinduced conductivity spectra and estimating the photoexcited carrier density in thin semiconducting films. We found the approximation to be valid when the Drude scattering time τ is lower than 100 fs. In addition, we studied the influence of the dark conductivity of the semiconducting films on the extraction of photoinduced complex conductivity spectra, and concluded that the dark conductivity doesn't affect the photoexcited conductivity when the Drude scattering time τ is small, and there is no Lorentz oscillator resonance in the studied sample in the frequency range of the setup (see Appendix A).

The TRTS of FeS_2 nano-crystalline samples has shown that the film grown with a GLAD angle of 80° has the longest carrier lifetime and highest photoinduced conductivity. The photoinduced conductivity in FeS_2 films exhibits a biexponential decay with a fast component on the order of 10 ps and a slow component on the order of 40 ps, indicating the presence of at least two different carrier trapping mechanisms. Using THz time-domain spectroscopy, we found that the dark conductivity of the FeS_2 nano-crystalline film is well-described by the Lorentz oscillator model with an oscillator frequency outside the experimental range. It is shown in Appendix A that this background conductivity doesn't influence the extraction of the photoinduced conductivity in time-resolved terahertz spectroscopy. We also find that the peak photoconductivity exhibits a square-root dependence on the excitation fluence, and that the carrier lifetime becomes shorter at higher excitation fluences. Transient photoconductivity induced by the 800 nm pump pulse can be well described by the Drude-Smith model with a c-parameter in the range of -0.9 to -0.95, indicating strong localization of photoexcited carriers. By varying the excitation fluence we have also found that the photoexcited carrier mobility in nanogranular FeS_2 film decreases as the carrier density becomes higher, suggesting that carrier-carrier scattering plays an important role in the photoconductive properties of this material.

The comparison between the photoconductive properties of the FeS_2 nano-crystalline thin film and the epitaxial silicon-on-sapphire film has shown that the peak photoconductive response of the FeS_2 film is close to 20% of the peak photoconductivity of epitaxial silicon. This relatively high peak photoinduced conductivity suggests that the nano-crystalline FeS_2 films indeed may be suitable for photovoltaic and other optoelectronic applications, though our experimental result indicates that there may only exist a small amount of multi-exciton generation. However, before the FeS_2 optoelectronic devices can be successfully implemented, a number of issues such as relatively low quantum efficiency and short photoexcited carrier lifetime of this material need to addressed by engineering morphology of the nano-structured FeS_2 films to optimize those parameters.

Bibliography

[1] B. Ferguson and X. C. Zhang, *Nature Materials* **1**, 26 (2002).

[2] P. U. Jepsen, D. G. Cooke, and M. Koch, *Laser Photonics Review* **5**, 124 (2011).

[3] D. M. Mittleman, M. Gupta, R. Neelamani, R. Baraniuk, J. Rudd, and M. Koch, *Applied Physics B* **68**, 1085 (1999).

[4] B. B. Hu and M. C. Nuss, *Optics Letters* **20**, 1716 (1995).

[5] Q. Wu, T. D. Hweitt, and X. C. Zhang, *Applied Physics Letters* **69**, 1026 (1996).

[6] J. F. Federici, B. Schulkin, F. Huang, D. Gary, R. Barat, F. Oliveira, and D. Zimdars, *Semiconductor Science and Technology* **20**, 266 (2005).

[7] N. Nishimura, R. Ogura, S. Matsumoto, M. Mizuno, and K. Fukunaga, *Electrical Engineering in Japan* **183**, 9 (2013).

[8] A. G. Markelz, A. Roitberg, and E. J. Heilweil, *Chemical Physics Letters* **320**, 42 (2002).

[9] L. H. Eadie, C. B. Reid, A. J. Fitzgerald, and V. P. Wallace, *Expert Systems with Applications* **40**, 2043 (2013).

[10] L. V. Titova, A. K. Ayesheshim, A. Golubov, D. Fogen, R. Rodriguez-Juarez, F. A. Hegmann, and O. Kovalchuk, *Biomedical Optics Express* **4**, 559 (2013).

[11] R. Köhler, A. Tredicucci, F. Beltram, H. E. Beere, E. H. Linfield, A. G. Davies, D. A. Ritchie, R. C. Iotti, and F. Rossi, *Nature* **417**, 156 (2002).

[12] J. Gao and F. A. Hegmann, *Applied Physics Letters* **93**, 223306 (2008).

[13] M. C. Nuss, K. W. Goossen, J. P. Gordon, P. M. Mankiewich, and M. L. O'Malley, *Journal of Applied Physics* **70**, 2238 (1991).

[14] F. Gao, G. L. Carr, C. D. Porter, D. B. Tanner, G. P. Williams, C. J. Hirschmugl, B. Dutta, X. D. Wu, and S. Etemad, *Physical Review B* **54**, 700 (1996).

[15] S. D. Brorson, R. Buhleier, I. E. Trofimov, J. O. White, C. Ludwig, F. F. Balakirev, H.-U. Habermeier, and J. Kuhl, *Journal of the Optical Society of America B* **13**, 1979 (1996).

[16] D. G. Cooke, F. A. Hegmann, Y. I. Mazur, W. Q. Ma, and X. Wang, *Applied Physics Letters* **85**, 3839 (2004).

[17] M. C. Beard, G. M. Turner, and C. A. Schmuttenmaer, *The Journal of Physical Chemistry B* **106**, 7146 (2002).

[18] M. Hangyo, M. Tani, and T. Nagashima, *International Journal of Infrared and Millimeter Waves* **26**, 1661 (2005).

[19] D. G. Cooke, F. A. Hegmann, E. C. Young, and T. Tiedje, *Applied Physics Letters* **89**, 122103 (2006).

[20] F. H. Su, F. Blanchard, G. Sharma, L. Razzari, A. Ayesheshim, T. L. Cocker, L. V. Titova, T. Ozaki, J. C. Kieffer, R. Morandotti, M. Reid, and F. A. Hegmann, *Optics Express* **17**, 9620 (2009).

[21] M. C. Beard, G. M. Turner, and C. A. Schmuttenmaer, *Physical Review B* **62**, 15764 (2000).

[22] M. Schall and P. U. Jepsen, *Optics Letters* **25**, 13 (2000).

[23] G. Li, D. Li, Z. Jin, and G. Ma, *Optics Communications* **285**, 4102 (2012).

[24] L. P. H. Lui and F. A. Hegmann, *Applied Physics Letters* **78**, 3478 (2001).

[25] O. Ostroverkhova, D. G. Cooke, S. Shcherbyna, R. F. Egerton, and F. A. Hegmann, *Physical Review B* **71**, 035204 (2005).

[26] O. Ostroverkhova, D. G. Cooke, and F. A. Hegmann, *Applied Physics Letters* **66**, 162121 (2006).

[27] D. G. Cooke, A. Meldrum, and P. U. Jepsen, *Applied Physics Letters* **101**, 211107 (2012).

[28] J. Kim, I. Maeng, J. Jung, H. Song, J.-H. Son, K. Kim, J. Lee, C.-H. Kim, G. Chae, M. Jun, Y. Hwang, S. J. Lee, J.-M. Myoung, and H. Choi, *Applied Physics Letters* **102**, 011109 (2013).

[29] T. L. Cocker, L. V. Titova, S. Fourmaux, H. C. Bandulet, D. Brassard, J. C. Kieffer, M. A. El Khakani, and F. A. Hegmann, *Applied Physics Letters* **97**, 221905 (2010).

[30] N. M. Froberg, B. B. Hu, X.-C. Zhang, and D. H. Auston, *IEEE Journal of Quantum Electronics* **28**, 2291 (1992).

[31] J. B. Khurgin, *Journal of the Optical Society of America B* **11**, 2492 (1994).

[32] D. Oikawa, A. Irie, and K. Yamaki, *IEEE Transactions on Applied Superconductivity* **23**, 3 (2013).

[33] K. L. Yeh, M. C. Hoffmann, J. Hebling, and K. A. Nelson, *Applied Physics Letters* **90**, 171121 (2007).

[34] J. E. Pedersen and S. R. Keiding, *IEEE Journal of Quantum Electronics* **28**, 2518 (1992).

[35] Q. Wu and X. C. Zhang, *Applied Physics Letters* **71**, 1285 (1997).

[36] D. Krökel, D. Grischkowsky, M. B. Ketchen, and X. C. Zhang, *Applied Physics Letters* **64**, 1324 (1994).

[37] F. Blanchard, L. Razzari, H. C. Bandulet, G. Sharma, R. Morandotti, J. C. Kieffer, T. Ozaki, M. Reid, H. F. Tiedje, H. K. Haugen, and F. A. Hegmann, *Optics Express* **15**, 13212 (2007).

[38] M. Bass, P. A. Franken, J. F. Ward, and G. Weinreich, *Physical Review Letters* **9**, 446 (1962).

[39] S. L. Chuang, *Physical Review Letters* **68**, 102 (1992).

[40] X. C. Zhang, Y. Jin, and X. F. Ma, *Applied Physics Letters* **61**, 2764 (1992).

[41] D. J. Griffiths, *Introduction to Electrodynamics*, Pearson Benjamin Cummings, third edition, 2008.

[42] A. Nahata, D. H. Auston, T. F. Heinz, and C. Wu, *Applied Physics Letters* **68**, 150 (1996).

[43] Q. Wu and X. C. Zhang, *Applied Physics Letters* **67**, 3523 (1995).

[44] Z. G. Lu, P. Campbell, and X. C. Zhang, *Applied Physics Letters* **71**, 593 (1997).

[45] Q. Wu, M. Litz, and X. C. Zhang, *Applied Physics Letters* **68**, 2924 (1996).

[46] J. A. Kash, *Physical Review B* **40**, 3455 (1989).

[47] F. Blanchard, D. Golde, F. H. Su, L. Razzari, G. Sharma, R. Morandotti, T. Ozaki, M. Reid, M. Kira, S. W. Koch, and F. A. Hegmann, *Physical Review Letters* **107**, 107401 (2011).

[48] G. Sharma, L. Razzari, F. H. Su, F. Blanchard, A. Ayesheshim, T. L. Cocker, L. V. Titova, H. C. Bandulet, T. Ozaki, J. C. Kieffer, R. Morandotti, M. Reid, and F. A. Hegmann, *IEEE Photonics Journal* **2**, 578 (2010).

[49] P. N. Saeta, J. F. Federici, B. I. Greene, and D. R. Dykaar, *Applied Physics Letters* **60**, 1477 (1992).

[50] G. Sharma, I. Al-Naib, H. Hafez, R. Morandotti, D. G. Cooke, and T. Ozaki, *Optics Express* **20**, 18016 (2012).

[51] M. Walters, B. Fischer, M. Schall, H. Helm, and P. U. Jepsen, *Chemical Physics Letters* **332**, 389 (2000).

[52] D. G. Cooke, *Time-Resolved Terahertz Spectroscopy of Bulk and Nanoscale Semiconductors*, PhD thesis, University of Alberta, 2006.

[53] L. Duvillaret, F. Garet, and J.-L. Coutaz, *IEEE Journal of Selected Topics in Quantum Electronics* **2**, 739 (1996).

[54] B. I. Greene, J. F. Federici, D. R. Dykaar, A. F. J. Levi, and L. Pfeiffer, *Optics Letters* **16**, 48 (1991).

[55] L. Razzari, F. H. Su, G. Sharma, F. Blanchard, A. Ayesheshim, H. C. Bandulet, R. Morandotti, J. C. Kieffer, T. Ozaki, M. Reid, and F. A. Hegmann, *Physical Review B* **79**, 193204 (2009).

[56] D. E. Aspnes and A. A. Studna, *Physical Review B* **27**, 985 (1983).

[57] M. C. Beard, G. M. Turner, and C. A. Schmuttenmaer, *Physical Review B* **62**, 15764 (2000).

[58] T.-I. Jeon and D. Grischkowsky, *Physical Review Letters* **78**, 1106 (1997).

[59] M. Fox, *Optical Properties of Solids*, Oxford Universty Press Inc., second edition, 2010.

[60] N. V. Smith, *Physical Review B* **64**, 155106 (2001).

[61] D. G. Cooke, A. N. MacDonald, A. Hryciw, J. Wang, Q. Li, A. Meldrum, and F. A. Hegmann, *Physical Review B* **73**, 193311 (2006).

[62] L. V. Titova, T. L. Cocker, D. G. Cooke, X. Wang, A. Meldrum, and F. A. Hegmann, *Physical Review B* **83**, 085403 (2011).

[63] M. Walther, D. G. Cooke, C. Sherstan, M. Hajar, M. R. Freeman, and F. A. Hegmann, *Physical Review B* **76**, 125408 (2007).

[64] T. L. Cocker, L. V. Titova, S. Fourmaux, G. Holloway, H.-C. Bandulet, D. Brassard, J.-C. Kieffer, M. A. El Khakani, and F. A. Hegmann, *Physical Review B* **85**, 155120 (2012).

[65] T.-T. Kang, M. Yamamoto, M. Tanaka, A. Hashimoto, A. Yamamoto, R. Sudo, A. Noda, D. W. Liu, and K. Yamamoto, *Optics Letters* **34**, 2507 (2009).

[66] H. Němec, P. Kužel, and V. Sundström, *Physical Review B* **79**, 115309 (2009).

[67] K. Shimakawa, T. Itoh, H. Naito, and S. O. Kasap, *Applied Physics Letters* **100**, 132102 (2012).

[68] D. G. Cooke, F. A. Hegmann, Y. I. Mazue, Z. M. Wang, W. Black, H. Wen, G. J. Salamo, T. D. Mishima, G. D. Lian, and M. B. Johnson, *Journal of Applied Physics* **103**, 023710 (2008).

[69] F. A. Hegmann, O. Ostroverkhova, and D. G. Cooke, *Photophysics of Molecular Materials: From Single Molecules to Single Crystals* , 367 (2006).

[70] A. Nahata, A. S. Weling, and T. F. Heinz, *Applied Physics Letters* **69**, 2321 (1996).

[71] A. Rice, Y. Jin, X. F. Ma, and X. C. Zhang, *Applied Physics Letters* **64**, 1324 (1994).

[72] M. van Exter, C. Fattinger, and D. Grischkowsky, *Optics Letters* **14**, 1128 (1989).

[73] P. H.-L. Sit, M. H. Cohen, and A. Selloni, *The journal of Physical Chemistry Letters* **3**, 2409 (2012).

[74] R. Sun, M. K. Y. Chan, and G. Ceder, *Physical Review B* **83**, 235311 (2011).

[75] M. Erbudak and T. E. Fischer, *Physical Review Letters* **29**, 732 (1972).

[76] S.-I. Kitamura and M. Iwatsuki, *Japanese Journal of Applied Physics* **34**, 145 (1995).

[77] M. Cardona and F. H. Pollak, *Physical Review* **142**, 530 (1966).

[78] A. B. Sproul, M. A. Green, and A. W. Stephens, *Journal of Applied Physics* **72**, 4161 (1992).

[79] A. R. Moore, *Applid Physics Letters* **31**, 762 (1977).

[80] D. R. Solli, P. Koonath, and B. Jalali, *Physical Review A* **79**, 053853 (2009).

[81] G. N. Koskowich, M. Soma, and R. B. Darling, *Physical Review B* **41**, 2944 (1990).

[82] D. Grischkowsky, S. Keiding, M. van Exter, and C. Fattinger, *Journal of the Optical Society of America B* **7**, 2006 (1990).

[83] G. W. Ludwig and R. L. Watters, *Physical Review* **101**, 1699 (1956).

[84] J. J. letcher, K. Kang, and D. G. Cahill, *Applied Physics Letters* **90**, 252104 (2007).

[85] J. S. Dugdale and Z. S. Basinski, *Physical Review* **157**, 552 (1967).

[86] T. Ichibayashi and K. Tanimura, *Physical Review Letters* **102**, 087403 (2009).

[87] N. S. Wingreen, *Physical Review B* **40**, 3191 (1989).

[88] M. Combescot and R. Combescot, *Physical Review B* **35**, 7986 (1987).

[89] D. M. Caughey and R. E. Thomas, *Proceedings of the IEEE* , 2192 (1967).

[90] Z. Mics, A. D'Angio, S. A. Jensen, M. Bonn, and D. Turchinovich, *Applied Physics Letters* **102**, 231120 (2013).

[91] S. Reggiani, M. Valdinoci, L. Colalongo, M. Rudan, G. Baccarani, A. D. Stricker, F. Illien, N. Felber, W. Fichtner, and L. Zullino, *IEEE Transactions on Electron Devices* **49**, 490 (2002).

[92] C.-M. Li, T. Sjodin, and H.-L. Dai, *Physical Review B* **56**, 15252 (1997).

[93] Q. L. Zhou, Y. Shi, B. Jin, and C. Zhang, *Applied Physics Letters* **93**, 102103 (2008).

[94] A. Ennaoui, S. Fiechter, C. Pettenkofer, N. Alonso-Vante, K. Büker, M. Bronold, C. Höpfner, and H. Tributsch, *Solar Energy Materials and Solar Cells* **29**, 289 (1993).

[95] C. Steinhagen, T. B. Harvey, C. J. Stolle, J. Harris, and B. A. Korgel, *The Journal of Physical Chemistry Letters* **3**, 2352 (2012).

[96] J. Puthussery, S. Seefeld, N. Berry, M. Gibbs, and M. Law, *Journal of the American Chemical Society* **133**, 716 (2011).

[97] M. Cabán-Acevedo, M. S. Faber, Y. Tan, R. J. Hamers, and S. Jin, *Nano Letters* **12**, 1977 (2012).

[98] Y. Bi, Y. Yuan, C. L. Exstrom, S. A. Darveau, and J. Huang, *Nano Letters* **11**, 4953 (2011).

[99] L. Vadkhiya and B. L. Ahuja, *Journal of Alloys and Compounds* **509**, 3042 (2011).

[100] V. N. Antonov, L. P. Germash, A. P. Shpak, and A. N. Yaresko, *Physica Status Solidi B* **246**, 411 (2009).

[101] G. Qiu, Q. Xiao, Y. Hu, W. Qin, and D. Wang, *Journal of Colloid and Interface Science* **270**, 127 (2004).

[102] W. Folkerts, G. A. Sawatzky, C. Hass, R. A. de Groot, and F. U. Hillebrecht, *Journal of Physics C: Solid State Physics* **20**, 4135 (1987).

[103] J. Cai and M. R. Philpott, *Computational Materials Science* **30**, 358 (2004).

[104] A. M. Karguppikar and A. G. Vedeshwar, *Physica Status Solidi (a)* **109**, 549 (1988).

[105] H. A. Macpherson and C. R. Stoldt, *ACS Nano Article* **6**, 8940 (2012).

[106] C. H. Ho, Y. S. Huang, and K. K. Tiong, *Journal of Alloys and Compounds* **422**, 321 (2006).

[107] A. Baruth, M. Manno, D. Narasimhan, A. Shankar, and X. Zhang, *Journal of Applied Physics* **112**, 054328 (2012).

[108] B. V. da F. L. Amorim, F. J. Moura, E. A. Brocchi, M. J. P. Vieira, and M. T. da C. Rupp, *Metallurgical and Meterials Transactions B* **43B**, 781 (2012).

[109] D.-Y. Wang, Y.-T. Jiang, C.-C. Lin, S. sian Li, and Y.-T. Wang, *Advanced Materials* **24**, 3415 (2012).

[110] F. Wang, L. Huang, Z. Luan, J. Huang, and L. Meng, *Materials Chemistry and Physics* **132**, 505 (2012).

[111] L. Vadkhiya and B. L. Ahuja, On the possibility of solar cell applications of iron pyrite, in *AIP Conference Proceedings*, 2011.

[112] J. M. LaForge, B. Gyenes, S. Xu, L. K. Haynes, L. V. Titova, F. A. Hegmann, and M. J. Brett, *Solar Energy Materials and Solar Cells* **117**, 306 (2013).

[113] F. Wang, Y. Wang, L. Y. Huang, Z. J. Luan, and L. Meng, *Materials Research Innovations* **15**, 410 (2011).

[114] D. F. Pridmore and R. T. Shuey, *American Mineralogist* **61**, 248 (1976).

[115] J. L. Verble and R. F. Wallis, *Physical Review* **182**, 783 (1969).

[116] E. D. Palik, *Handbook of Optical Constants of Solids*, volume 3, Academic Press, 1998.

[117] H. D. Lutz, G. Schneider, and G. Kliche, *Journal of Physics and Chemistry Solids* **46**, 437 (1985).

[118] I. Opahle, K. Koepernik, and H. Eschrig, *Physical Review B* **60**, 14035 (1999).

[119] C. Sourisseau, R. Cavagnat, and M. Fouassier, *Journal of Physics and Chemistry of Solids* **52**, 537 (1991).

[120] W. B. Jackson, *Philosophical Magazine Letters* **60**, 277 (1989).

[121] M. C. Beard, K. P. Knutsen, P. Yu, J. M. Luther, Q. Song, W. K. Metzger, R. J. Ellingson, and A. J. Nozik, *Nano Letters* **7**, 2506 (2007).

[122] H. W. Hillhouse and M. C. Beard, *Current Opinion in Colloid & Interface Science* **14**, 245 (2009).

[123] O. E. Semonin, J. M. Luther, S. Choi, H.-Y. Chen, J. Gao, A. J. Nozik, and M. C. Beard, *Science* **334**, 1530 (2011).

Appendix A

Background Conductivity Correction

In a TRTS experiment, we measure an optical pump pulse to excite a conducting thin film near the surface of the sample and then compare it to the reference THz pulse, *i.e.*, the pulse through the sample without optical pump. In developing the thin film approximation, the substrate and thin film is assumed to be semi-insulating without optical pump pulse. But some of the thin film samples are already conducting without photo-excitation. When there is a background conductivity , the method used to extract the conductivity has to be modified. Eq. 3.27 now becomes

$$\frac{T_s(\omega)}{T_0(\omega)} = \frac{E_s(\omega)}{E_0(\omega)} = \frac{1+N+Z_0\hat{\sigma}_b(\omega)d}{1+N+Z_0\big[\hat{\sigma}_s(\omega)+\hat{\sigma}_b(\omega)\big]d} \tag{A.1}$$

where $\hat{\sigma}_b(\omega)$ is the background conductivity and $\hat{\sigma}_s(\omega)$ is the photo-induced conductivity as usual. Both these conductivities are frequency dependent.

Now if we want to extract the photo-induced conductivity from experimental data, we need to separate the real and imaginary part of Eq. A.1. Substituting Eq. 3.29 into the reverse of last equation, we get

$$\begin{gathered}\Big(1+N+Z_0\sigma_{b1}d-iZ_0\sigma_{b2}d\Big)\Big[1+N+Z_0d(\sigma_{b1}+\sigma_{s1}) \\ +iZ_0d(\sigma_{b2}+\sigma_{s2})\Big] = \frac{A_0}{A_s}\exp^{i[\phi_0-\phi_s]}\Big\{\Big[1+N+Z_0d\sigma_{b1}\Big]^2+\Big[Z_0d\sigma_{b2}\Big]^2\Big\}\end{gathered} \tag{A.2}$$

where all the conductivity, amplitude and phase are frequency dependent but are simplified to be succinct. Separating the real and imaginary part we get two separate equations:

$$
\begin{aligned}
(1+N+Z_0\sigma_{b1}d)\Big[1+N+Z_0d(\sigma_{b1}+\sigma_{s1})\Big]+Z_0\sigma_{b2}d\Big[Z_0d(\sigma_{b2}+\sigma_{s2})\Big]& \\
=\bigg\{\Big[1+N+Z_0d\sigma_{b1}\Big]^2+\Big[Z_0d\sigma_{b2}\Big]^2\bigg\}\frac{A_0}{A_s}\cos[\phi_0-\phi_s]&
\end{aligned}
\tag{A.3}
$$

$$
\begin{aligned}
Z_0d(\sigma_{b2}+\sigma_{s2})(1+N+Z_0\sigma_{b1}d)-Z_0\sigma_{b2}d\Big[1+N+Z_0d(\sigma_{b1}+\sigma_{s1})\Big]& \\
=\bigg\{\Big[1+N+Z_0d\sigma_{b1}\Big]^2+\Big[Z_0d\sigma_{b2}\Big]^2\bigg\}\frac{A_0}{A_s}\sin[\phi_0-\phi_s]&
\end{aligned}
\tag{A.4}
$$

The two equations can be solved for σ_{s1} and σ_{s2} as a function of other parameters. When knowing the background conductivity σ_{b1} and σ_{b2}, the photoinduced conductivity could be calculated. This complicates the process of extracting photoinduced conductivity from the thin film. An extra step to extract the background conductivity from THz-TDS experiment will be necessary in such case. The σ_{s1} and σ_{s2} as functions of σ_{b1} and σ_{b2} are

$$
\begin{aligned}
\sigma_{s1}=\bigg\{Y\frac{A_0}{A_s}\cos(\phi_0-\phi_s)-(1+N+Z_0\sigma_{b1}d)^2& \\
-Z_0\sigma_{b2}d(Z_0\sigma_{b2}d+Z_0\sigma_{s2}d)\bigg\}/\bigg\{Z_0d(1+N+Z_0\sigma_{b1}d)\bigg\}&
\end{aligned}
\tag{A.5}
$$

$$
\begin{aligned}
\sigma_{s2}=\bigg\{Y\frac{A_0}{A_s}\sin(\phi_0-\phi_s)-Z_0\sigma_{b2}d(1+N+Z_0\sigma_{b1}d)& \\
+\frac{Z_0\sigma_{b2}dY\frac{A_0}{A_s}}{\cos}(\phi_0-\phi_s)1+N+Z_0\sigma_{b1}d\bigg\}& \\
/\bigg\{Z_0d\Big[(1+N+Z_0\sigma_{b1}d)+\frac{(Z_0\sigma_{b2}d)^2}{1+N+Z_0\sigma_{b1}d}\Big]\bigg\}&
\end{aligned}
\tag{A.6}
$$

where $Y=[1+N+Z_0\sigma_{b1}d]^2+[Z_0\sigma_{b2}d]^2$.

A LabView program was written to extract the photoinduced conductivity with the exist of a background conductivity. In this program, the background conductivity can be defined by the user by inputting the ω_p, τ and c. The THz waveforms measured in the time-resolved terahertz spectroscopy are loaded to the program. The amplitude and phase spectra of the reference THz waveform and the pumped THz waveforms are calculated with Fast Fourier Transform. Then the photoinduced conductivity is calculated by using Eq. A.5 and Eq. A.6. The photoinduced conductivity calculated without considering background conductivity using Eq. 3.32 and Eq. 3.33 is also shown in the program.

These two conductivities calculated with and without background conductivity are compared in the graph to see how the background conductivity influence the extraction of the photoindiced conductivity.

A wide range of background conductivities have been tested with several sets of terahertz waveforms measured in time-resolved terahertz spectroscopy. For Lorentz oscillator conductivity such as in the FeS_2 nano-crystalline films, the background conductivity doesn't influence the extraction of the photo-induced conductivity when the central frequency of the oscillators are not in the range of the THz spectrum. When there is an oscillator in the spectrum range, the extracted conductivity ignoring the background conductivity deviate from the conductivity calculated with the background by a large extent.

For Drude and Drude-Smith model, it is acceptable to ignore the background conductivity in extracting photoinduced conductivity when τ is not higher than 100 fs, *i.e.*, the crossing point between real and imaginary conductivity is not in the range of our spectra. When $\tau < 100$ fs, the real and imaginary conductivity change smoothly in the range of THz spectroscopy. Combining all the background conductivities that have been tried, it could be shown that the background conductivity only affects the extraction of photoinduced conductivity when the real or imaginary conductivity changes rapidly in the range of THz spectroscopy, *i.e.*, from 0.2 THz to 2.7 THz.

Appendix B

Simulation for Testing Thin Film Approximation

To test the validity of the thin film approximation, the waveform transmitted through the conducting thin film is compared to the reference waveform to see whether there is significant phase shift that influences the approximation result. And then the conductivity calculated from Eq. 3.35 is compared to the actual conductivity of the thin film, which directly reflects the accuracy of the approximation. The logical design of the program has the following sequence:

1. Load reference THz waveform.
2. Input conductivity and film information.
3. Calculate the transmitted THz waveform based on the conductivity.
4. Compare the simulated waveform with the reference waveform.
5. Compare the conductivity from approximation to the actual value.

The reference THz pulse we use in the program is a real THz pulse from a THz TDS scan, which allows us to get exactly the same amplitude spectrum as in our experiment. The program read a data file and loads the reference THz waveform. After the waveform is loaded, it is converted to amplitude and phase spectra using a Fast Fourier Transform.

From Eq. 3.30 and Eq. 3.31, we see that the amplitude and phase of the reference THz pulse and the sample THz pulse can be used to calculate the conductivity of the thin film. Inversely, when we know the conductivity of the thin film and the amplitude and phase of the reference THz waveform, we are able to predict the THz pulse transmitted through the thin conducting film by the following equations:

$$A_s(\omega) = A_0 \sin(\phi_0(\omega) - \phi_s(\omega)) \left[\frac{1+N}{Z_0 \sigma_2(\omega) d} \right] \tag{B.1}$$

$$\phi_s(\omega) = \phi_0(\omega) - \arctan \left[\frac{Z_0 \sigma_2(\omega) d}{1+N+Z_0 \sigma_1(\omega) d} \right] \tag{B.2}$$

We want the conductivity of the thin film to be well defined so that we have a baseline for comparison. In the program, the conductivity of the thin film is defined by the user. The user has the freedom to create Drude model and Drude-Smith model by specifying the value of ω_p, τ and c. The thickness d of the conducting film and refractive index N of the substrate are also input by the user. Based on the conductivity and these parameters, the amplitude and phase of the THz waveform transmitted through the conducting film are calculated.

Then an inverse FFT is performed on the amplitude and phase to get the THz waveform in time domain. The amplitude attenuation and phase shift were measured by comparing this simulated pulse to the reference pulse. If there is a significant phase shift, then the modulation of transmission ΔT measured in the optical pump-THz probe experiment is not simply due to the amplitude attenuation. Because the delay stage controlling the probe pulse is fixed at the position detecting the THz peak of the reference waveform, the probe pulse will no longer be detecting the pulse peak if it is shifted. This will lead to discrepancy in the thin film approximation. And the discrepancy can be calculated by comparing the modulation with fixed stage position to the actual amplitude attenuation.

The conductivity based on the thin film approximation is calculated from the differential transmission $\left|\frac{\Delta T}{T}\right|$ using Eq. 3.35. When there is a discrepancy in the differential transmission, the conductivity calculated also contains non-negligible error. The program calculates the conductivity based on the $\left|\frac{\Delta T}{T}\right|$ and then compares it to the actual conductivity at 1THz defined by the user. The discrepancy is also calculated and shown in the result panel.

The simulation program is developed in NI LabVieW 8.6. The program user interface could not be shown clearly in one picture. So the modules in the program are separately shown in multiple screen shots. In Fig. B.1 it shows the module that reads THz waveform and do a Fast Fourier Transform of the

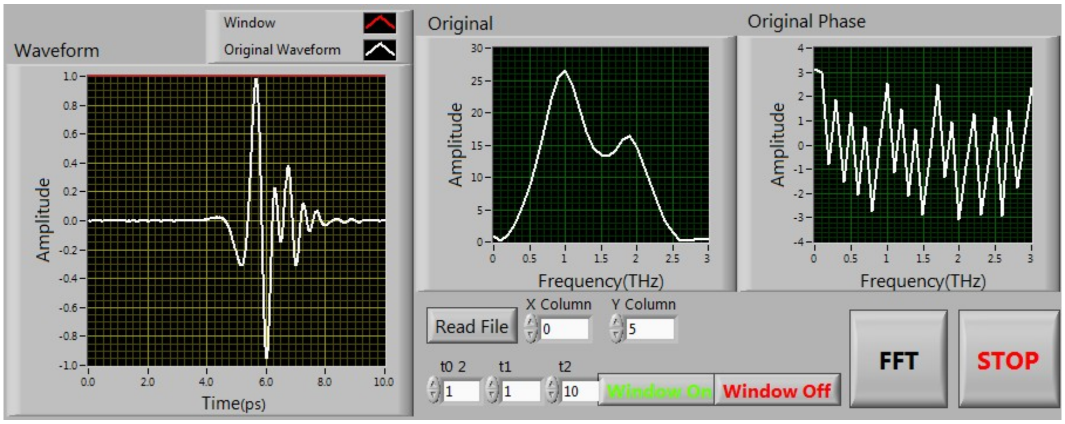

X Column 0

Y Column 5

t0 2 1

t1 1

t2 10

Figure B.1: The module in the simulation program that reads the THz waveform from data file and do a Fast Fourier Transform on the waveform. The waveform and the FFT results are shown in separate plot windows.

waveform.

By clicking the Read File button, the program asks the user to specify the path of the data file that contains the terahertz waveform. The user needs to specify the columns in the file where the THz amplitude and time data are stored. After reading the file, the THz waveform will be plotted in the waveform window on the left side.

In the row below the Read File button, one can specify whether the original pulse should be windowed. One can specify the range of the window by specifying the value of t_1 and t_2. The sharpness of the window function can be controlled by changing the value of t_0. Sometimes using the window can reduce the noise ratio. If the data is quite clean and the user doesn't want any influence on the original data, window can be turned off simply by clicking on the Window Off button.

Then, the waveform is converted to amplitude spectrum and phase spectrum in frequency domain by Fast Fourier Transform. The amplitude and phase spectra are shown in the plot window as well. In the labview FFT function, the phase result is shifted to the range between $-\pi$ and π. Because only the phase difference is of interest, whether the phase is shifted or not doesn't influence our result.

The module that allows the user to define the conductivity of the thin film and simulate the THz waveform transmitted through the conducting film is shown Fig. B.2. After getting the FFT result in last step, user can determine the conductivity of the thin film by type in the value of ω_p, τ and c. The

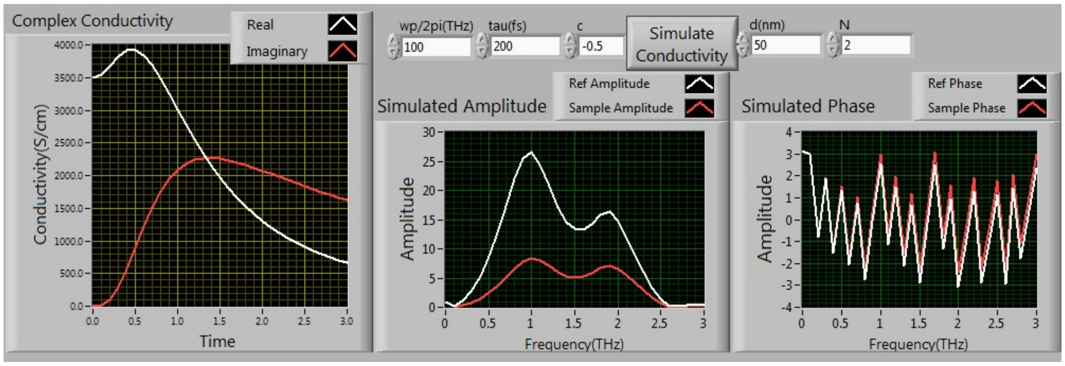

wp/2pi(THz) 100

tau(fs) 200

c -0.5

d(nm) 50

N 2

Figure B.2: The module in the simulation program that lets the user define the conductivity of the thin film and then simulate the THz waveform transmitted through the conducting film.

thickness d of the conducting film and the refractive index N of the substrate are also defined by the user.

After all these parameters are typed, a user can click on the Simulate Conductivity button to continue. The program first calculates the frequency dependent conductivity based on the parameters the user input. The conductivity is then plotted in the plot window on the left. The frequency dependent amplitude and phase of the THz waveform transmitted through the conducting film are calculated using Eq. B.1 and Eq. B.2. These amplitude and phase are plotted along with the amplitude and phase of the reference pulse in two plot windows. The amplitude attenuation and phase shift can be seen in these windows directly.

After the amplitude and phase of the transmitted THz pulse are calculated, an inverse Fast Fourier Transform is used to recover the THz pulse in time domain. The result is shown in the result panel in Fig. B.3. The THz pulse transmitted through the conducting film is plotted along with the original THz pulse in the plot window. The program traces the peak of these two THz pulses and shows the phase shift in time domain. The discrepancy of the differential transmission caused by the phase shift is shown in the result panel. Also, the conductivity calculated from the differential transmission $\frac{\Delta T}{T}$ is compared to the conductivity defined by the user. The discrepancy is shown in the result panel, too. All these results can be saved to a single file that contains the reference waveform, the simulated waveform and all the parameters. Since this file contains both the THz pulses, it can be loaded into the program we use to extract conductivity to check the validity of the simulated result. By using the original THz waveform and the simulated waveform, the transient conductivity

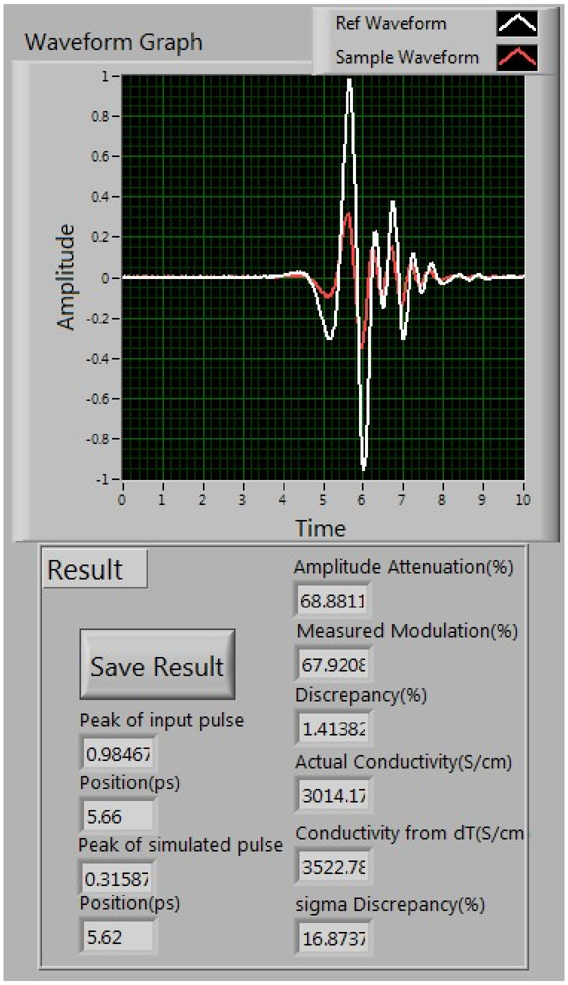

Peak of input pulse
0.98467
Position(ps)
5.66
Peak of simulated pulse
0.31587
Position(ps)
5.62

Amplitude Attenuation(%)
68.8811
Measured Modulation(%)
67.9208
Discrepancy(%)
1.41382
Actual Conductivity(S/cm)
3014.17
Conductivity from dT(S/cm
3522.78
sigma Discrepancy(%)
16.8737

Figure B.3: The module that shows the transmitted THz waveform and the simulation result.

is calculated using Eq. 3.32 and Eq. 3.33. The calculated conductivity exactly matches the conductivity used to simulate the transmitted THz waveform without any error.